Alma Mater Studiorum · Università di Bologna

Scuola di Scienze
Corso di Laurea Magistrale in Fisica

Image Quality and Dose Evaluation of Filtered Back Projection Versus Iterative Reconstruction Algorithm in Multislice Computed Tomography

Relatore:
Prof. Maria Pia Morigi

Correlatore:
Prof. Luisa Pierotti

Presentata da:
Daniele Pesolillo

Sessione III
Anno Accademico 2013/2014

Alla mia famiglia.....che mi ha dato una seconda possibilità.

Contents

List of Figures

Abstract

Il presente lavoro di tesi è stato svolto presso il servizio di Fisica Sanitaria del Policlinico Sant'Orsola-Malpighi di Bologna.

Lo studio si è concentrato sul confronto tra le tecniche di ricostruzione standard (Filtered Back Projection, FBP) e quelle iterative in Tomografia Computerizzata.

Il lavoro è stato diviso in due parti: nella prima è stata analizzata la qualità delle immagini acquisite con una CT multislice (iCT 128, sistema Philips) utilizzando sia l'algoritmo FBP sia quello iterativo (nel nostro caso iDose^4). Per valutare la qualità delle immagini sono stati analizzati i seguenti parametri: il Noise Power Spectrum (NPS), la Modulation Transfer Function (MTF) e il rapporto contrasto-rumore (CNR). Le prime due grandezze sono state studiate effettuando misure su un fantoccio fornito dalla ditta costruttrice, che simulava la parte body e la parte head, con due cilindri di 32 e 20 cm rispettivamente.

Le misure confermano la riduzione del rumore ma in maniera differente per i diversi filtri di convoluzione utilizzati. Lo studio dell'MTF invece ha rivelato che l'utilizzo delle tecniche standard e iterative non cambia la risoluzione spaziale; infatti gli andamenti ottenuti sono perfettamente identici (a parte le differenze intrinseche nei filtri di convoluzione), a differenza di quanto dichiarato dalla ditta. Per l'analisi del CNR sono stati utilizzati due fantocci; il primo, chiamato Catphan 600 è il fantoccio utilizzato per caratterizzare i sistemi CT. Il secondo, chiamato Cirs 061 ha al suo interno degli inserti che simulano la presenza di lesioni con densità tipiche del distretto addominale. Lo studio effettuato ha evidenziato che, per entrambi i fantocci, il rapporto contrasto-rumore aumenta se si utilizza la tecnica di ricostruzione iterativa.

La seconda parte del lavoro di tesi è stata quella di effettuare una valutazione della riduzione della dose prendendo in considerazione diversi protocolli utilizzati nella pratica clinica, si sono analizzati un alto numero di esami e si sono calcolati i valori medi di CTDI e DLP su un campione di esame con FBP e con iDose^4. I risultati mostrano che i valori ricavati con

l'utilizzo dell'algoritmo iterativo sono al di sotto dei valori DLR nazionali di riferimento e di quelli che non usano i sistemi iterativi.

Introduction

Today, ionizing radiation from Computed Tomography (CT) scanners represents the greatest per capita medical exposure for the population of industrialized countries. Although this growth is mainly attributed to the increasing number of CT examinations, CT dose per examination is still high and remains an important worry.

Academia, industry, and government have responded with efforts to reduce the radiation dose required to obtain diagnostic-quality images. Research has shown that some incident cancer cases may be associated with CT scans. Although the risks for an individual are small, the rapid increase of CT utilization has created some significant concern over the patient radiation dose.

Automatic dose control comprimes all technical means to adapt the tube current to the attenuation properties of individual patients. Dose modulation is the adaptation of the tube current to varying attenuation by the patient during one revolution of the x-ray source (circular dose modulation) or along z-axis (longitudinal dose modulation). It results, if adequately designed, in significantly reduced dose values depending on the body region. Longitudinal dose modulation aims to ensure a constant noise level regardless of the local attenuation properties. By doing so, dose will inevitably be increased when proceeding from the upper abdomen to the pelvis in examinations of the entire abdomen. Noise, however, is not the only characteristic related to image quality; in the pelvis, the dose should instead be decreased owing to the improved inherent contrast which permits an increased noise level.

With increasing recognition of the importance of radiation protection, dose reduction has become an important issue in CT system development. In the past decade, several techniques for reducing CT radiation dose have been developed. The challenge of reducing dose is to maintain image quality because noise is increased at decreasing exposure level.

Maintaining clinically acceptable image quality at low dose is the goal of many techniques for reducing radiation dose.

Modern CT systems are equipped with several dose reduction techniques.

These techniques range from hardware, such as a sliding collimator to eliminate unnecessary radiation exposure due to overranging, to algorithms such as improved filtered back projection (FBP) and iterative reconstruction (IR). One step has been CT manufactures implementing iterative reconstruction methods that for certain clinical tasks can improve dose efficiency over the conventional reconstruction method, filtered back projection.

While analytical algorithms such as FBP are based on only a single reconstruction, iterative algorithms use multiple repetitions in which the current solution converges towards a better solution. As a consequence, the computational demands are much higher.

Due to the exponential growth of computer technology proposed by Moore's law, which is holding since the 1970s, and the computational capacities available in a modern processor or graphics adapter the usage of IR methods has become a realistic option, with reconstruction times acceptable for clinical workflow. Nevertheless, new algorithmic innovations are needed because computational demands have increased due to the fact that image resolution was improved, acquisition times were greatly reduced; CT scans became part of the clinical routine and modern IR algorithms gained additional complexity.

Iterative reconstruction algorithms may allow a notable dose reduction due to a more precise modeling of the acquisition process. This is expected to support the trend towards continued dose reduction, which is considered a necessity in view of the increasing number of CT examinations in clinical routine. In addition, iterative methods with the ability to include various physical models represent a more intuitive and natural way of image reconstruction. Statistical reconstruction methods, for example, model the counting statistics of detected photons by respective weighting of the measured rays. Other implementations include the modeling of the acquisition geometry or incorporate further information on the x-ray spectra used for improving the simulation of the acquisition process.

The performance of CT scanners is frequently measured using physical phantoms targeting metrics that quantify radiation dose and image quality. These performance evaluations are used to perform quality control tests, develop clinical protocols, accredit devices, or assess the utility of new scanner designs and algorithms. Currently, a number of useful phantoms exist that are targeted to the measurements of image noise, spatial resolution, Hounsfield Unit accuracy, alignement, and detectability. Those include the ACR Accreditation Phantom, the Catphan Phantom and manufacturer-supplied quality control phantoms. Another industry standard phantom, the CT dose index (CTDI) phantom, is used to parameterize CT dose.

Even though these phantoms are of significant value, they fail to capture

the performance aspects of some of the key yet common technological attributes of modern CT systems: image quality performance as a function of body size, tube current modulation, and iterative reconstruction.

The purpose of this study is to evaluate the image quality and dose assessment by using a filtered back projection and iterative reconstruction algorithm. This thesis has been divided in two parts: initially, we analyze the noise power spectrum and the modulation transfer function in both standard and iterative reconstruction. Next we focus on low contrast detectability by make use of two different phantoms. The second part allows us to analyze dose assessment in CT imaging and compare the obtained results with national DLR. This thesis is organized as follows:

- *Chapter 1*: A brief historical introduction to Computed Tomography; fundamentals principles and design; acquisition modes and different configurations; comparison between axial and helical scanning; single-slice and multi-slice technologies.

- *Chapter 2*: Theoretical background of reconstruction algorithms; reconstruction procedure; standard and iterative techniques; state of the art of various manufacturers.

- *Chapter 3*: Noise power spectrum analysis and noise reduction with IR; phantoms and methods used; Modulation transfer function analysis; test device and processing.

- *Chapter 4*: Low-contrast analysis with Catphan 600 and Cirs 061 phantoms.

- *Chapter 5*: Dose assessment; theoretical basis of Computed Tomography Dose Index and Dose Length Product; comparison between FBP, IR and national LDR.

- *Chapter 6*: Conclusions and future evaluations.

Chapter 1

Basics of Computed-Tomography Technology

1.1 A brief history

For the 75 years of x-ray imaging, the detector used in diagnostic radiology, such as radiographic film or image intensifiers, provided reasonably good visualization of high-contrast objects.

However, their ability to record small differences in trasmitted x-ray signals was limited. Several factors contributed to the inability to resolve low-contrast signals. First, large-area detectors record a large amount of scattered radiation, making small differences in x-ray trasmission difficult to resolve. Second, the superposition of the patient's three dimensional information onto a two-dimensional detector obscures low-contrast information.

Introduced clinically in the early 1970s, x-ray computed tomography (CT) overcame many of the difficulties encountered in using large-area detectors. First, the sequential irradiation of slabs of tissues and collimation at the detector markedly reduced the amount of scattered radiation measured. Second, the reconstruction of a tomographic image eliminated much of the problem of overlapping anatomy.
X-ray CT was the first imaging modality that allowed physicians to see the internal structure of a three-dimensional object in cross-section[1][1].

CT differs from the more conventional x-ray tomography in that one uses digital or computer techniques to restore the slice of interest rather than the

[1]CT was rapidly accepted into clinical practice because of its tomographic nature and superior contrast resolution.

analog techniques of deliberately casting unwanted information into out of focus planes on a film moving in a complex prescribed geometrical pattern with the x-ray tube.

The first clinically useful Computed Tomography system was pioneered by Godfrey Hounsfield Fig.[1.1] of EMI Ltd. in England. This system was installed in 1971 in the Atkinson Morley Hospital near London. The EMI scanner arrived on the scene with an impact not unlike that of x-ray systems following Roentgen's discovery in 1895. The scanner developed by Hounsfield in his laboratory took several hours to acquire the raw data for a single scan or "slice"and took days to reconstruct a single image from this raw data.

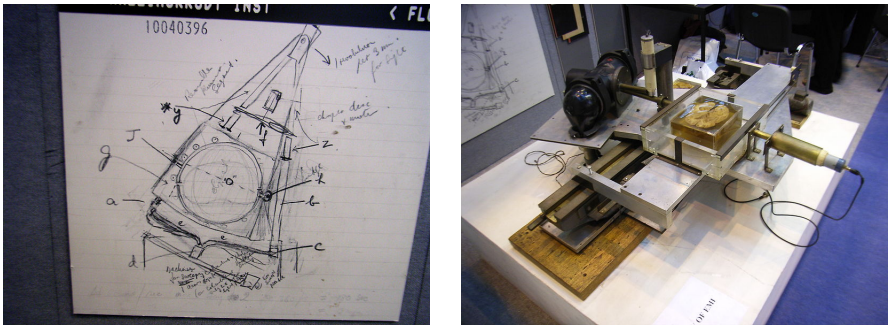

Figure 1.1: Hounsfield's sketch (left), Lithograph of Hounsfield Original Test Lathe, presented to the author on the late 1970s (right).

By the 1975 EMI were marketing a body scanner, the CT5000, the first of which was installed at Northwick Park Hospital in London. The first body scanner in the USA was installed at the Mallinkrodt Institute and had its first clinical use in October 1975. By this time, scan time had been reduced to 20 seconds, for a 320x320 image matrix.

The mid-1970s were a time of rapid development in CT: 1976 saw 17 companies offering scanners, with scan times down to 5 seconds in some cases. By 1978, there was an installed base of around 200 scanners in the USA, image matrix size were up to 512x512 and some models of scanner had the capability of ECG-triggered scans. By the end of the 1970s the importance of CT scanning to medicine was clear: Hounsfield and Cormack received the Nobel Prize for medicine in 1979.

The 1980s saw incremental development of CT scanner technology: short scan times and matrix sizes, until by the late 1980s scan time were down to only 3 seconds. Development continued through the 1990s, with the introduction of spiral scanning in the early 1990s and the development of multi-slice scanners, with 4-slice scanners and 0.5 seconds scan times being 'state of the art' by the end of the century.

Development of CT scanner technology continued through the early years of 21st century, particularly with multi-slice scanners. High-end scanners were offering up to 320 slices, dual-source and dual-energy x-ray sources and iterative reconstruction algorithm.

The latest multi-slice CT systems can collect up to 640 slices of data in about 300 ms and reconstruct a 512× 512 matrix image from millions of data points in less than a second. An entire chest can be scanned in five to ten seconds using the most advanced multi-slice CT system.

During its 40-year history, CT has made great improvements in speed, patient comfort, and resolution. A CT scan times have gotten faster, more anatomy can be scanned in less time. Faster scanning helps to eliminate artifacts from patient motion such as breathing or peristalsis. Tremendous research and development has been made to provide excellent image quality for diagnostic confidence at the lowest possible x-ray dose[2].

Figure 1.2: A modern CT Scanner, Philips Brilliance 64 CT Scanner.

1.2 Fundamentals principles and Design

Computed Tomography (CT) is a non invasive medical examination or procedure that utilized specialized x-ray equipment to produce cross-sectional images of the body. Each cross-sectional images represents a “slices”of the person being imaged.

These cross-sectional images are used for a variety of diagnostic and therapeutic purposes. CT scans can be performed on every region of the body for a variety of reasons (e.g., diagnostic, treatment planning, interventional).

CT images of internal organs, bones, soft tissue, and blood vessels provide greater clarity and more details than conventional x-ray images, such as a chest x-ray.

The value in a CT slice image correspond to x-ray attenuation, which reflects the proportion of x-rays scattered or absorbed as they pass through each voxel. X-ray attenuation is primarily a function of x-ray energy and the density and composition of the material being imaged.

Tomographic imaging consists of directing x-rays at an object from multiple orientations and measuring the decrease in intensity along a series of linear paths. This decrease is characterized by Lambert-Beer's Law, which describes intensity reduction as a function of x-ray energy, path length, and material linear attenuation coefficient. A specialized algorithm [see Chapter 2] is then used to reconstruct the distribution of x-ray attenuation in the volume being imaged[3][4].

The simplest form of Lambert-Beer's law for a monochromatic x-ray beam through a homogeneus material is

$$I = I_0 \exp[-\mu x] \tag{1.1}$$

where I_0 and I are the initial and the final x-ray intensity, μ is a material's linear attenuation coefficient and x is the length of the x-ray path. If there are multiple materials, the equation becomes

$$I = I_0 \exp\Big[\sum_i (-\mu_i x_i)\Big] \tag{1.2}$$

where each increment i reflects a single material with attenuation coefficient μ_i with linear extent x_i. In a well-calibrated system using a monochromatic x-ray source (i.e. synchrotron or gamma-ray emitter) this equation can be solved directly.

If a polychromatic x-ray source is used, to take into account the fact that the attenuation coefficient is a strong function of x-ray energy, the complete solution would require solving the equation over the range of the x-ray energy *(E)* spectrum utilized

$$I = \int I_0(E) \exp\Big[\sum_i (-\mu_i(E) x_i)\Big] dE \tag{1.3}$$

However, such a calculation is usually problematic, as most reconstruction strategies solve for a single μ value at each spatial position. In such cases, μ is taken as an effective linear attenuation coefficient, rather than an absolute. This complicates absolute calibration, as effective attenuation is a function of

both the x-ray spectrum and the properties of the scan object. It also leads to beam-hardening artifacts: changes in image value caused by preferential attenuation of low-energy x-rays[5].

There are a number of methods by which the x-ray attenuation data can be converted into an image. The most frequent approach in CT imaging is called "filtered backprojection"[see Chapter 2], in which the linear data acquired at each angular orientation are convolved with a specially designed filter and then backprojected across a pixel field at the same angle.

This principle is illustrated in Fig.[1.3]. A hand sample of garnet-biotite-kyanite schist (top left) is rotated, and its midsection is imaged with a planar fan beam (blue). The attenuation of x-rays by the sample as it rotates is shown in the upper right; the more attenuation there is along a beam path leading from the point source (bottom) to the linear detector (top), the fewer x-rays reach the detector. The data collected at each angle are compiled in the bottom right. In this image the horizontal axis corresponds to detector channel, and the vertical axis corresponds to rotation angle (or time), and brightness corresponds to the extent of x-ray attenuation. The resulting image is called a sinogram, as any point in the original object corresponds to a sine curve. After data acquisition is complete, reconstruction begins. Each row of the sinogram is first convolved with a filter, and projected across the pixel matrix (bottom right) along the angle at which it was acquired. Once all angles have been processed, the image is complete.

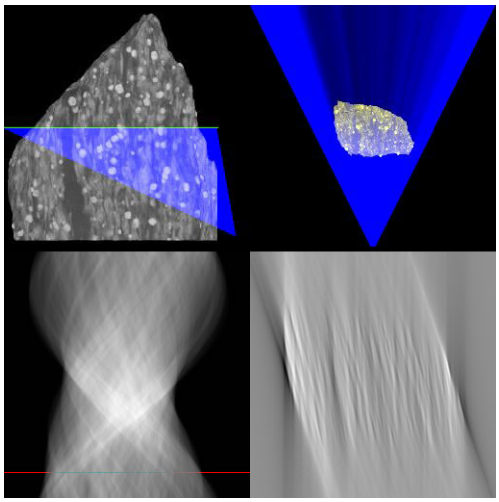

Figure 1.3: Sample of garnet-biotite-kyanite schist.

CT-Scanner hardware is designed to determine effective x-ray attenuation coefficients at each point within a volume of interest from transmission

measurements acquired at multiple angles through the object. A set of transmission measurements through the object at a given angle is known as a *projection*. This projection measurements are mathematically combined to form a two-dimensional representation of a three-dimensional object.
So, while a typical digital image is composed of pixels (picture elements), a CT slice image is composed of voxels (volume elements).

The scanner is made up of three primary systems, including the gantry, the computer, and the operating console. Each of these is composed of various subcomponents.

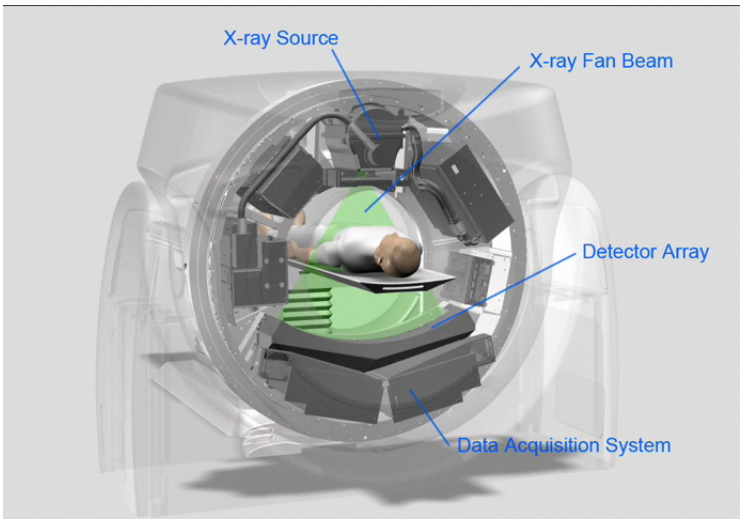

Figure 1.4: Gantry virtual view.

The gantry assembly is the largest of these systems. It is made up of all the equipment related to the patient, including the patient support, the positioning couch, the mechanical supports, and the scanner housing. It also contains the heart of the CT scanner, the x-ray tube, as well as detectors which respectively generate and detect x-rays.

The gantry is the 'donut' shaped part of the CT scanner that houses the components necessary to produce and detect x-rays to create a CT image. The x-ray tube and detectors are positioned opposite each other and rotate around the gantry aperture. Continous rotation in one direction without cable wrap around is possible due to the use of slip rings.
The following images are of a Toshiba Aquilion 16 CT scanner with the external and internal components of the gantry.

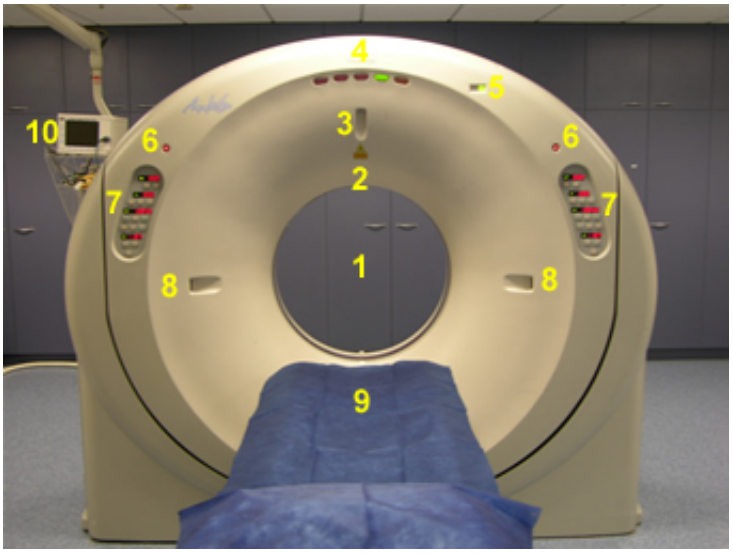

Figure 1.5: Gantry External view.

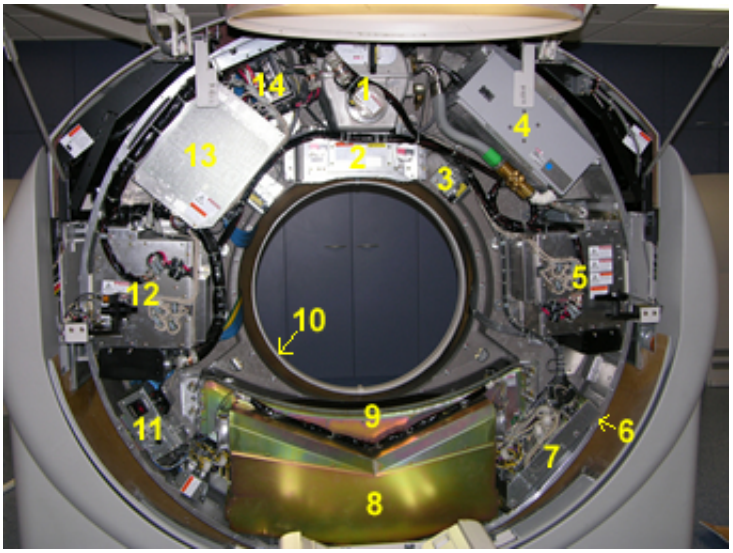

Figure 1.6: Gantry Internal view.

NUM.	Gantry External View	Gantry Internal view
1	*Gantry Aperture(720mm diameter)*	*X-Ray tube*
2	*Microphone*	*Filters, collimator, reference detector*
3	*Sagittal laser alignment light*	*Internal Projector*
4	*Patient guide lines*	*X-ray tube heat exchanger (oil cooler)*
5	*X-ray exposure indicator light*	*High voltage generator (0-75 kV)*
6	*Emergency stop buttons*	*Direct drive gantry monitor*
7	*Gantry control panels*	*Rotation Control Unit*
8	*External laser alignment lights*	*Data Acquisition system (DAS)*
9	*Patient couch*	*Detectors*
10	*ECG gating monitor*	*Slip rings*
11	*-None-*	*Detector temperature controller*
12	*-None-*	*High voltage generator (75-150 kV)*
13	*-None-*	*Power unit*
14	*-None-*	*Line noise filter*

Table 1.1: Internal and External CT components (Toshiba Aquilion 16 CT scanner).

1.3 Acquisition Modes

1.3.1 Configurations

Planar Fan Beam Configuration

The diagram in Fig.[1.7] illustrates some of the most common configurations for CT scanners. In planar beam scanning, x-rays are collimated and measured using a linear detector array. Typically, slice thickness is determined by the aperture of the linear array. Collimation is necessary to reduce the influence of X-ray scatter, which results in spurious additional x-rays reaching the detector from locations not along the source-detector path. Linear arrays can generally be configured to be more efficient than planar ones, but have the drawback that they only acquire data for one slice image at a time.

Cone Beam Configuration

In cone-beam scanning, the linear array is replaced by a planar detector, and the beam is no longer collimated. Data for an entire object, or a considerable thickness of it, can be acquired in a single rotation. The data are reconstructed into images using a cone-beam algorithm. In general, cone-beam data are subject to some blurring and distortion the further one goes from the central plane that would correspond to single-slice acquisition. They are also more subject to artifacts stemming from scattering if high-energy x-rays are utilized. However, the advantage of obtaining data for hundreds or thousands of slices at a time is considerable, as more acquisition time can be spent at each turntable position, decreasing image noise. In this thesis we used this configuration to do our acquisitions.

Parallel Beam Configuration

Parallel-beam scanning is done using a specially configured synchrotron beam line as the x-ray source. In this case, volumetric data are acquired and there is no distortion. However, the object size is limited by the width of the x-ray beam; depending on beam line configuration, objects up to 6 cm in diameter may be imaged. Synchrotron radiation generally has very high intensity, allowing data to be acquired quickly, but the x-rays are generally low-energy (< 35 keV), which can preclude imaging samples with extensive high-Z materials.

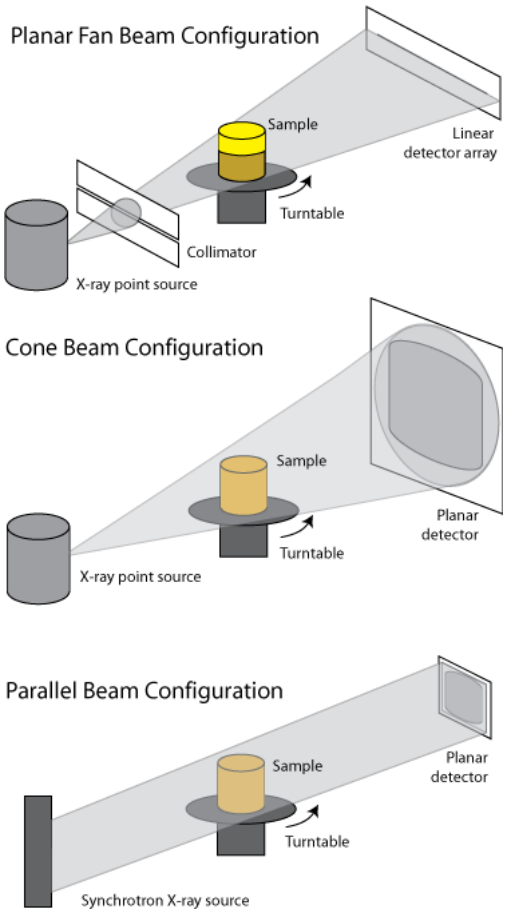

Figure 1.7: Some of the most common configurations for CT scanners.

1.3.2 X-ray tube in various generations of CT

The great majority of CT systems use x-ray tubes, although tomography can also be done using a synchrotron or gamma-ray emitter as a monochromatic x-ray source. Important tube characteristics are the target material and peak x-ray energy, which determine the x-ray spectrum that is generated; current, which determines x-ray intensity; and the focal spot size, which impacts spatial resolution.

Most CT x-ray detectors utilize scintillators. Important parameters are scintillator material, size and geometry, and the means by which scintillation events are detected and counted. In general, smaller detectors provide better image resolution, but reduced count rates because of their reduced area compared to larger ones. To compensate, longer acquisition times are used to reduce noise levels.

First Generation

CT scanners used a pencil-thin beam of radiation. The images were acquired by a "translate-rotate" method in which the x-ray source and the detector in a fixed relative position move across the patient followed by a rotation of the x-ray source/detector combination (gantry) by 1 for 180. The thickness of the slice, typically 1 to 10 mm, is generally defined by pre-patient collimation using motor driven adjustable wedges external to the x-ray tube. This generation used axial platforms.

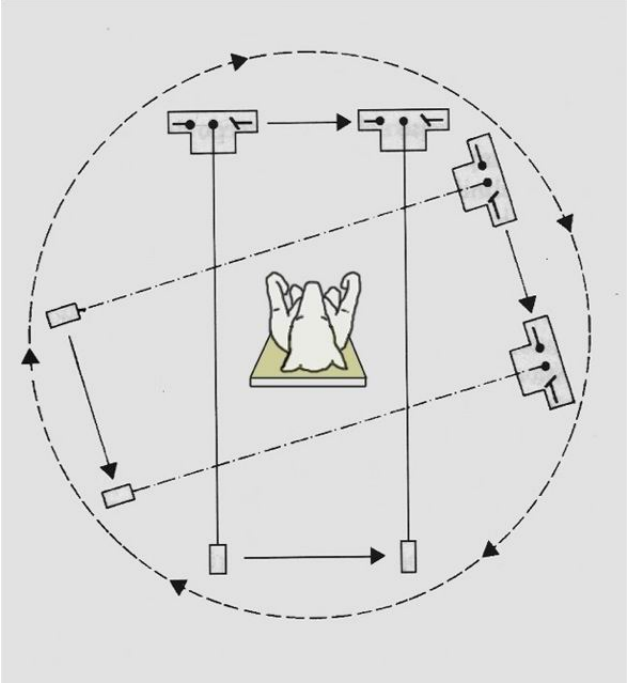

Figure 1.8: A representation of first generation CT scanner (Parallel Beam, Translate-Rotate).

Second Generation

The x-ray source changed from the pencil-thin beam to a fan shaped beam.

The "translate-rotate" method was still used but there was a significant decrease in scanning time. Rotation was increased from one degree to thirty degrees. Because rotating anode tubes could not withstand the wear and tear of rotate-translate motion, this early design required a relatively low output stationary anode x-ray tube.

The power limits of stationary anodes for efficient heat dissipation were improved somewhat with the use of asymmetrical focal spots (smaller in the

scan plane than in the z-axis direction), but this resulted in higher radiation doses due to poor beam restriction to the scan plane. Nevertheless, these scanners required slower scan speeds to obtain adequate x-ray flux at the detectors when scanning thicker patients or body parts. This generation used axial platforms.

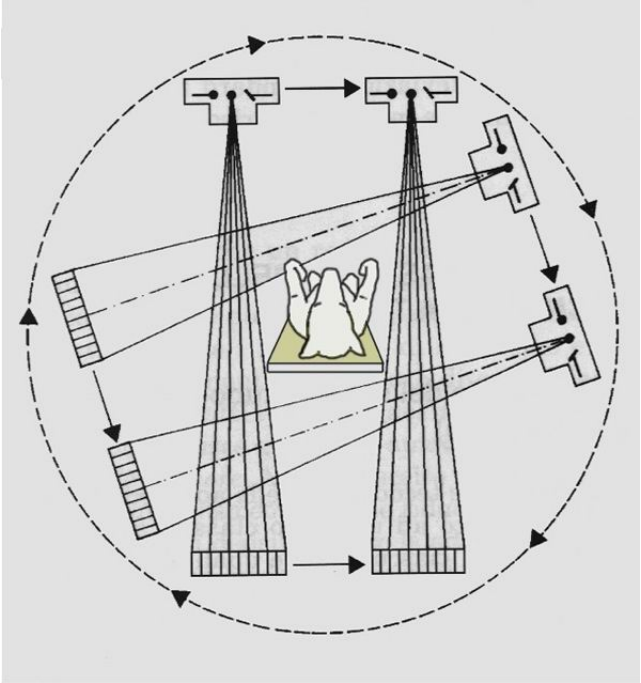

Figure 1.9: A representation of second generation CT scanner (Fan Beam, Translate-Rotate).

Third Generation

Designers realized that if a pure rotational scanning motion could be used rather than the slam-bang translational motion, then it would be possible to use higher-power (output), rotating anode x-ray tubes and thus improve scan speeds in thicker body parts in which the 3rd generation become a Rotate-Rotate geometry.
A typical machine employs a large fan beam such that the patient is completely encompassed by the fan, the detector elements are aligned along the arc of a circle centered on the focus of the x-ray tube. The x-ray tube and detector array rotate as one through 360 degrees, different projections are obtained during rotation by pulsing the x-ray source, and bow-tie shaped filters are chosen to suit the body or head shape by some manufacturers to control excessive variations in signal strength.

Such filters generally attenuate the peripheral part of the divergent fan beam to a greater extent than the central part. It also helps overcome the effects of beam hardening and to minimize patient skin dose in the peripheral part of the field of view.

A number of variants on this geometry have been developed, which include those based on offsetting the centre of rotation and the use of a flying focus x-ray tube. This generation used axial/helical platforms.

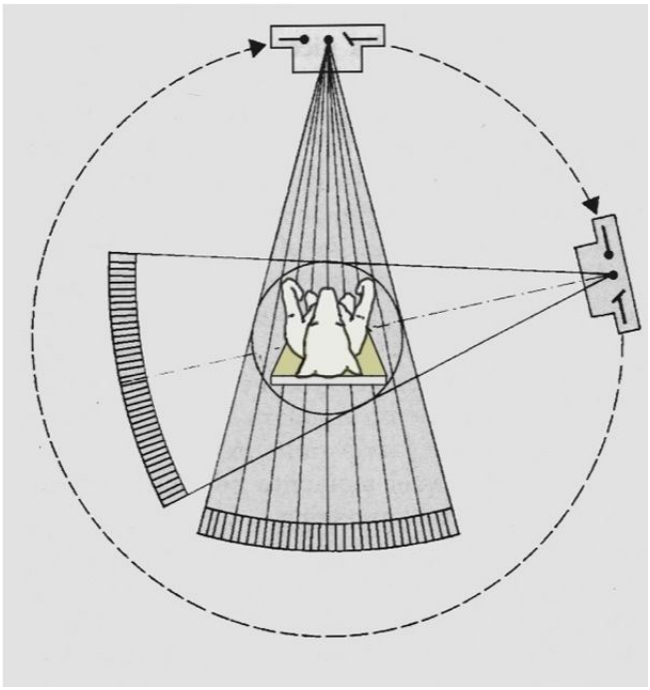

Figure 1.10: A representation of third generation CT scanner (Fan Beam, Rotate only).

Fourth Generation

Fourth generation of CT scanner uses Rotate-Fixed Ring geometry where a ring of fixed detectors completely surrounds the patient. The X-ray tube rotates inside the detector ring through a full 360 degrees with a wide fan beam producing a single image. Due to the elimination of translate-rotate motion the scan time is reduced comparable with third generation scanner, initially, to 10 seconds per slice but the radiographic geometry is poor because the X-ray tube must be closer to the patient than the detectors, i.e. the geometric magnification is large also scatter artifact is more than third generation since they cannot use anti-scatter grid.

The disadvantages of poor geometry noted above have been alleviated very neatly by the so called nutating geometry. The X-ray tube is external to the detector ring but slightly out of the detector plane, this change resulted in increasing both the acquisition speed, and image resolution[6]. The method of scanning was still slow, because the X-ray tube and control components interfaced by cable, limiting the scan frame rotation. Further, they were more sensitive to artifacts because the non-fixed relationship to the x-ray source made it impossible to reject scattered radiation. This generation use axial/helical platforms.

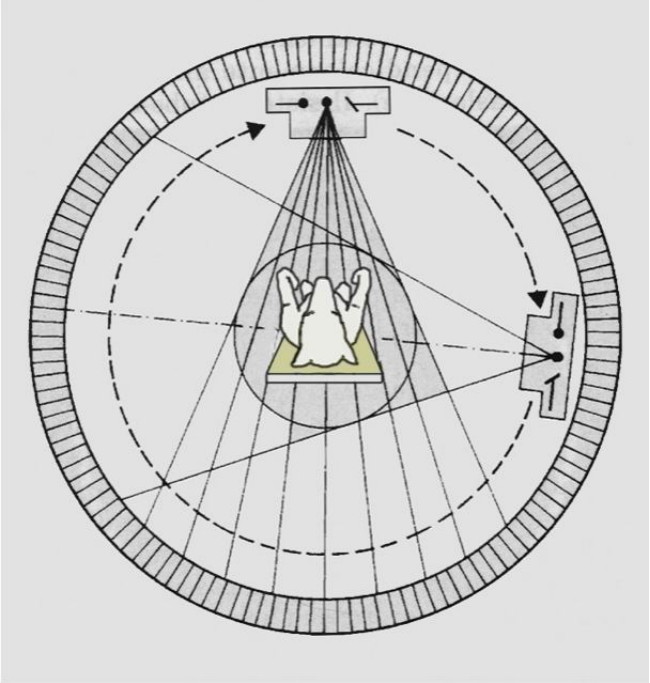

Figure 1.11: A representation of fourth generation CT scanner (Fan Beam, stationary circular detector).

Several other CT scanner geometries which have been development (fifth and sixth generation) and marketed do not precisely fit the above categories. In the next section we will see the two basic modes for CT acquisition.

1.3.3 Axial CT Scanning vs Helical CT Scanning

After the third generation, CT technology remained stable until 1987. By then, CT examinations times were dominated by interscan delays. After each 360 rotation, cables connecting rotating components to the rest of the gantry required that rotation stop and reverse direction (Slip Ring).

Scanning, breaking and reversal required at least 8-10 s, of which only 1-2 were spent acquiring data. The result were poor temporal resolution and long procedure times.

Axial (sequential) scanning

In this scan mode, the patient table remains stationary while the tube and detector array rotate once around the patient, collecting the necessary data for image recontruction. After one rotation, the patient table is moved along the z axis to the next position and another set of scan data are acquired. If projection through the entire organ of interest can be acquired in one rotation, such as with 16 cm wide detector arrays, then no table translation is required.

In single detector row, the image thickness is determined primarly by the collimation of the x-ray beam along the z axis, and one wide detector array was used to acquire different slice thicknesses.

In multi detector scanners (MDCT), the image thickness is determined by the detector element dimensions; the data from adjacent detector rows can be added together to give wider image thickness and a range of different slice thickness can be acquired simultaneously.

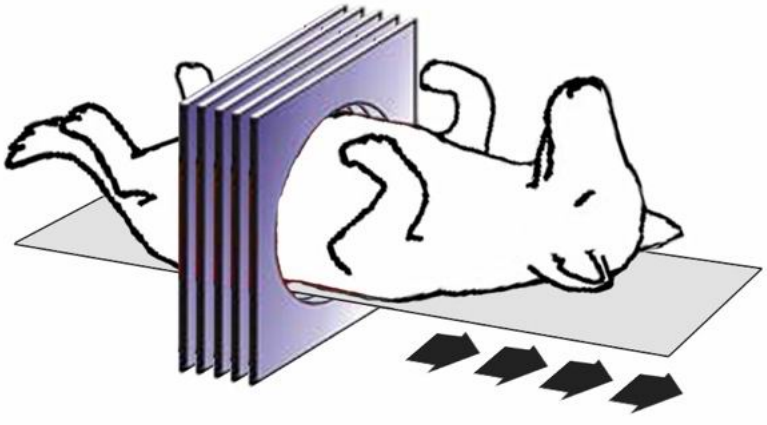

Figure 1.12: Artistic representation of axial CT.

Helical (spiral) scanning

Spiral scanning involves continuous translation of the patient table with continuous x-ray rotation and data collection. This decreases overall scan time, and can allow scanning of the entire adult torso within a breath hold. The major advantage of spiral scanning is the volume of coverage for a given rotation of x-ray exposure.

With the introduction of spiral scanning, the slice is not so simply defined by the x-ray collimation; rather, the nature of the moving table requires interpolation schemes to provide estimates of information within a given slice. This information acquired in an acquisition which includes information from the slice above and below the slice interest and then interpolates the data to establish an effective slice at a given position.

In helical scanning, extra rotations of data acquisition are required at the beginning and end of the scan in order to provide sufficient data for image reconstruction at the edges of the prescribed scan range.

Eliminating interscan delays required continuous rotation and the strategy is to continuously rotate and acquire data as the table moving though the gantry. The resulting trajectory of the tube and detectors relative to the patient traces out a helical or spiral path. This powerful concept allows for rapid scans of entire z-axis regions of interest.

Certain concepts associated with helical CT are fundamentally different from those of axial scanning. One such concept is how fast the table slides through the gantry relative to the rotation time and slice thicknesses being acquired. This aspect is referred to as the helical *pitch* and is defined as the table movement per rotation divided by the slice thickness[7].

To understand this concept we consider an MSCT scanner with n arrays that have a thickness T (at isocenter), the beam width a as measured at the isocenter is given by

$$a = nT + \eta \tag{1.4}$$

where η is the over-beaming that is necessary in MSCT systems. The η portion of the beam corrsponds to the width of the penumbra on both sides of the active beam, which extends beyond the edges of the active detector arrays *(nT)* to reduce artifacts. Then, the pitch is defined by

$$p = \frac{b}{nT} \qquad [mm] \tag{1.5}$$

where b is the ratio of the table feed.

The choice of pitch is examination dependent, involving a trade-off between coverage and accuracy.

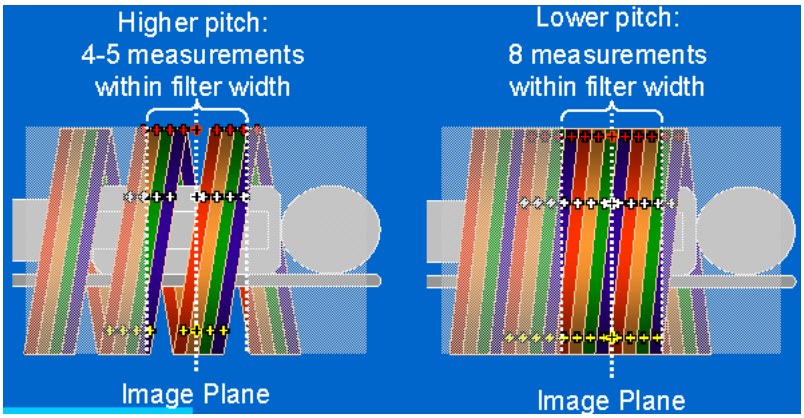

Figure 1.13: Comparison between higher pitch and lower pitch[7].

In single detector row CT, as the pitch is increased, the data sampling along z is more sparse, and the result image is wider[2][Fig. 1.13]. Image noise is not affected, however, as the same number of projections is always used to form an image.

In multi detector row CT, scanners use spiral interpolation algorithms that are different than those in single detector, and take advantage of the multiple rings of transmission data. For MDCT, the width of the section sensitivity profile remains relatively constant as the pitch changes.

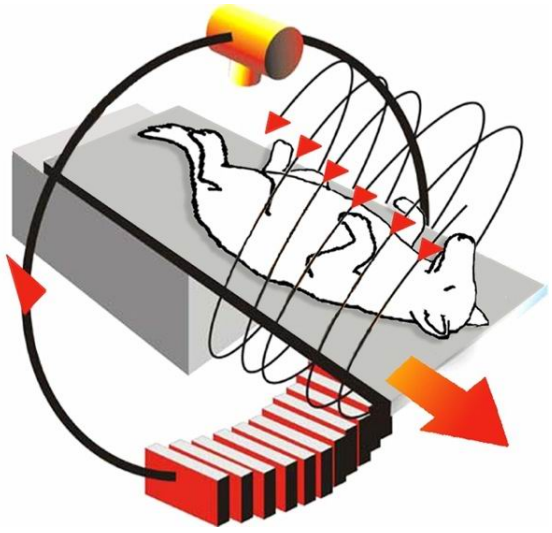

Figure 1.14: Artistic representation of spiral CT.

[2]If the slice thickness is 10 mm and the table moves 15 mm during one tube rotation, then the pitch $= \frac{15}{10} = 1.5$.

1.3.4 Difference between SSCT and MSCT

The principal difference between single-slice CT (SSCT) and multi-slice CT (MSCT) are:

- Primary difference is in the design of the detector arrays, as illustrated in Fig.[1.16].
- Secondary difference is that MSCT offer a potentially thinner slice that can be achieved by physical and/or electronic collimation.
- MSCT offer a better defined sensitivity profile Fig.[1.15].

Single-Slice CT

SSCT detector arrays are one dimensional; that is, they consist of a large number (typically 750 or more) of detector elements in a single row across the irradiated slice to intercept the x-ray fanbeam. In the slice thickness direction (z-direction), the detectors are monolithic, that is, single elements long enough (typically about 20 mm) to intercept the entire x-ray beam width, including part of the penumbra.

In SSCT, slice thickness is determined by prepatient and possibly post-patient x-ray beam collimators. Generally, the x-ray beam collimation was designed such that the z-axis width of the x-ray beam at the isocenter (i.e., at the center of rotation) is the same as the desired slice thickness. (The x-ray beam width, usually defined as the full width at half maximum (FWHM) of the z-axis x-ray beam intensity profile).

The interpolation process tends to create slice where the FWHM is often matched to the nominal slice width, but the area tails of the slice extend the sensitivity profile significantly into the neighboring slices, and much beyond the normal slice width.

Multi-Slice CT

In a multi slice CT, the key factor is that the x-ray collimation allows simultaneous radiation of several adjoining z-axis slices at the same time. This significantly enhances x-ray tube utilization. In MSCT, each of the individual, monolithic SSCT detector elements in the z-direction is divided into several smaller detector elements, forming a 2-dimensional array. Rather than a single row of detectors encompassing the fan beam, there are now multiple, parallel rows of detectors.

In MSCT, however, slice thickness is determined by detector configuration and x-ray beam collimation. Because it is the length of the individual

detector (or linked detector elements) acquiring data for each of the simultaneously acquired slices that limits the width of the x-ray beam contributing to that slice, this length is often referred to as detector collimation.

The installation of MSCT scanners providing 16 data channels for 16 simultaneously acquired slices began in 2002. In addition to simultaneously acquiring up to 16 slices, the detector arrays associated with 16-slice scanners were redesigned to allow thinner slices to be obtained as well.

One potential problem for the multi-slice system is that a wider area is scanned at one time, and therefore more scattered radiation per slice is generated affecting deleteriously both image quality and radiation dose. The collimator and detector design must be optimized for MSCT and may need to compensate for x-ray movements in the longitudinal direction by allowing a wider beam than the actual slice thickness, thus impacting deleteriously on dose buildup from neighboring slices.

Detector arrays for various 16-slice scanner models are illustrated in Fig.[1.17]. Note that in all of the models, the innermost 16 detector elements along the z-axis are half the size of the outermost elements, allowing the simultaneous acquisition of 16 thin slices (from 0.5 mm thick to 0.75 mm thick, depending on the model). When the inner detectors were used to acquire submillimeter slices, the total acquired z-axis length and therefore the total width of the x-ray beam ranged from 8 mm for the Toshiba version to 12 mm for the Philips and Siemens versions. Alternatively, the inner 16 elements could be linked in pairs for the acquisition of 16 thicker slices.

By 2005, 64 slice scanners were announced, and installations by most manufacturers began. Detector array designs used by several manufacturers are illustrated in Fig.[1.18]. The approach used by our manufacturer (Philips) for 64 slice detector array designs was to lengthen the arrays in the z-direction and provide all submillimeter detector elements: 64×0.625 mm (total z-axis length of 40 mm).

In addition to the simultaneous acquisition of more slices, MSCT x-ray beam widths can be considerably wider than those for SSCT. Sixteen slice MSCT beam widths are up to 32 mm; 64-slice beams can be up to 40 mm wide; and even wider beams are used in systems currently under development or in clinical evaluation. A possible consequence is that more scatter may reach the detectors, compromising low-contrast detection. Generally, however, the antiscatter septa traditionally used with third generation CT scanners can be made sufficiently deep to remain effective with MSCT.

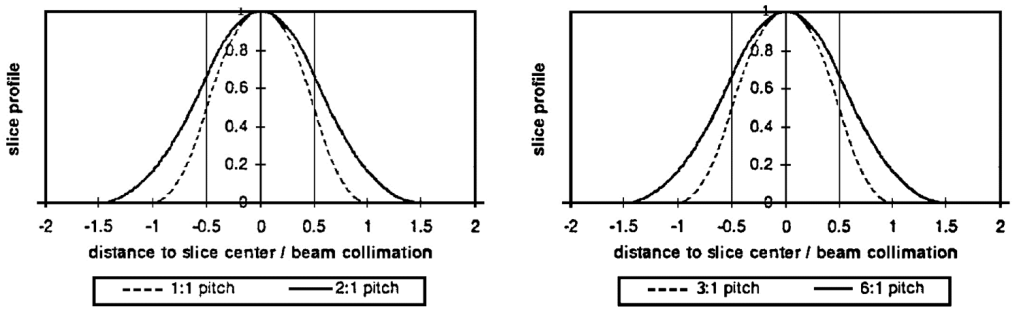

Figure 1.15: Spiral Slice Sensitivity Profile (SSP) of SSCT in Spiral Mode (LEFT); As the pitch increases, SSP curves deviate more and more from an ideal square wave (-0.5 to 0.5) more similar to conventional (non-spiral) CT. Spiral Slice Sensitivity Profile of MSCT in Spiral Mode (RIGHT); Fractional pitch of multislice leads to better approximation of SSCT, more similar to ideal square wave (-0.5 to 0.5)[1].

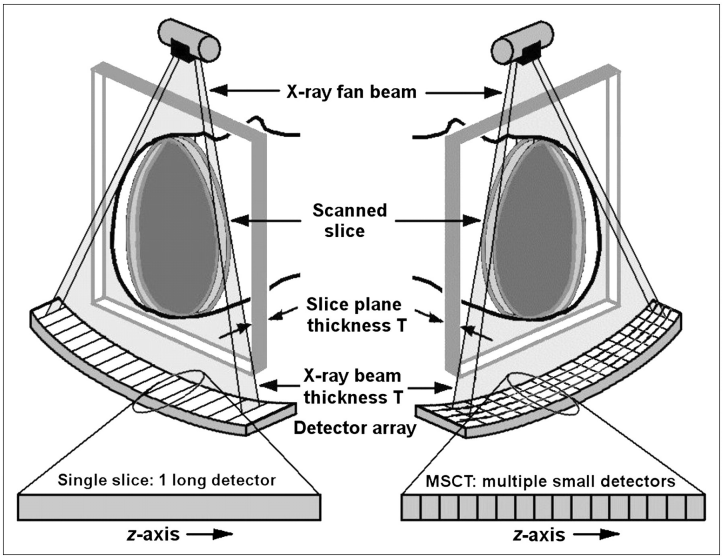

Figure 1.16: SSCT arrays containing single, long elements along z-axis (Left). MSCT arrays with several rows of small detector elements (Right)[8].

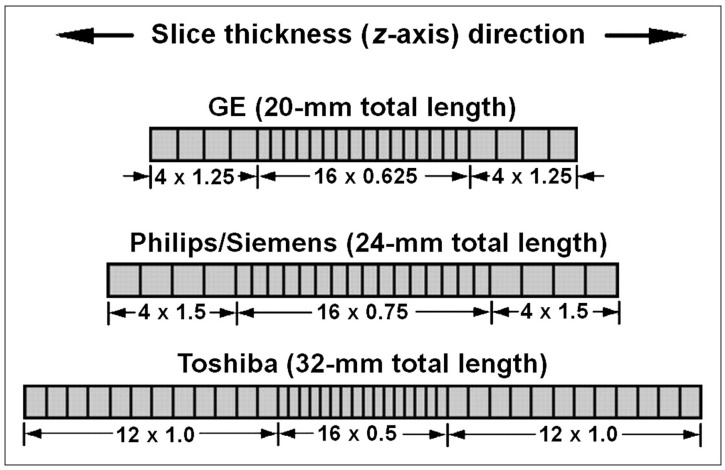

Figure 1.17: Diagrams of various 16-slice detector designs (in z-direction). Innermost elements can be used to collect 16 thin slices or linked in pairs to collect thicker slices[8].

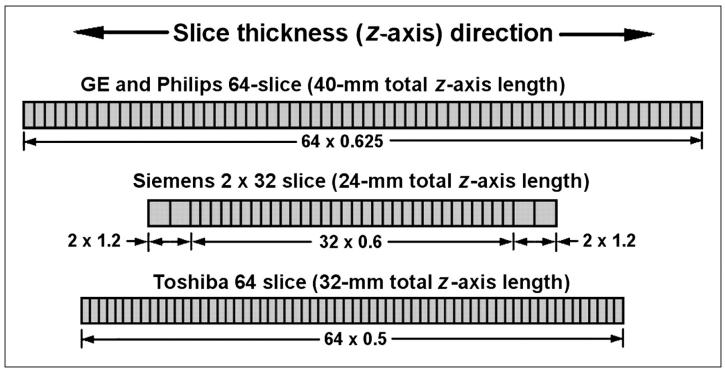

Figure 1.18: Diagrams of various 64-slice detector designs (in z-direction). Most designs lengthen arrays and provide all submillimeter elements. Siemens scanner uses 32 elements and dynamic-focus x-ray tube to yield 2 measurements per detector[8].

Chapter 2

Reconstruction Algorithms

2.1 Theoretical background

X-ray CT imaging is a procedure to get images of thin slice of an unknown object, such as biological tissue, from the projection data collected by illuminating the object from many different directions using x-ray. The object can be represented by its distribution of x-ray attenuation coefficient1.2. When a parallel beam of x-rays propagates through the object, the total attenuation of the beam can be expressed by a line integral, which is the well-known Radon transform.

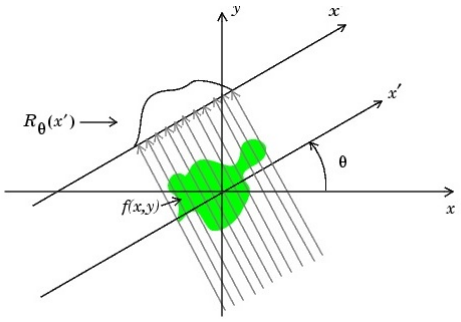

Figure 2.1: Radon Transform.

The Radon transform(2.1) of an image represented by the function *f(x,y)* can be defined as a series of line integrals trough *f(x,y)* at different offsets from the origin. It is defined as

$$R(p,\tau) = \int_{-\infty}^{\infty} f(x, px + \tau)dx \tag{2.1}$$

where p and τ are the slope and intercepts of the line. A more directly applicable form of the transform can be defined by using a delta function

$$R(r,\theta) = \int_{-\infty}^{\infty}\int_{-\infty}^{\infty} f(x,y)\delta(x\cos\theta + y\sin\theta - r)dxdy \tag{2.2}$$

where *f(x,y)* denotes the object, *R(r,θ)* denotes the projection data when the scanning angle is θ and the distance between the projection line and the origin is r (the perpendicular offset of the line); δ denotes the Dirac delta function, the term between brackets represents a projection line of x-rays. The acquisition of data in medical imaging techniques such as MRI, CT and PET scanners involves a similar method of projecting a beam through the object, and the data is in a similar form to that described in the eq.(2.2).

The plot of the Radon transform, or scanner data, is referred to as a sinogram due to its characteristic sinusoid shape. Next figure shows a simple head phantom and the sinogram created by taking the Radon transform at intervals of one degree from 0 to 180 degrees.

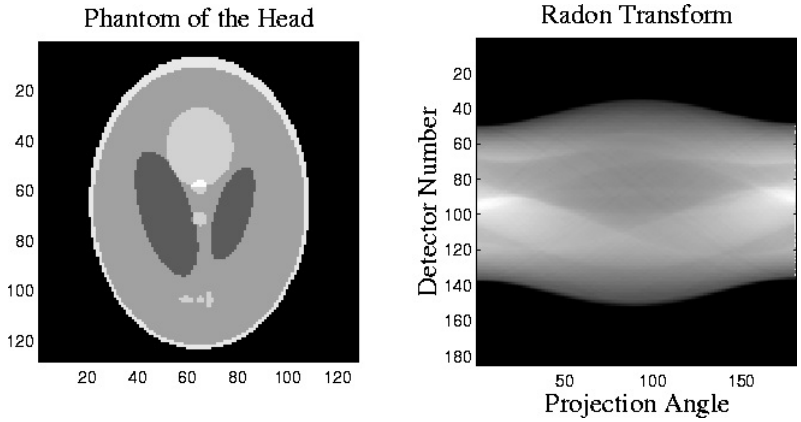

Figure 2.2: The Shepp-Logan head phantom (left) and its Radon Transform (right).

Unfortunately, the actual data detected by a medical imaging system does not correspond exactly to the Radon transform of the "true "image. In any imaging system, projection data will be corrupted by noise, and the projections are measured with only limited resolution. The geometry of the imaging system may differ from the ideal, particularly in transmission tomography, where a fan beam imaging system is more easily implemented than a parallel-beam system.

2.1.1 Reconstruction Procedure

Computed tomography (CT) reconstruction is computationally demanding, but by applying the latest high performance processors and advanced software programming techniques, it's possible to reign in processing times. With the resulting performance gains, CT scanners operate faster while also enhancing image quality and increasing acquisition flexibility. These advances in CT imaging enable radiologists and department managers to improve patient care, reduce the time to diagnosis and boost the department's productivity.

This procedure is very important for CT imaging. The properties of the final reconstructed image strongly depends upon reconstruction algorithm used[9]. Image reconstruction has a fundamental impact on image quality and therefore on radiation dose.

For a given radiation dose it is desirable to reconstruct images with the lowest possible noise without sacrificing image accuracy and spatial resolution. Reconstruction algorithms that improve image quality can be translated into a reduction of radiation dose because images of acceptable quality can be reconstructed at lower dose[18].

There are many approch to reconstruction algorithms; in the literature a large number of acronyms can be found. Unfortunately these acronyms are not always used consistently in the literature and a number of variations and combinations of different concepts exist.

We divide these in four approaches to calculating the slice image given the set of its views. These are called CT reconstruction algorithms.

- Solving many simultaneous linear equations.
- Fourier Reconstruction.
- Filtered Back Projection (FBP).
- Iterative Techniques.

Solving many simultaneous linear equations

One equation can be written for each measurement. That is, a particular sample in a particular profile is the sum of a particular group of pixels in the image. To calculate N^2 unknown variables (i.e., the image pixel values), there must be N^2 independent equations, and therefore N^2 measurements. Most CT scanners acquire about 50% more samples than rigidly required by this analysis.

For example, to reconstruct a 512× 512 image, a system might take 700 views with 600 samples in each view. By making the problem overdetermined in this manner, the final image has reduced noise and artifacts. The problem with this first method of CT reconstruction is computation time. Solving several hundred thousand simultaneous linear equations is a crazy thing.

Fourier Reconstruction

In the spatial domain, CT reconstruction involves the relationship between a 2D image and its set of 1D views. By taking the 2D Fourier transform of the image and the one-dimensional Fourier transform of each of its views, the problem can be examined in the frequency domain. As it turns out, the relationship between an image and its views is far simpler in the frequency domain than in the spatial domain. The frequency domain analysis of this problem is a milestone in CT technology called the *Fourier slice theorem*[1].

Fig.[2.3] shows how the problem looks in both the spatial and the frequency domains. In the spatial domain, each view is found by integrating the image along rays at a particular angle. In the frequency domain, the image spectrum is represented in this illustration by a two dimensional grid. The spectrum of each view (a one dimensional signal) is represented by a dark line superimposed on the grid. As shown by the positioning of the lines on the grid, the Fourier slice theorem states that the spectrum of a view is identical to the values along a line (slice) through the image spectrum. For instance, the spectrum of view 1 is the same as the center column of the image spectrum, and the spectrum of view 3 is the same as the center row of the image spectrum. Notice that the spectrum of each view is positioned on the grid at the same angle that the view was originally acquired. All these frequency spectra include the negative frequencies and are displayed with zero frequency at the center.

Fourier reconstruction of a CT image requires three steps. First, the one dimensional FFT is taken of each view. Second, these view spectra are used to calculate the two dimensional frequency spectrum of the image, as outlined by the Fourier slice theorem. Since the view spectra are arranged radially, and the correct image spectrum is arranged rectangularly, an interpolation routine is needed to make the conversion. Third, the inverse FFT is taken of the image spectrum to obtain the reconstructed image[11].

Unfortunately this method suffer from artifacts due to interpolation in Fourier plane and aliasing[2].

[1]The Fourier Slice Theorem describes the relationship between an image and its views in the frequency domain.

[2]All the frequency domain information of a band-limited function is contained in an

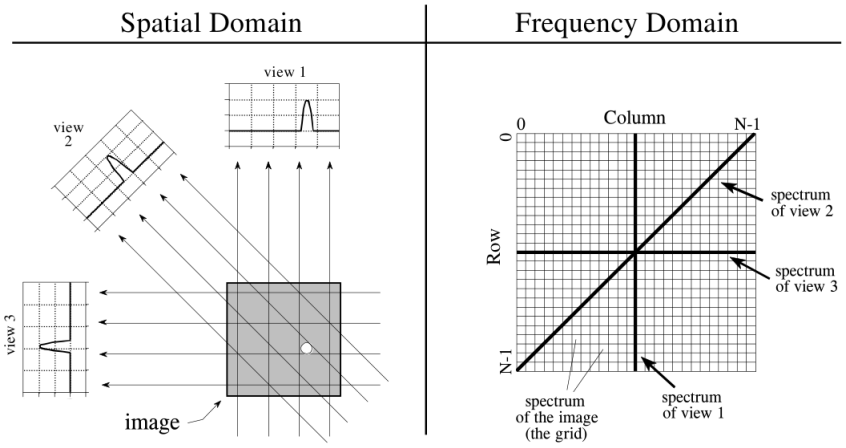

Figure 2.3: The Fourier slice theorem. In the spatial domain, each view is found by integrating the image along rays at a particular angle. In the frequency domain, the spectrum of each view is a one dimensional slice of the two dimensional image spectrum.

Filtered Backprojection

FBP is the most important analytical scheme for image recontruction that is currently widely used on clinical CT scanners because of their computational efficiency and numerical stability. Many FBP-based methods have been developed for different generations of CT data-acquisition geometries, from axial parallel and fan beam CT in the 1970s and 1980s to current multi-slice helical CT and cone-beam CT with large area detectors.

This method is a modification of an older technique, called *backprojection* or *simple backprojection*. Fig.[2.4] shows that simple backprojection is a common sense approach, but very unsophisticated. An individual sample is backprojected by setting all the image pixels along the ray pointing to the sample to the same value. In less technical terms, a backprojection is formed by smearing each view back through the image in the direction it was originally acquired. The final backprojected image is then taken as the sum of all the backprojected views.

While backprojection is conceptually simple, it does not correctly solve the problem. As shown in Fig.[2.4b], a backprojected image is very blurry. A singlepoint in the true image is reconstructed as a circular region that decreases in intensity away from the center. In more formal terms, the point spread function of backprojection is circularly symmetric, and decreases as the reciprocal of its radius.

interval. If this interval is not satisfied, the transform in this interval is corrupted by contributions from adjacent periods.

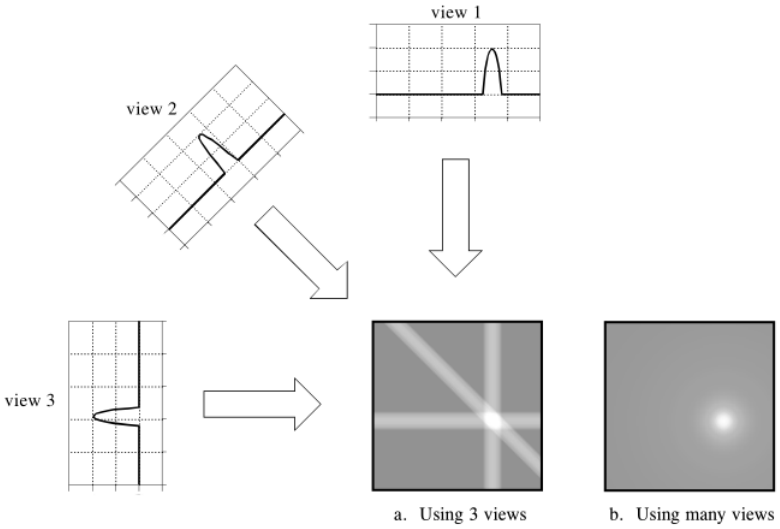

Figure 2.4: Backprojection reconstructs an image by taking each view and smearing it along the path it was originally acquired. The resulting image is a blurry version of the correct image.

Filtered backprojection (FBP) is a technique to correct the blurring encountered in simple backprojection. As illustrated in Fig.[2.5], each view is filtered before the backprojection to counteract the blurring PSF. That is, each of the one-dimensional views is convolved with a one-dimensional filter to create a set of filtered views. These filtered views are then backprojected to provide the reconstructed image, a close approximation to the "correct" image. In fact, the image produced by filtered backprojection is identical to the correct image when there are an infinite number of views and an infinite number of points per view.

Notice how the profiles have been changed by the filter. The image in this example is a uniform white circle surrounded by a black background. Each of the acquired views has a flat background with a rounded region representing the white circle. Filtering changes the views in two significant ways. First, the top of the pulse is made flat, resulting in the final backprojection creating a uniform signal level within the circle. Second, negative spikes have been introduced at the sides of the pulse. When backprojected, these negative regions counteract the blur.

FBP algorithm and its modified versions for 2D and 3D projection reconstruction, such as FDK (Feldkamp-Davis-Krees) algorithm have been used in almost all the fields of straight ray tomography. The projection can be classified into two types: parallel and fan beam projection.

Since FBP for fan beam tomography is usually obtained by modifying that for parallel beam tomography. The derivation of FBP algorithm for par-

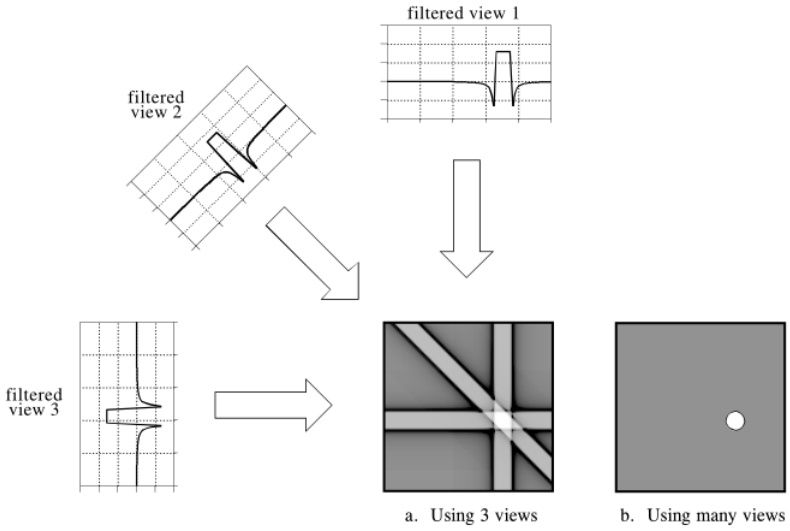

Figure 2.5: Filtered backprojection reconstructs an image by filtering each view before backprojection. This removes the blurring seen in simple backprojection, and results in a mathematically exact reconstruction of the image.

allel beam tomography is rather simple. The Fourier slice theorem links 1D Fourier transform (FT) of the projection data collected at angle θ,S_θ(w)[12], with 2D FT at the frequency samples. We consider the Radon transform, namely

$$\begin{aligned} S_\theta(\omega) &= \int_{-\infty}^{\infty} R(r,\theta)\exp(-i2\pi\omega r)dr \\ &= \int_{-\infty}^{\infty}\int_{-\infty}^{\infty} f(x,y)\exp[-i2\pi\omega(x\cos\theta + y\sin\theta)]dxdy \\ &= F(\omega\cos\theta, \omega\sin\theta) \end{aligned} \tag{2.3}$$

Then, the unknown $f(x,y)$ can be reconstructed by the Inverse Fourier Transform (IFT) or the dual Radon transform as following

$$\begin{aligned} \hat{f}(x,y) &= \int_0^{\pi}\int_{-\infty}^{\infty} F(\omega\cos\theta, \omega\sin\theta)|\omega|\exp[i2\pi\omega(x\cos\theta + y\sin\theta)]d\omega d\theta \\ &= \int_0^{\pi}\int_{-\infty}^{\infty} S_\theta(\omega)|\omega|\exp(i2\pi\omega r)d\omega d\theta \end{aligned} \tag{2.4}$$

where $\hat{f}(x,y)$ denotes the reconstructed image; $r = x\cos\theta + y\sin\theta$; $|\omega|$ is known as "ramp filter "in the frequency domain. $\hat{f}(x,y)$ will be identical with $f(x,y)$ almost everywhere according to the properties of FT and IFT. In

practice, the projection data and reconstructed images have to be discretized to record, calculate and display.

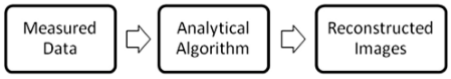

Figure 2.6: The basic workflow of an FBP.

Iterative Techniques

Iterative reconstruction (IR) and algorithms such as projection or image based noise reduction are currently being introduced to help users to reduce absorbed dose in CT.

In iterative reconstruction, an initial estimate of the object being imaged is generated from the acquired projection data. This is typically done using FBP, which are very fast. IR do not reduce absorbed dose in CT scanning. Rather, by improving the image quality through noise reduction, the technical factors that affect absorbed dose can be adjusted to realize excellent image quality at reduced noise levels.

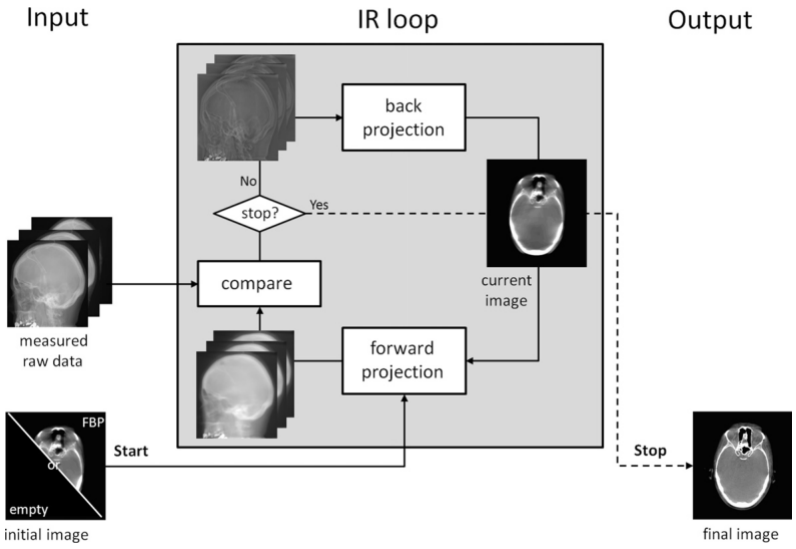

Figure 2.7: Schematic view of the iterative reconstruction process[13]. The volume estimated is initiated either with an empty image or, if available, an FBP reconstruction. If a stop criterion is matched,the loop is terminated and the current volumetric image becomes the final volumetric image.

This section will give an overview of available iterative reconstruction methods and the range of physical models which can be applied in these algorithms. We distinguish between:

- *Pure iterative methods without any modeling.*
- *Statistical methods with modeling of the photon counting statistics.*
- *Model-based methods which go beyond statistical modeling.*

Abbreviation	Meaning
ART	Algebraic reconstruction technique
SART	Simultaneous ART
SIRT	Simultaneous iterative reconstruction technique
OS-SIRT	Ordered subset SIRT
MART	Multiplicative algebraic reconstruction technique
ML-EM	Maximum likelihood expectation-maximization
OS-EM	Ordered subset expectation-maximization
OSC	Ordered subset convex algorithm
ICD	Iterative coordinate descent
OS-ICD	Ordered subset ICD
MBIR	Model-based iterative reconstruction

Figure 2.8: Selection of the most prominent iterative reconstruction algorithms.

Pure iterative methods without any modeling

All iterative reconstruction consist of three major steps Fig.[2.7]; first, a forward projection of the current volumetric image is necessary to create artificial raw data. Then artificial and measured raw data are compared and an update image is computed which subsequently is backprojected to the current volumetric image.

The simplest form of iterative reconstruction is the algebraic reconstruction technique, namely ART. This is based on Kaczmarz method for solving linear system of equations $Ax = b$, where in terms of image reconstruction x are the voxels of the volume to be reconstructed, A is system matrix used for producing the raw data and b are the pixels of the measured raw data. The entries of the matrix A correspond to rays from the x-ray source through the volume to the detector pixels.
To start the ART algorithm, all the pixels in the image array are set to some arbitrary value. An iterative procedure is then used to gradually change the image array to correspond to the profiles. An iteration cycle consists of looping through each of the measured data points. For each measured value, the following question is asked: how can the pixel values in the array be changed to make them consistent with this particular measurement? In other words,

the measured sample is compared with the sum of the image pixels along the ray pointing to the sample. If the ray sum is lower than the measured sample, all the pixels along the ray are increased in value. Likewise, if the ray sum is higher than the measured sample, all of the pixel values along the ray are decreased. After the first complete iteration cycle, there will still be an error between the ray sums and the measured values. This is because the changes made for any one measurement disrupts all the previous corrections made. The idea is that the errors become smaller with repeated iterations until the image converges to the proper solution[14].

Statistical methods with modeling of the photon counting statistics

The key idea of statistical methods is to incorporate counting statistics of the detected photons into the reconstruction process. In transmission CT the number of photons leaving the x-ray tube as well as the measured photons at the detector, which passed through the patient or object, are assumed to be Poisson distributed[15]. Statistical reconstruction methods can work in three different domains:

1. **Methods in the raw domain (sinogram domain)**: the methods working in the raw data apply an adaptive or iterative 2D edge-preserving denoising algorithm directly on the projection raw data.

2. **Methods in the image domain**: Algorithm in the volumetric image domain are denoising the volume after the reconstruction and they are aiming for noise reduction while preserving spatial resolution. All filters which are applied on the reconstructed volumetric data without using any information on the acquisition process are not considered statistical recostruction methods, but post-processing filters.

3. **Full statistical methods**: These algorithms can be roughly divided into two groups: methods based on correlated to the maximum likelihood principle and those based or correlated to the least square principle. By maximizing the likelihood, the algorithm tries to find the set of parameters that makes the measurements the most probable. In maximization methods the natural algorithm of the likelihood is often more convenient, which fortunately has its maximum values at the same points as the function itself.

Next figure shows an example of a statistical IR algorithm, sometimes known as a hybrid IR algorithm because of its ability to blend with FBP, this commercial manufacturer is called adaptive statistical iterative reconstruction (ASIR).

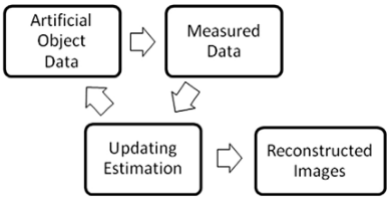

Figure 2.9: The basic workflow of an ASIR algorithm.

Model-based methods which go beyond statistical modeling

The term model-based classifies all methods which go beyond modeling statistics of the detected photons as Poisson distributed. These methods try to model the acquisition process as accurately as possible. The acquisition is a physical process in which photons with a spectrum of energies are emitted by the focus area on the anode of an x-ray tube; they travel through the object and are either registered within the area of a detector pixel, scattered outside of the detector or are absorbed by the object[16].

Model based iterative algorithm (MBIR) is an advanced CT algorithms that incorporates modeling of several key parameters that were omitted in earlier algorithms to reduce computational requirement and speed up scans. More recently, model-based iterative reconstruction (MBIR), also known as pure IR algorithm, has been shown to significantly improve image quality while reducing noise and artifacts in multislice CT scans during initial tests.

In MBIR, images are reconstructed by minimizing the objective function incorporated with an accurate system model, a statistical noise model, and a prior model. The system model deals with the nonlinear, polychromatic nature of x-ray tubes by modeling the photons in the measured data set. The statistical noise model takes into consideration the size of an x-ray tube focal spot and the three-dimensional shape of detectors. The prior model is a regularization algorithm that corrects unrealistic situations during reconstruction to speed up the process[17].

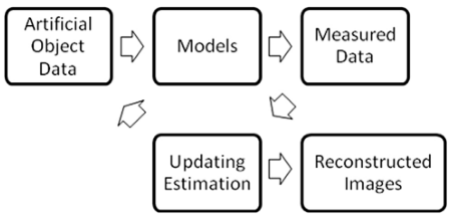

Figure 2.10: The basic workflow of an MBIR algorithm.

2.2 State of the art

With increasing recognition of the importance of radiation protection, dose reduction has become an important issue in CT system development. Modern CT systems are equipped with several dose reduction techniques. These techniques range from hardware, such as a sliding collimator to eliminate unnecessary radiation exposure due to overranging, to algorithms such as improved filtered back projection (FBP) and iterative reconstruction, as previously seen.

Newer iterative reconstruction techniques are promising for effectively reducing dose. Studies have shown that with iterative techniques, image noise (measured as the SD of attenuation) decreases and contrast-to-noise ratio increases compared with the values with FBP at similar dose levels. Clinical observer studies have confirmed that with iterative techniques, substantial reduction in radiation dose can be achieved without loss of image quality.

A limitation of iterative reconstruction is that the images have a different appearance resulting from a change in shape of noise power spectrum (NPS). This change in NPS shape hampers objective comparisons of image quality by assessment of noise expressed as Standard Deviation of attenuation, which is the general method for measuring noise and its relation to radiation dose.

Each CT manufacturer has developed its own iterative reconstruction technique. Consequently, results may not be generalized for all iterative reconstruction techniques. Studies have been performed with ASiR (GE Healthcare), Veo (GE Healthcare), IRIS (Siemens Healthcare), Safire (Siemens Healthcare), iDose (Philips Healthcare), and AIDR (Toshiba Medical Systems).

Manufacturer	Statistical IR	Model-based IR
General Electric	ASiR	Veo
Philips	iDose	IMR
Siemens	IRIS	SAFIRE
Toshiba	AIDR 3D (integrated)	AIDR 3D (integrated)

IR, iterative reconstruction.

Figure 2.11: Statistical and Model-based Iterative Reconstruction Algorithms Developed by Major Computed Tomography Manufacturers[16].

Objective measurements in most of the previous studies have been limited to measurements of noise levels as Standard Deviation. In only a few studies did investigators support their results with NPS measurements, and some

investigators added an objective evaluation of spatial resolution. In general, study results show a significant decrease in noise and potential dose reduction.

Now we see the main differences between these manufacturer, finally explains in detail the algorithm used in this thesis ($iDose^4$).

2.2.1 GE Healthcare

ASiR

ASiR, the industry's first iterative reconstruction technology, may improve low contrast detectability (LCD) allow for reduced noise, and reduced mA all without degrading anatomical integrity. ASiR overcomes the limitations of the conventional CT reconstruction approach (FBP) arriving at an optimal image using an advanced iterative computation. This computation may dramatically reduce the amount of dose needed to acquire a high-performance image. In early studies, the use of ASiR has been found to enable dose reductions of one-third to one-half while improving image quality.

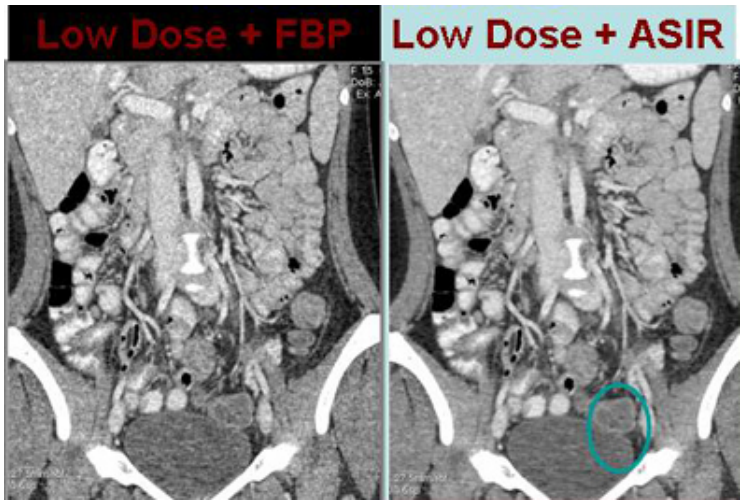

Figure 2.12: In a 15-year-old patient presenting to the emergency department to rule out appendicitis, low-dose scan with FBP reconstruction was noisier than follow-up imaging using the same dose with ASiR reconstruction[18].

In clinical practice, the use of ASiR may reduce CT patient dose depending on the clinical task, patient size, anatomical location and clinical practice. A consultation with a radiologist and a physicist should be made to determine the appropriate dose to obtain diagnostic image quality for the particular clinical task.

VEO

Enabling imaging under 1 mSv with profound clarity; the world's first model-based CT iterative reconstruction product, Veo combines sophisticated algorithms with advanced computing power. This breakthrough is changing the way physicians use CT imaging, delivering a unity of high-performance images and low dose that was previously unthinkable. VEO establishes new rules in the relationship between image quality and dose reduction, opening up new possibilities for challenging cases and sensitive patients. VEO can give the clinicians the diagnostic information they need at previously unthinkable ultra low dose levels.

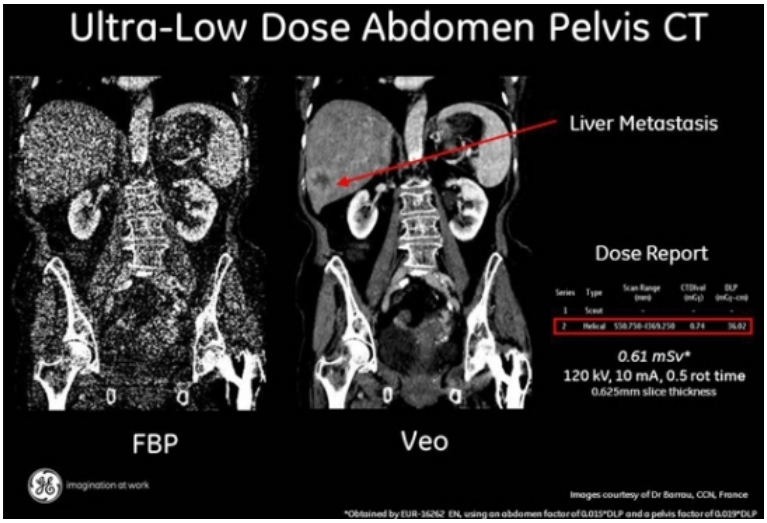

Figure 2.13: Liver metastasis visualized with VEO. The right image is less noisy than other[19].

Veo is the worlds first model-based iterative reconstruction product. Radiologists and clinicians can operate under a new set of rules. Lower noise and higher resolution can be achieved within a single image. At the same time, significant dose reduction capabilities are now available, opening up new possibilities for challenging cases and sensitive patients.

The benefits of this capability are significant, especially for the most radio-sensitive patients including pediatric cases and young women, or those requiring regular follow-up and monitoring as it dramatically reduces cumulative dose in patients who require regular follow-up exams. Veo is able to improve image resolution by up to 50% and reduce noise while using as little as one eighth of the normal dose as compared to a standard CT image. In traditional CT reconstruction approaches, higher spatial resolution is typically accompanied by higher image noise. VEO's CT reconstruction platform

challenges this trade-off by improving resolution while reducing noise.

2.2.2 Siemens Healthcare

IRIS

Instead of reducing the amount and complexity of corrective models to gain reconstruction speed Siemens has developed a new method for iterative reconstruction which maintains the image correction quality of theoretical iterative reconstruction. To accelerate the convergence of the reconstruction and to avoid long reconstruction times the new IRIS applies the raw data reconstruction only once.

During this newly developed initial raw data reconstruction a so called master image is generated that contains the full amount of raw data information yet at the expense of significant image noise. The following iterative corrections known from theoretical iterative reconstruction are consecutively performed in the image space. They clean up the image and remove the image noise without degrading image sharpness. Therefore, a time consuming repeated projection and corresponding back projection can be avoided. In addition, the noise texture of the images is comparable to standard well established convolution kernels.

Figure 2.14: Comparison between standard protocol (FBP) and Iterative reconstruction in image space [see www.healthcare.siemens.com].

This technique results in artifact and noise reduction, increased image sharpness, and dose savings of up to 60% for a wide range of clinical appli-

cations. IRIS allows to enhance spatial resolution and to reduce image noise by introducing multiple iteration steps in the reconstruction process.

SAFIRE

SAFIRE (Sinogram Affirmed Iterative Reconstruction) is considered innovative compared with IRIS, because it works not only in image space but also in raw data domain. First of all, an anisotropic noise model is applied to images reconstructed with FBP in order to reduce the variance of the signal. After each iteration, data are reprojected in sinogram space to validate the images with measurement data, and the detected deviations are corrected, yielding an updated image.

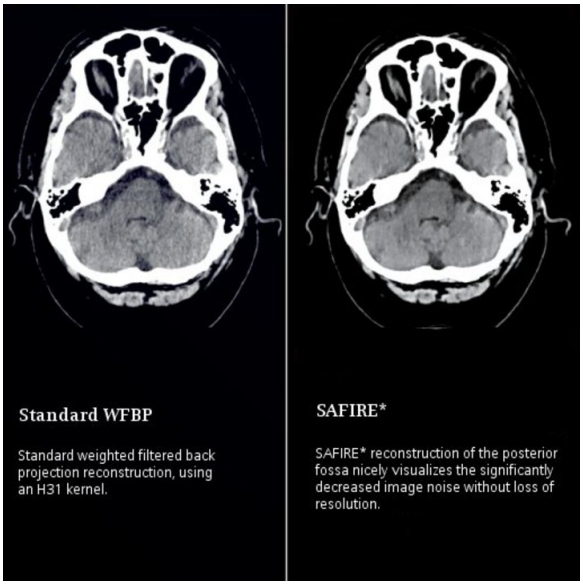

Figure 2.15: Comparison between FBP and Sinogram Reconstruction. Image noise decrease without loss of resolution in the right image [see www.healthcare.siemens.com].

SAFIRE is an advanced IR technique that utilizes both projection space data and image space data, with the number of iterations in each space dependent on the needs of a specific scan. In contrast to other pure raw data based IR algorithms, SAFIRE is available right on the scanner and can reconstruct up to 20 images per second. Therefore, SAFIRE can easily be used in routine clinical workflow, with well established reconstruction kernels, providing up to 60% reduction in dose.

2.2.3 Toshiba Medical System

AIDR 3D

AIDR (Adaptive Iterative Dose Reduction) is Toshiba's latest evolution of iterative reconstruction technology; it has been fully integrated and automated into the imaging chain to improve dose reduction and image quality. It is designed to reduce dose by reducing the magnitude of image noise while preserving image detail, allowing for lower dose acquisitions.

The reconstruction process incorporates raw data and image space noise optimization. During AIDR 3D reconstruction, a scanner model and a statistical noise model are taken into account to minimize the effects of photon starvation and electronic and statistical noise in projection space while an image-based anatomical model minimizes quantum noise magnitude.

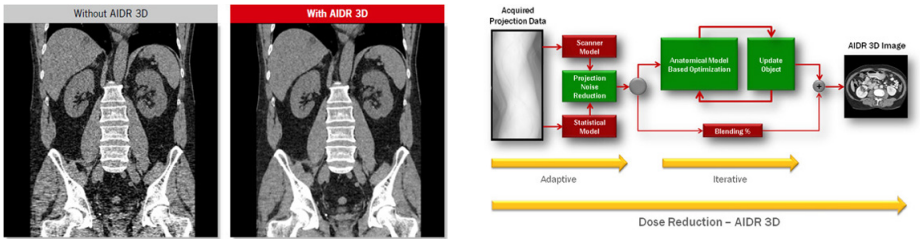

Figure 2.16: In the left image we see noise reduction with AIDR3D. In the right image is shown the workflow for dose reduction AIDR 3D [see toshibamedicalsystems.com].

This advanced iterative reconstruction algorithm works in two parts. The first part adaptively removes photon noise in the 3D raw data domain. This is followed by the second part, model-based iterative noise reduction in the reconstruction process. AIDR 3D reconstruction has therefore been systematically optimized to minimize the impact on patient throughput. As a result, advanced iterative reconstruction with AIDR 3D adds mere seconds to the total reconstruction time.

With each interation, AIDR 3D fine-tunes these results for the particular exam, balancing the relationship between noise magnitude reduction and spatial resolution preservation. The original FBP image is used as an input for each iteration and is adaptively blended with the processed data to create the final image, helping to ensure the noise texture is well maintained for the viewer.

2.2.4 Philips Healthcare

IMR

The low required dose is the result of Philips' proprietary Iterative model reconstruction (IMR) system which has set a new direction in CT image quality with industry leading low-contrast resolution and virtually noise-free images. Long associated with MR, this improvement in low-contrast resolution is a made possible through IMR, the first technique to be built on a knowledge-based model. Enabled by hardware innovation, its reconstruction speed allows IMR to be used in even the most demanding applications. The new capabilities also mark the first time a knowledge-based solution takes benefits previously realised only in routine body imaging to advanced neuro and cardiovascular applications.

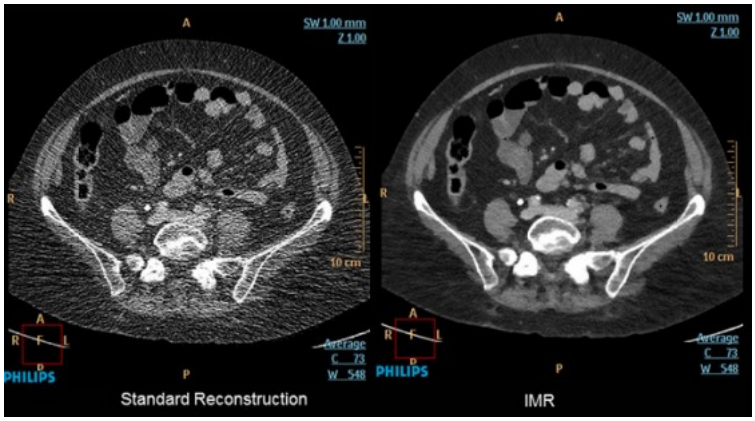

Figure 2.17: Image enhancement of an abdomen using IMR [see www.healthcare.philips.com].

With Philips IMR, low dose and enhanced image quality can be delivered together in CT imaging. With IMR, clinicians acquiring CT images can simultaneously lower radiation dose by 60-80%, with 43-80% improvement in low contrast detectability and 70-83% less image noise, relative to standard reconstruction techniques (FBP).

iDOSE^4

iDose^4 is a 4th generation reconstruction technique that provides significant improvements in image quality and radiation dose reduction. The [Fig. 2.18] summarizes the advantages of this generation reconstruction techniques in terms of artifact prevention and the efficiency of quantum mottle noise reduction across all frequencies.

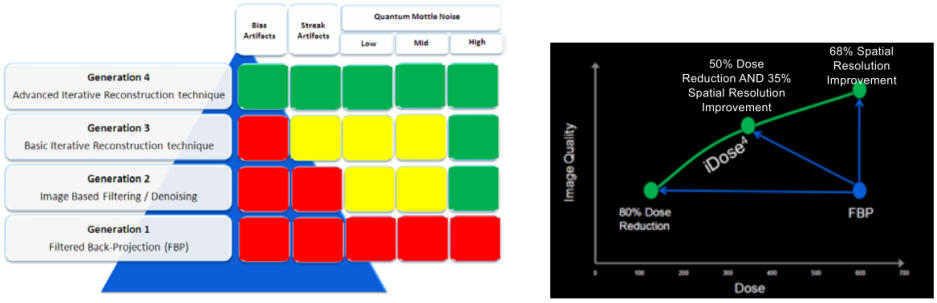

Figure 2.18: Summary of noise reduction and artifact prevention capabilities provided by each reconstruction generation (left). Adapting dose reduction and spatial resolution based on the clinical indication (right) [see www.healthcare.philips.com].

Optimizing the implementation of iDose^4 on the Philips CT scanner platforms has enabled the additional clinical benefit of being able to adapt the spatial resolution and dose reduction benefits to the specific clinical indication. For pediatric imaging where radiation dose reduction is paramount, iDose^4 enables significantly lower radiation dose while maintaining diagnostic image quality. In other cases, where image quality (e.g., spatial resolution) is of higher priority than the dose reduction, such as in the assessment of coronary stent patency, iDose^4 enables significantly improved image quality.

In FBP, the reconstruction filter amplifies any noise present in the projections proportional to the spatial resolution characteristics of the filter. High spatial resolution (sharp filter) reconstructions amplify image noise levels to clinically unacceptable levels and make them suboptimal for low contrast assessments. Hence, the need to perform two reconstructions (i.e., soft filter and sharp filter).

With iDose^4 , the noise in sharp reconstructions can be maintained at a sufficiently low level to permit soft tissue and detailed, high contrast assessment from a single reconstruction that provides improved image quality over either individual FBP reconstruction.

This algorithm provides an innovative solution in which iterative processing is performed in both the projection and image domains. The reconstruction algorithm starts first with projection data where it identifies and corrects the noisiest CT measurements, those with very poor signal to noise ratio, or very low photon counts. Each projection is examined for points that have likely resulted from very noisy measurements using a model that includes the true photons statistics. Through an iterative diffusion process, the noisy data is penalized and edges are preserved.

This process ensures that the gradients of underlying structures are retained, thus preserving spatial resolution while allowing a significant noise

reduction. Since the corrections are performed on the acquisition data; this method successfully prevents bias error. The noise that remains after this stage of the algorithm is propagated to the image space; however, the propagated noise is now highly localized and can be effectively removed to support the desired level of dose reduction.

2.2.5 Summary

After summarizing these iterative reconstruction algorithms, we can say:

- All IR algorithms improved general image quality compared with FBP.
- The statistical IR algorithms improves image quality proportional independent of radiation dose.
- The model-based IR algorithms improves image quality progressive with reducing radiation dose.
- ASiR, VEO, IMR, iDOSE^4 maintained or improved spatial resolution at the same time reducing the noise.
- All IR algorithms affected the NPS, especially the model-based.

The application of the iterative process is weighed on scales that change as a function of the vendors (GE, Siemens, Toshiba, Philips). General Electric uses percentages (10%, 50%, 90%), Siemens uses nominal values (strength 1, strength 3, strength 5), Toshiba uses standard names (mild, standard, strong).

In our case (iDose^4) the scale is numerical and varies from level 1 to level 7, in relation to the anatomical district acquired.

Chapter 3

Image Quality Assessment

3.1 Noise Power Spectrum Analysis

In this section we describe and study a powerful metric for analyzing CT performance, called Noise Power Spectrum (NPS). In diagnostic CT imaging, noise is mainly caused by photon detection statistics and cannot be avoided due to the desire to limit radiation dose. The standard deviation (SD) of noise, provides no information about noise spatial characteristics and thus has only a gross predictive value for object detectability.

While the image SD is relatively easy to calculate, it may not fully reflect the impact that the noise will have on a diagnostic task. In this study, the NPS will be used to described the noise including correlation introduced by filtering, remembering that NPS characterizes both the magnitude and spatial frequency distribution of image noise; the magnitude reflects the degree of randomness at each spatial frequency.

The shape of the NPS reveals where the noise power is concentrated in frequency space:

1. *Low-frequency noise power concentration means noise will be significantly mottled in appearance.*

2. *High-frequency noise power will result in finer grain noise.*

Furthermore, the sum of noise power over all non zero frequencies in the NPS yield the noise variance. By taking into account both the variance and spatial characteristics of the image noise, the NPS is a more thorough noise descriptor than pixel standard deviation.

The NPS calculated in this work is divided by the square of the mean value of the pixels used for analysis. This ratio is referred to as the normalized

noise power spectrum (NNPS)[20]:

$$NNPS(u,v) = \frac{NPS(u,v)}{(large\ area\ signal)^2} \qquad [mm^2] \tag{3.1}$$

The large are signal is basically a measure of the gain of the system. It is measured in the same units as the data used to determine NPS.

The noise power spectrum is related to the frequency decomposition of the image noise. First, an image containing nothing but the noise to be analyzed is decomposed into its two-dimensional frequency components. These components, called the Fourier amplitudes, are then squared to obtain the power contribution at each frequency.

This result is averaged with the results obtained from other similar images to arrive finally at the average noise power for each frequency, or, in other words, the noise power spectrum. It is therefore proportional to the average square value of the frequency amplitudes of the noise. The square of the amplitude is used instead of the amplitude itself, since the average value of the amplitude is zero while the average value of the squared amplitude is not. Often the response of the system is assumed to be circularly symmetric[21] (as we will see later).

3.1.1 Materials and Methods

In this work we acquired some phantoms normally used to investigate image quality in CT. A simple approach, ensuring spectral response similar to the clinical response, is the use of a homogeneous phantom simulating the spectral response of the real tissue. The acquisitions were made on a Philips phantom with different scan, recostruction data, iterative reconstruction levels and different convolution kernel (or filters).

The main phantom used for testing, is composed of two part: head and body, which are mounted on a support before each measurement.

Figure 3.1: Philips Phantom used for acquisition. Body phantom (LEFT SIDE) and head phantom (RIGHT SIDE).

The measurements were performed using iCT128 MSCT (Philips Healthcare) installed at Radiology Department of Sant'Orsola-Malpighi Hospital, in Bologna. The images were acquired in axial and spiral scan mode, with reconstruction matrices 512×512 (both head and body phantom).

Body Phantom

The first phantom analyzed was the body unit, which is made from a single polymethylmethacrylate (PMMA) container of 320 mm in diameter, filled with water and with a teflon (PTFE) pin inside.

This phantom is used for calibration and quality assurance in body modality. It is mounted on the bed of the system.

First of all, several images are acquired for each set analyzed. To study the noise power spectrum, we used the method suggested in [22][23][24], therefore we selected the first seven slice reconstructions. The reason for this is because if there are large exposure variations over the measurements area, computing the NNPS separately for each ROI and then averaging will tend to cancel some (but not all) the variations in noise power, resulting from regional variations in x-ray exposure. Namely decrease the statistics fluctuations of noise texture, in such a way that the shape of NNPS will have less peaks.

The next table shows the acquisition and reconstruction parameters for the Noise Power Spectrum study.

Voltage	120 kVp
Exposure	200 mAs
Beam Collimation	64×0.625
Convolution Kernel	A, B, C, D, D(H)
Slice Thickness	2.5 mm
Pixel Sixe	0.6835×0.6835 mm
FOV	350×350 mm
Rotation Time	0.75 s
Matrix Size	512 × 512

Table 3.1: List of parameters utilized.

Kernel A	Very smooth	Large patients, No effects on HU values
Kernel B	Smooth	Routine abdomen and pelvis
Kernel C	Sharp	Routine abdomen and pelvis
Kernel D	Very sharp	Edge enhancement in lung and bone
Kernel D(H)	Very sharp and high resolution	Edge enhancement

Figure 3.2: Convolution kernel for body phantom.

The images were studied by a set of plugin applications for ImageJ software, called QA-distribution. The Noise Power Spectrum was calculated using this software in the following way.

The plugin can handle both linear and square root compressed images without signal offset. The NNPS is calculated from a uniformly exposed image. The image is divided in image fragments with $2^N \times 2^N$, in this case 64×64 because this ROI provide a bin frequency around $0.03\, lp/mm$, a good compromise to get a proper definition without excessive noise[22][23][24].

The noise analysis is performed on these individual subregions and the final NNPS is calculated as the average of all individual noise spectra, obtained from each subregion. We assume that a flatfield corrected linear image is used[25].

At this time, we select the parameters for calculate NNPS.

- Select actual pixel size.
- Select NNPS fragment size.
- Choose the number of lines around the central axis not be used for the evaluation of the NNPS.
- Choose whether you want to show the 2D NNPS image on the screen.
- Select image type.

Taking account that the size for the NNPS calculation should be a power of 2, and a 2D FFT-algorithm is used, we choose a uniformly exposed area and select a ROI excluding the teflon insert. The radially averaged NNPS is calculated by radial averaging the NNPS over all pixels of the 2D NNPS[26][27].

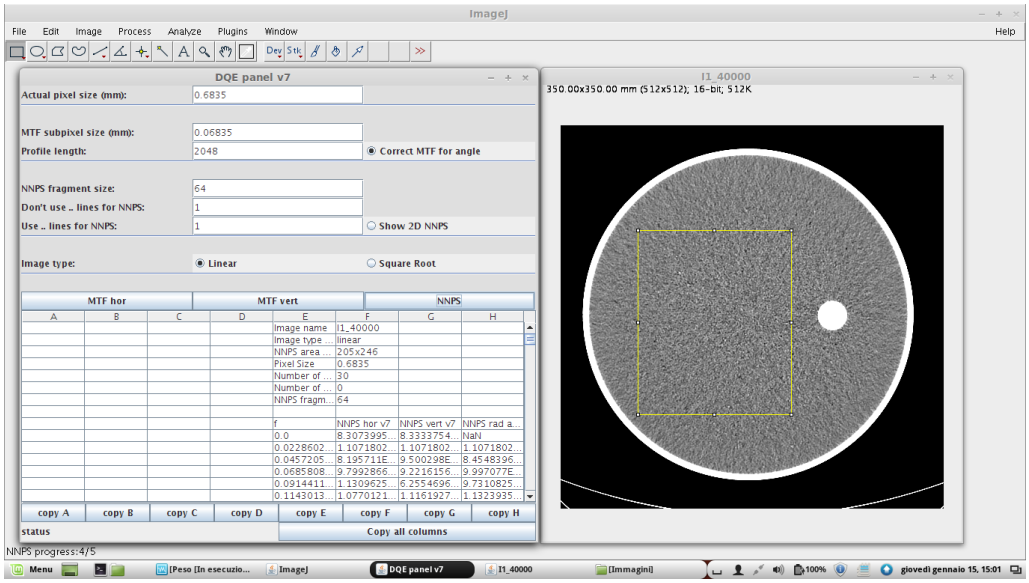

Figure 3.3: Spatial frequency (mm^{-1}) and radially NNPS values (mm^2) (LEFT). Body phantom image and ROI utilized for calculate the Normalized Noise Power Spectrum (RIGHT).

Spatial Frequency	Slice 1	Slice 2	Slice 3	Slice 4	Slice 5	Slice 6	Slice 7	Average values – Kernel A
0	0	0	0	0	0	0	0	0
0.022860278	1.31E-004	1.40E-004	1.56E-004	1.15E-004	1.17E-004	1.32E-004	1.54E-004	1.35E-004
0.045720556	1.98E-004	1.38E-004	2.32E-004	1.59E-004	2.16E-004	1.53E-004	2.14E-004	2.06E-004
0.0685808339	2.47E-004	1.85E-004	2.19E-004	2.51E-004	2.45E-004	2.20E-004	2.38E-004	2.42E-004
0.0914411119	2.97E-004	2.47E-004	2.73E-004	2.59E-004	3.32E-004	2.86E-004	2.87E-004	2.92E-004
0.1143013899	3.22E-004	2.68E-004	3.08E-004	3.24E-004	3.41E-004	3.05E-004	2.82E-004	3.02E-004
0.1371616679	3.73E-004	3.34E-004	3.55E-004	3.59E-004	3.90E-004	3.41E-004	3.50E-004	3.62E-004
0.1600219459	3.85E-004	3.90E-004	3.65E-004	3.38E-004	3.40E-004	3.86E-004	4.03E-004	3.94E-004
0.1828822238	4.37E-004	3.70E-004	4.08E-004	3.80E-004	4.07E-004	4.06E-004	3.80E-004	4.08E-004
0.2057425018	4.14E-004	4.39E-004	4.06E-004	3.96E-004	4.06E-004	3.76E-004	3.98E-004	4.06E-004
0.2286027798	3.86E-004	3.58E-004	3.97E-004	3.80E-004	4.03E-004	4.04E-004	4.10E-004	3.98E-004
0.2514630578	4.13E-004	3.57E-004	4.23E-004	3.52E-004	4.12E-004	3.88E-004	4.16E-004	4.15E-004
0.2743233358	3.66E-004	3.52E-004	3.69E-004	3.61E-004	3.61E-004	4.00E-004	3.53E-004	3.60E-004
0.2971836138	3.51E-004	3.09E-004	3.14E-004	3.43E-004	3.34E-004	3.41E-004	3.27E-004	3.39E-004
0.3200438917	3.17E-004	2.92E-004	3.02E-004	2.85E-004	3.10E-004	2.96E-004	3.10E-004	3.13E-004
0.3429041697	2.95E-004	2.70E-004	2.83E-004	2.74E-004	2.82E-004	2.57E-004	2.98E-004	2.97E-004
0.3657644477	2.50E-004	2.47E-004	2.28E-004	2.23E-004	2.50E-004	2.24E-004	2.38E-004	2.44E-004
0.3886247257	2.22E-004	2.09E-004	1.93E-004	2.01E-004	2.05E-004	1.97E-004	2.08E-004	2.15E-004
0.4114850037	1.73E-004	1.73E-004	1.70E-004	1.57E-004	1.63E-004	1.50E-004	1.75E-004	1.74E-004
0.4343452816	1.40E-004	1.38E-004	1.32E-004	1.34E-004	1.42E-004	1.27E-004	1.32E-004	1.36E-004
0.4572055596	1.07E-004	1.04E-004	1.09E-004	1.03E-004	1.07E-004	1.03E-004	1.07E-004	1.07E-004
0.4800658376	8.67E-005	8.11E-005	7.95E-005	8.07E-005	8.54E-005	7.78E-005	8.10E-005	8.39E-005
0.5029261156	5.92E-005	6.02E-005	5.94E-005	6.23E-005	6.33E-005	5.53E-005	5.86E-005	5.89E-005
0.5257863936	4.29E-005	3.91E-005	4.35E-005	4.47E-005	4.15E-005	4.21E-005	4.24E-005	4.27E-005
0.5486466715	2.96E-005	2.86E-005	3.03E-005	3.03E-005	2.94E-005	2.93E-005	2.89E-005	2.92E-005
0.5715069495	1.99E-005	1.86E-005	1.90E-005	1.89E-005	1.89E-005	1.95E-005	2.01E-005	2.00E-005
0.5943672275	1.32E-005	1.16E-005	1.17E-005	1.16E-005	1.24E-005	1.12E-005	1.16E-005	1.24E-005
0.6172275055	8.49E-006	7.36E-006	7.51E-006	8.01E-006	7.64E-006	7.57E-006	7.38E-006	7.94E-006
0.6400877835	5.43E-006	4.82E-006	5.21E-006	5.31E-006	5.06E-006	5.12E-006	4.91E-006	5.17E-006
0.6629480614	3.64E-006	3.22E-006	3.52E-006	3.67E-006	3.38E-006	3.50E-006	3.34E-006	3.49E-006
0.6858083394	2.82E-006	2.38E-006	2.67E-006	2.63E-006	2.60E-006	2.68E-006	2.49E-006	2.66E-006
0.7086686174	2.27E-006	1.93E-006	2.24E-006	2.18E-006	2.13E-006	2.18E-006	2.02E-006	2.15E-006

Figure 3.4: Values of NNPS calculate for all seven slice with FBP algorithm and Convolution kernel A.

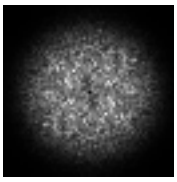

Figure 3.5: 2D image of the NNPS, note the circular symmetry.

Since the 2D Fourier spectrum is a circular symmetry we select column H in the Fig.[3.2], this process was repeated for each slices of acquisition and NNPS was calculated for all seven slices Fig.[3.4]. Finally this values are averaged and utilized for the final NNPS[28][29].

The reconstruction kernel changes in relation to the characteristics of spatial resolution and contrast of the images that they determine. These feature of image quality are in opposition to each other. Then, they can be classified in two categories:

1. *Smoothing kernel, improve contrast resolution, low frequency*: to highlight elements that have little contrast to the background (e.g. abdomen, skull). It can be advantageous to employ these kernels in obese patients, where the signal-to-noise ratio can be diminished secondary to attenuation from adipose tissue.

2. *Edge kernel, improve spatial resolution, high frequency*: edge enhancement of anatomic structure (e.g. lung).

First of all we plot each convolution filter with different iDose levels to see how the curves change the shape of NNPS[30][31]. Observing this plot, NNPS measured at a fixed radius in the uniform region showed a dependency on the reconstruction method. For iterative reconstruction we found that different levels of iDose reduce the noise magnitude and shifted the noise texture.

Convolution kernel A

For increasing levels of iDose, the magnitude of the NNPS curve decreases while the peak is shifted to low frequencies. For iDose6, the spatial frequency peak is reduced by $\sim 0.1\ mm^{-1}$ respect to iDose1.

Compared to convolution kernel D (or C or DH), image reconstructed with kernel A will have worse spatial resolution, but will also have less noise at lower frequencies.

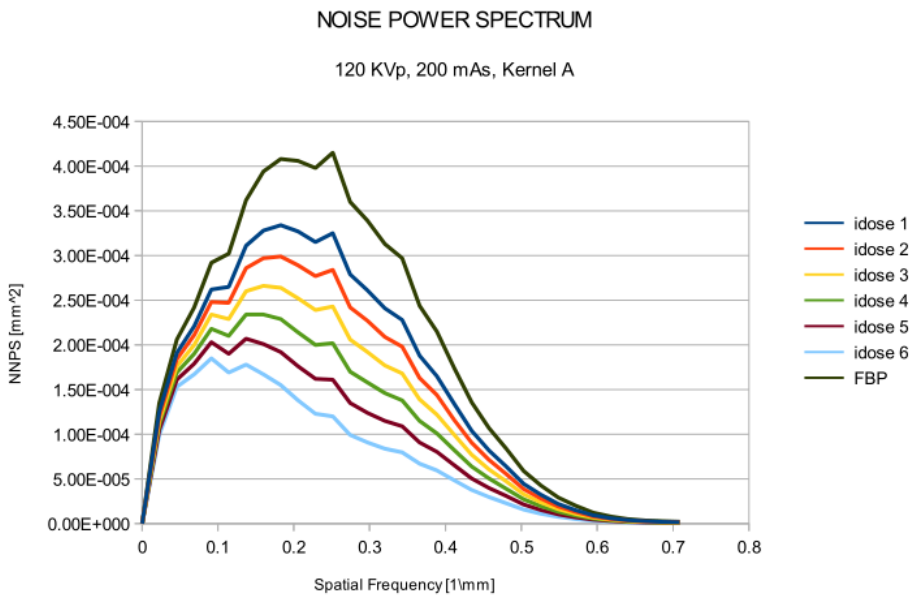

Figure 3.6: Normalized noise power spectrum for different iDose levels. An image reconstructed using this filter, producing noise texture with low spatial frequency noise. See Appendix A for phantom's image.

Convolution kernel B

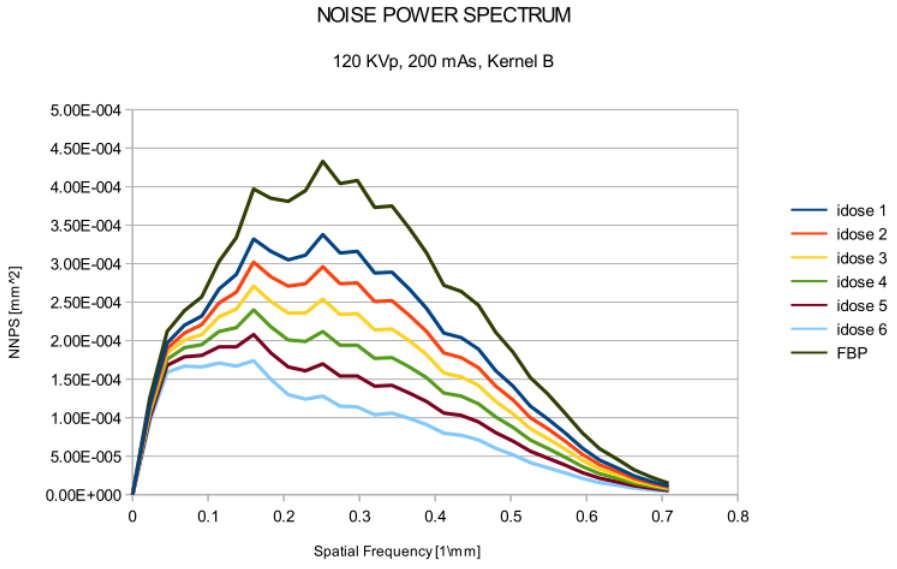

Figure 3.7: Normalized noise power spectrum for different iDose levels. First idose level will have two peaks while iDose6 will have one peak shifted at lower frequencies. See Appendix A for phantom's image.

For this kernel we observe that the first iDose level has two peaks at ~ 0.15

and $\sim 0.25\ mm^{-1}$. The positive slope region is caused by the ramp filtering, and the subsequent fall-off at higher frequencies is due to the mathematical reconstruction kernel that is used.

In this case the fall-off for iDose1 is past $0.3\ mm^{-1}$ and for iDose6 is beyond the first peak at $0.15\ mm^{-1}$. Note the plateau between $0.05\ mm^{-1}$ and $0.15\ mm^{-1}$.

Convolution kernel C

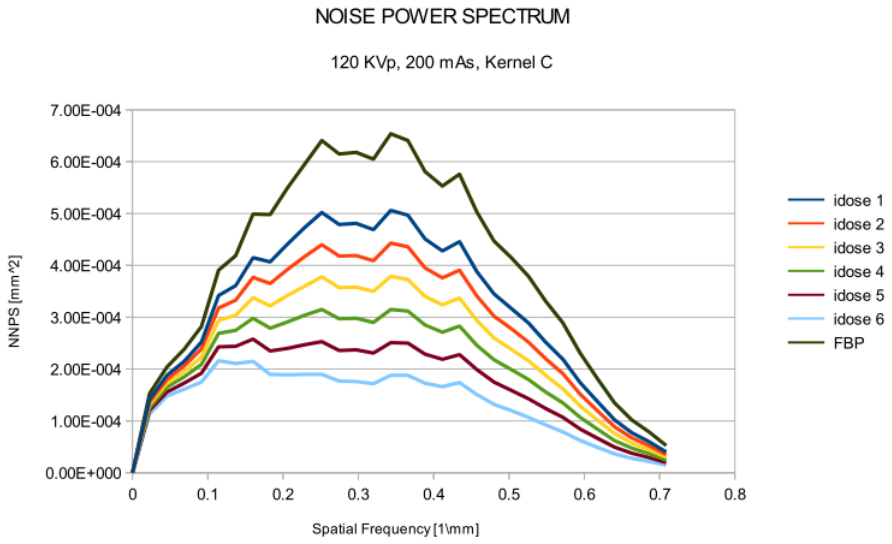

Figure 3.8: Normalized noise power spectrum for different iterative reconstruction levels. For higher levels the peaks from $0.25\ mm^{-1}$ to $0.35\ mm^{-1}$ disappear. See Appendix A for phantom's image.

By studying this filter, we note that the negative slope at high spatial frequencies fall more in subsequent zone (beyond $0.7\ mm^{-1}$) than kernel A ($\sim 0.6\ mm^{-1}$) and B ($\sim 0.7\ mm^{-1}$).

This convolution kernel shows two peculiarities.

- First, iDose1 has more noise fluctuations than iDose6.
- Second, last reconstruction level has two peaks at $0.1\ mm^{-1}$ and $\sim 0.15\ mm^{-1}$ similarly to iDose6 of kernel A.

In this case the difference is a plateau in this range of frequencies and the fall-off is beyond $\sim 0.45\ mm^{-1}$.

The positive slope region of the NNPS is lower than kernel A, B, D, DH; the plateau has an higher NNPS, however, is shorter than filter B.

Since this kernel has a wide range in all iterative levels, it can be used to study NNPS in medium spatial frequencies, even though it is a sharp filter.

Convolution kernel D

Different kernels are used that represent different trade-offs between spatial resolution and image noise, but all clinical kernels produce some roll-off in response at high frequencies. Roll-off refers to the progressive reduction in the filter function at higher spatial frequencies, to reduce the impact of quantum noise on the image[32].

This filter works at higher frequencies than the others. The plot shows that NNPS varies more than in the previous cases and for iDose1 between 0.32 mm^{-1} to 0.5 mm^{-1} will form a wide variation of NNPS values.

This feature vanishes with higher iterative levels and for iDose7 will form a plateau and also the noise power decreases slower after $\sim 0.5\ mm^{-1}$. Unlike the previous case, the shape of noise power spectrum is shifted towards higher frequencies than filter C.

Note that for iDose1, iDose2, iDose3 and iDose4 the curves overlap at low frequencies ($\sim 0.06\ mm^{-1}$); iDose4 and iDose5 plots are separated and then again overlaps for iDose5, iDose6 and iDose7 for very low values ($< 0.02\ mm^{-1}$).

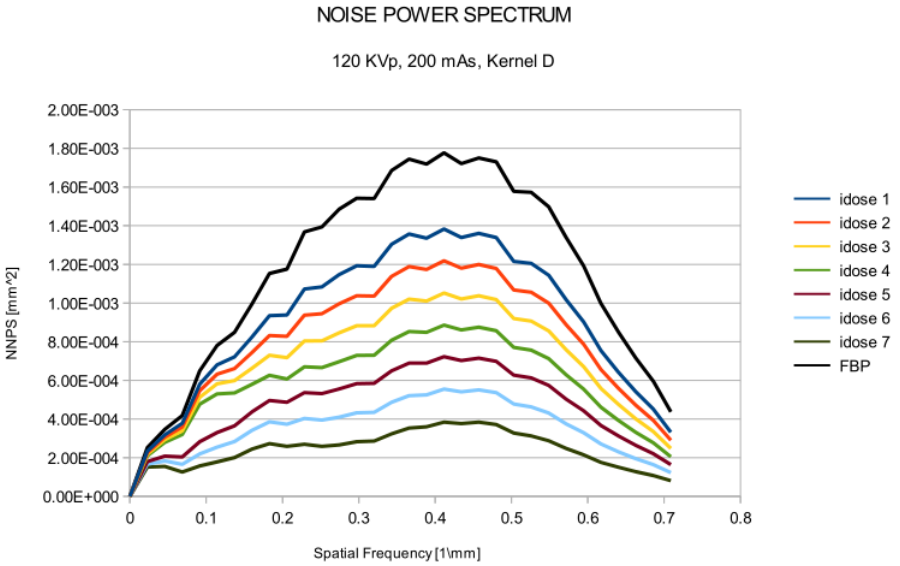

Figure 3.9: All curves shifted by high frequencies than other kernels. See Appendix A for phantom's image.

Convolution kernel DH

This filter is a sharp kernel that passes more higher-frequency noise. Compared with kernel A,B,C and D will have better spatial resolution but will also have more noise at higher frequencies.

This filter stress fine parts, in the image. Unfortunately, while kernel A, B smooths out noise, sharp filtering does the exact inverse: it enhances noise. One can skip this, if the original image is not excessively noisy; generally the noise will overpower the image. We can high-pass filter only the brightest parts of the image, where the signal-to-noise ratio is most noteworthy.

In Fig.[3.10] the shapes of noise power spectrum are very similar up to $\sim 0.45\ mm^{-1}$. Beyond this value we note that the peak at $\sim 0.5\ mm^{-1}$, with increasing iterative levels, disappears and the NNPS will have little variations respect to lower frequencies.

Secondly, for values under $\sim 0.15\ mm^{-1}$ there are no changes; furthermore for iDose7 the slope remains unchanged. For other reconstruction levels there are variations from 0.02 to $\sim 0.15\ mm^{-1}$, especially for the first four levels.

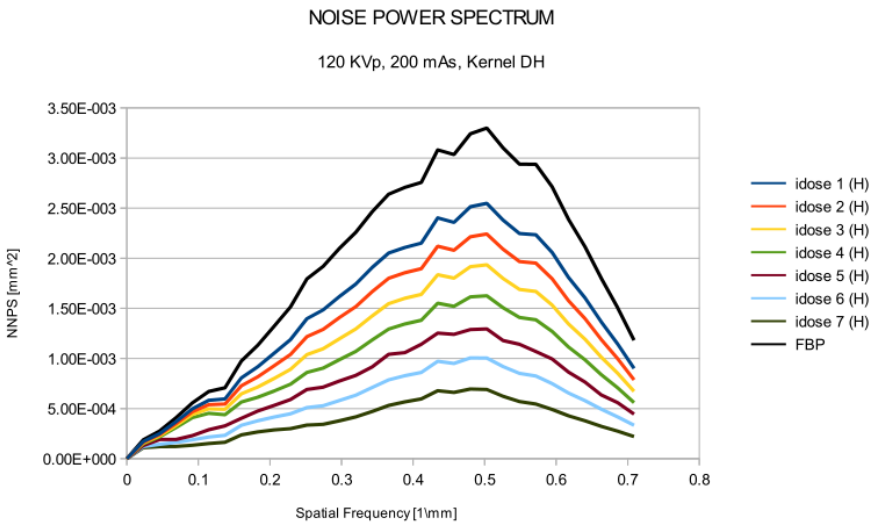

Figure 3.10: Shape of Normalized Noise Power Spectrum of FBP and reconstruction levels. The curves tends to zero more slowly than the others filter. See Appendix A for phantom's image.

Next study focuses on compared Filtered Back Projection and Iterative reconstruction algorithm using three iterative levels, which are level 1, level 3 and level 4. The iDose level is selectable, and it reflects a scale of how aggressively the noise reduction is performed relative to noise that would be obtained if reconstructed with FBP. The purpose is to examine the effects of

reconstruction filters on NNPS using traditional geometry (i.e. non-helical). In particular, the effects of the traditional roll-off smooth filter (A,B) and the enhancing filter (C, D, DH) will be studied. To improve accuracy, the result was averaged over all seven images acquired previously.

Remember that, while NNPS have much potential in the way of standardizing protocols across institutions, certain protocols, such as cardiac imaging, in which the number of projections contributing to the final image at a particular gantry angle can vary, are not emanable for NNPS analysis.

For these iDose levels and convolution filters we calculate the normalized noise power spectrum [see Appendix A for others tables] and we compared each reconstruction level with FBP. The iterative algorithm levels utilized for this study are the ones used in clinic:

- Level 1 is more similar than Filtered Back Projection (10.6% noise reduction).
- Level 3 has a medium reconstruction level (22.5% noise reduction).
- Level 4 has a reconstruction level greater than previous (29.3% noise reduction).

iDose1 vs FBP

Convolution kernels are designed to weight the frequency content of the projection. Therefore, the specific design of the kernel greatly influences the shape of the NPS and the quality of the final images. It following that choosing different convolution kernels allows the user to somewhat control noise texture. Also, the ability to choose a specific kernel allows the user to exploit a fundamental tradeoff in CT between noise and resolution.

In frequency space, most filters follow the same basic ramp-up roll-off design. The ramp is designed to reduce blurring and roll-off portion is highly variable and controls the high-frequency content of the image. As mentioned previously, sharp kernels preserve more high frequency content and thus result in better spatial resolution. The limit for high resolution is increased noise at high spatial frequencies. Soft kernels suppress high frequency content and offer reduced noise at the cost of lower spatial resolution.

We analyze [Fig. 3.11] and focus on different aspects such as the shape at low frequencies, the slope at high frequencies and noise reduction for all kernels, starting from Filtered Back Projection.

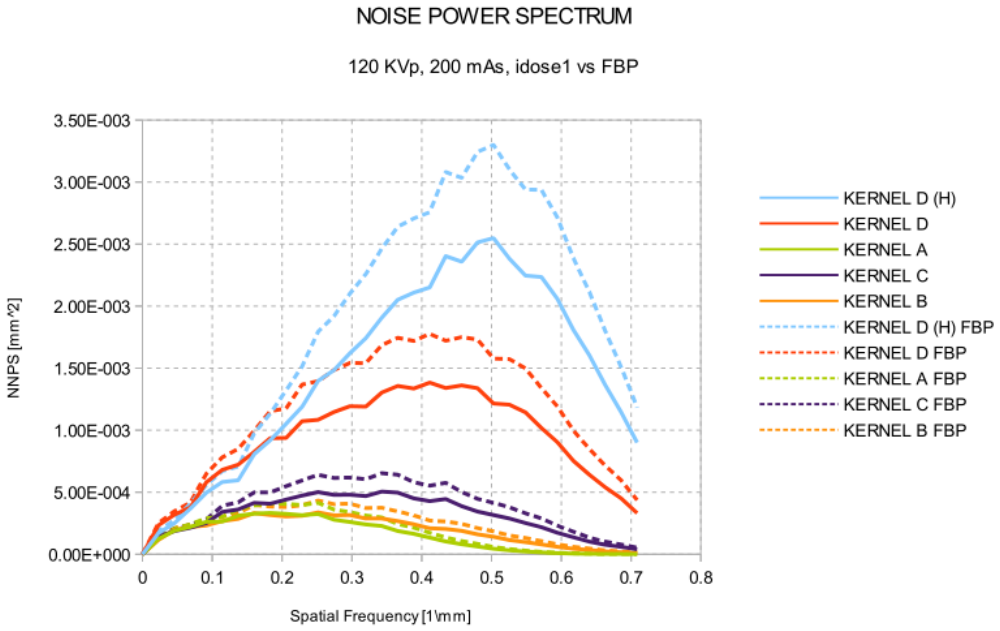

Figure 3.11: Trend of noise power spectrum for all reconstruction kernels. Radially averaged normalized NPS curves show how noise texture is manifested in the NPS.

- *Shape analysis at low frequencies*: for range between 0 and 0.1 mm^{-1}, kernel DH has less noise than kernel D (both iterative and standard) while kernel DH FBP has the same noise texture of iterative kernel D. Instead, for other kernels the NNPS is overlying and impossible to study.

  For range between 0.1 mm^{-1} and 0.2 mm^{-1} the sharp filters tends to have different trends, the NNPS varies slightly therefore can be studied. The smooth filters (A,B) don't allow us to study the noise texture. The use of smooth filters does not make much sense for the previous reason, however a comparison of sharp filters is useful to understand when to use them.

- *Slope analysis at high frequencies*: for values higher than 0.5 mm^{-1}, the trend of sharper filters drops more quickly than smooth filters. However, kernel A,B and C go down from 0.25 mm^{-1} and lowest values of the curves overlap.

  The convolution kernels D,DH improve spatial resolution but, as we can see from the plot, the noise values are higher and are unable to discern with higher intensity than the ones of other filters.

- *Noise reduction*: By using iterative algorithms the noise power is much

lower than standard reconstruction, for sharp filter the difference is more marked in a range between 0.2 and 0.6 mm^{-1} for kernel DH, while it is remarkable between 0.2 and 0.55 mm^{-1} for kernel D. The difference is much lower for smooth filters, especially for kernel A there is little difference between 0.2 and 0.3 mm^{-1}. Images with coarse texture have an NNPS concentrated at low frequencies (kernel A,B) while images with finer texture have an NNPS concentrated at higher frequencies (kernel D,DH)[33].

iDose3 vs FBP

Level 3 of iterative algorithm shows further differences than level 1. The curves are similar but at some frequency range they overlap, and we must be careful to select which filters are used for analysis.

We repeat the previous procedure to analyze the noise power spectrum.

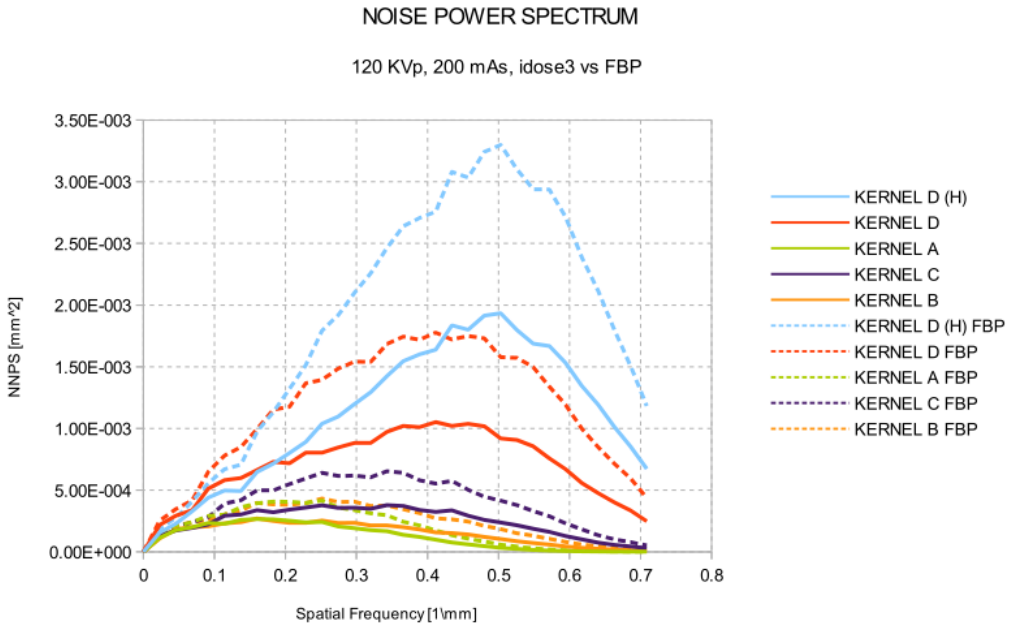

Figure 3.12: Trend of noise power spectrum for all reconstruction kernels. Note the differences at $\sim$ 0.45 mm^{-1} and $\sim$ 0.3 mm^{-1}.

- *Shape analysis at low frequencies*: for $\sim$ 0.2 mm^{-1}, iDose3 kernel DH has less noise than kernel D (FBP) even if the first one is high resolution. The sharper filters (with iterative reconstruction) shows oscillating curves which intersect in two points ($\sim$ 0.08 and $\sim$ 0.18 mm^{-1}).

The difference shown is greater than iDose1 analysis. The noise texture for sharp kernels (both FBP and iterative) is impossible to study for values < 0.1, but between 0.1 and 0.2 the trends can be studied (even if the differences are minimal) for standard versus iterative algorithm.

The smooth filters (A,B) for values < 0.1 cannot be studied but between 0.1 and 0.2 the shape and the slope is similar. In this case the difference among two algorithms is lower than sharp filters.

- *Slope analysis at high frequencies*: for values higher than 0.5 mm^{-1}, the sharper filters are steeper than smooth filters. However, smooth kernels (A,B) for iterative and standard reconstruction begin to go down from 0.25 mm^{-1} but for kernel C the curve start to decline for ~ 0.45 mm^{-1}.

  The convolution kernels D,DH improve spatial resolution but, aa can be seen from the plot, the noise values are higher and are unable to discern NNPS variations principally between 1.00×10^{-3} and 3.00×10^{-3}.

- *Noise reduction*: By using iterative algorithms the noise power is much lower than standard reconstruction (this is true for all iDose levels studied), the difference is more marked for the sharp filter in range between 0.1 and 0.7 mm^{-1}. The variation is much lower for smooth filter, starting from ~ 0.1 for kernel C, and from ~ 0.25 for kernel A and B. The main difference with [Fig. 3.11] is that kernel DH (iterative) and kernel D (FBP) are crossing at ~ 0.42; before this value the NNPS for kernel DH is lower than kernel D, while after it becomes higher. Then, we must be careful about which filter use to study a specific spatial frequency range.

iDose4 vs FBP

Level 4 of iterative algorithm shows some peculiarities compared to other reconstruction levels, mainly at high frequency.

Once again, we analyze the three main features which characterize the noise power spectrum analysis. We repeat the same method used previously.

- *Shape analysis at low frequencies*: for values < 0.1 mm^{-1}, both kernel D and kernel DH follow a pattern that respects the characteristics of those filters; for values of ~ 0.05 mm^{-1}, *standard* and *iterative* have a similar NNPS and then we cannot observe a good texture noise variation. For ~ 0.2 mm^{-1} the sharper filters (both iterative and standard), are very similar to each other.

The smooth filters (A,B) for values $< 0.1\ mm^{-1}$ cannot be studied because the variations of NNPS are too small, whereas between 0.1 and 0.2 trends are beginning to take shape allowing to distinguish the values of noise although very small. In this case the difference among two algorithms is similar than sharp filters.

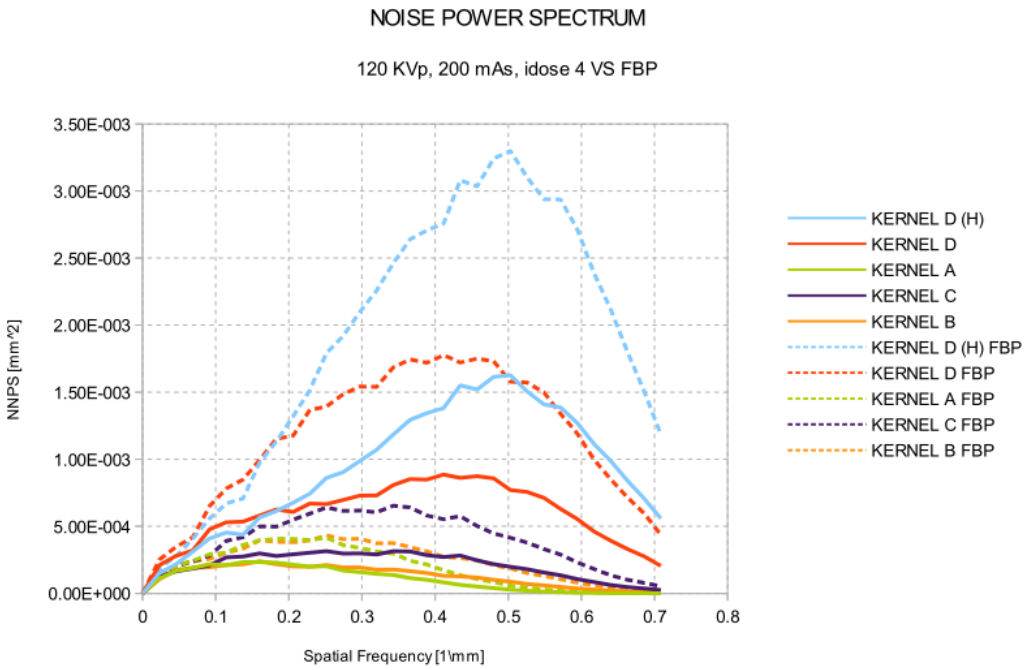

Figure 3.13: Trend of noise power spectrum for all reconstruction kernels. Note the lowest noise power for kernel D (FBP) after 0.55 mm^{-1}.

- *Slope analysis at high frequencies*: for values higher than 0.5 mm^{-1}, iterative reconstruction for smooth kernel tends go down more quickly than FBP. The difference is less remarkable for kernel A, while for kernel B the curve is slightly different although beyond this value is difficult to make an accurate assessment. It is clear from the graph that NNPS do not ramp up as to the traditional roll-offs shown for smooth kernel (this for all reconstruction levels). Sharper filters has a similar slope, especially iterative reconstruction with kernel DH and standard reconstruction with kernel D after 0.55 mm^{-1}.

- *Noise reduction*: In Fig.[3.11], we show the NNPS associated to the standard roll-off filters (kernel A,B,C), ranging from more smooth to the sharper in their effects. Remembering that these noise power spectrum represent a constant dose condition (200 mAs) for unsubtracted

axial images, the noise power shifts to higher frequencies and aliasing of noise does not occur with the sharper filters in the NNPS. In this case, unlike the previous, one can see two differences: first, at 0.5 mm^{-1} kernel DH (iterative reconstruction) and D (standard reconstruction) overlap; after ∼0.55 mm^{-1} NNPS is lower for FBP but for values <0.5 mm^{-1} the iterative becomes smaller. Second, the smooth filters have the same trend as previously cases except kernel C. Note the low-frequency structured noise is not present. Because most objects are low-frequency dominated, this noise could have a potentially deleterious effect on the object detectability.

Next step is to study and visualize the noise fluctuations within body phantom. This process has been done with all convolution kernels both FBP and iterative reconstruction (See appendix A for other plots), by analyzing all slice acquired. Internally the image is scaled to a square image using nearest neighbor sampling. For selections, the bounding box of the selection is used for the surface plot.

In the left image we have a FBP reconstruction that represent the noise fluctuations (light blue), where x-axis and y-axis is the FOV (field of view). The luminance of an image is interpreted as height for the plot. Internally the image is scaled to a square image using nearest neighbor sampling. Right image represent the iterative reconstruction, it can be noted that the noise fluctuations are less pronounced than filtered back projection.

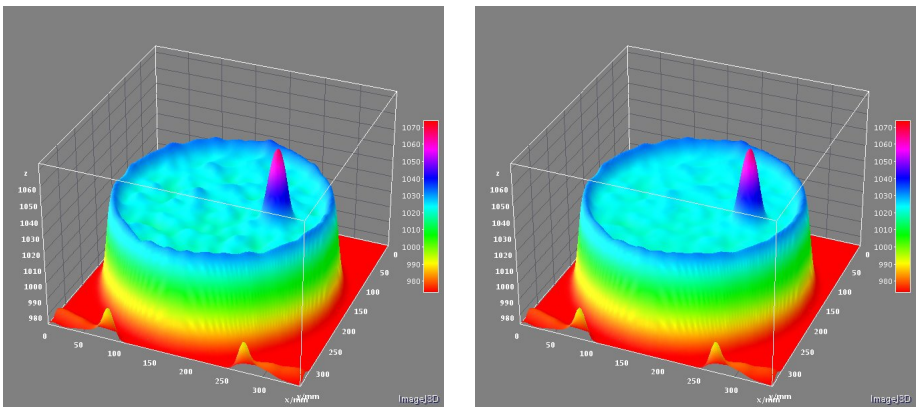

Figure 3.14: Noise texture fluctuations of Filtered Back Projection algorithm with convolution kernel A (LEFT). Noise texture fluctuations of Iterative reconstruction algorithm (iDose, level 4) with same convolution kernel of FBP (RIGHT). The teflon insert is not affected by noise texture and reconstruction algorithm.

Head Phantom

Head phantom unit is composed by three sections. Section 1 is a PMMA transparent box, with a diameter of 225 mm, filled by air. Section 2 and 3 are enclosed in a PVC box with a diameter of 200 mm, filled with distilled water. The head unit is mounted outside, free in air.

- Section 1 is a physical layer and this part is equipped with guides, used to measure the slice width and the impulse response.
- Section 2 is a water layer, used for head calibration and to measure uniformity and noise. Furthermore, the rapid test on the image quality use this section to measure and calculate the low contrast resolution.
- Section 3 is a multiple pins layer, equipped with pins of various materials, used to measure the linearity of brain mode and the contrast scale. This section has a pin used to measure the spatial resolution in standard mode.

Voltage	120 kVp
Exposure	200 mAs
Beam Collimation	64×0.625
Convolution Kernel	A, EB, UB, C, D, D(H)
Slice Thickness	2.5 mm
Pixel Sixe	0.4882×0.4882 mm
FOV	250×250 mm
Rotation time	0.75 s
Matrix Size	512 × 512

Table 3.2: List of parameters utilized.

Kernel UB	Smooth	Improves bone-braine interface, No effects on HU values
Kernel EB	Smooth	Head scans only, increase to observed HU values

Figure 3.15: Convolution kernel for Head Phantom.

For noise characterization, to generate an image noise similar to a clinical head scan, an homogeneous phantom filled with water, which mimics a

normo-type head, was used. To reproduce the clinical conditions, the FOV of 250 mm was used for the homogeneous phantom acquisition.

For each reconstruction stack of 16 images, a subset of 7 images was processed with QA-distribution (imageJ plugin). For each image, the NNPS from a 64×64 region of interest (ROI) fragments at the image center was calculated and subtracted pixel-by-pixel from the same ROI to cancel the Fourier Transform dc component. The dc component is not useful to a human observer because, the human visual response is low at low frequencies and the absolute image brightness cannot be used as an image feature for detection.

The noise power spectrum was produced by squaring the FFT magnitude image and, finally, the NPS stack was averaged using seven images to generate a single NNPS image with better accuracy. The ROI used was large enough to accurately identify the low frequencies in the NNPS.

To compare and present the results, the mono-dimensional NNPS were extracted from the 2D images with a radial average of the data points (exactly as for the other phantom).

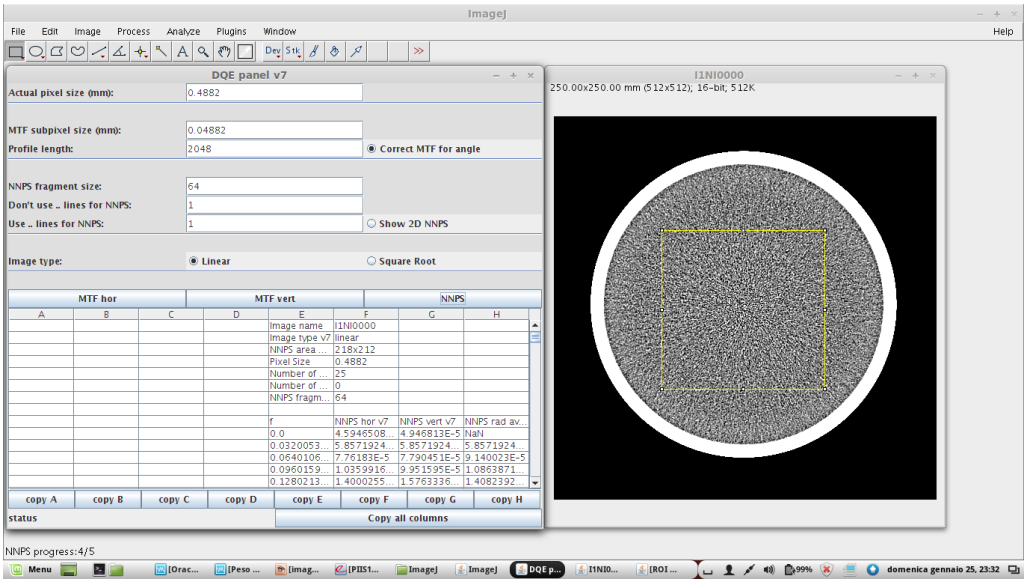

Figure 3.16: Spatial frequency (mm^{-1}) and radially NNPS values (mm^2) (LEFT). Head phantom image and region of interest utilized for calculate the Normalized Noise Power Spectrum (RIGHT).

Spatial Frequency	Slice 1	Slice 2	Slice 3	Slice 4	Slice 5	Slice 6	Slice 7	Average values Kernel A
0	0	0	0	0	0	0	0	0
0.0320053257	2.86E-005	2.96E-005	2.52E-005	1.81E-005	2.18E-005	3.02E-005	3.18E-005	2.65E-005
0.0640106514	3.42E-005	4.30E-005	3.42E-005	3.38E-005	2.84E-005	3.82E-005	3.92E-005	3.67E-005
0.0960159771	4.59E-005	4.33E-005	4.27E-005	4.28E-005	4.02E-005	4.18E-005	4.77E-005	4.68E-005
0.1280213027	5.87E-005	4.70E-005	4.63E-005	4.59E-005	5.20E-005	5.14E-005	4.71E-005	5.29E-005
0.1600266284	5.35E-005	5.39E-005	4.63E-005	5.60E-005	5.37E-005	6.52E-005	6.02E-005	5.68E-005
0.1920319541	6.50E-005	6.15E-005	6.15E-005	5.93E-005	4.72E-005	5.87E-005	5.16E-005	5.83E-005
0.2240372798	6.26E-005	5.66E-005	6.38E-005	6.41E-005	6.05E-005	5.23E-005	5.44E-005	5.85E-005
0.2560426055	5.66E-005	5.90E-005	5.76E-005	5.78E-005	6.62E-005	5.39E-005	4.96E-005	5.31E-005
0.2880479312	4.93E-005	5.31E-005	5.25E-005	5.66E-005	5.17E-005	5.04E-005	4.84E-005	4.88E-005
0.3200532569	4.81E-005	4.74E-005	4.79E-005	4.37E-005	4.44E-005	4.07E-005	4.51E-005	4.66E-005
0.3520585825	4.00E-005	3.47E-005	4.51E-005	3.96E-005	4.17E-005	3.70E-005	3.64E-005	3.82E-005
0.3840639082	3.19E-005	3.40E-005	3.36E-005	3.46E-005	3.28E-005	3.22E-005	3.21E-005	3.20E-005
0.4160692339	2.71E-005	2.52E-005	2.41E-005	2.61E-005	2.50E-005	2.55E-005	2.59E-005	2.65E-005
0.4480745596	1.68E-005	1.81E-005	1.75E-005	1.89E-005	1.80E-005	1.88E-005	1.86E-005	1.77E-005
0.4800798853	1.38E-005	1.33E-005	1.21E-005	1.28E-005	1.29E-005	1.42E-005	1.32E-005	1.35E-005
0.512085211	1.02E-005	8.98E-006	7.76E-006	8.98E-006	9.21E-006	9.68E-006	8.46E-006	9.35E-006
0.5440905367	5.64E-006	5.53E-006	5.41E-006	5.60E-006	5.40E-006	5.63E-006	5.63E-006	5.63E-006
0.5760958624	3.63E-006	3.39E-006	3.15E-006	3.67E-006	3.39E-006	3.46E-006	3.30E-006	3.47E-006
0.608101188	2.12E-006	1.97E-006	1.90E-006	1.88E-006	2.02E-006	1.97E-006	2.01E-006	2.06E-006
0.6401065137	1.20E-006	1.11E-006	1.03E-006	1.22E-006	1.18E-006	1.15E-006	1.18E-006	1.19E-006
0.6721118394	7.01E-007	6.21E-007	6.28E-007	6.56E-007	6.88E-007	5.89E-007	6.27E-007	6.64E-007
0.7041171651	4.35E-007	4.07E-007	3.96E-007	4.42E-007	4.16E-007	3.88E-007	4.26E-007	4.30E-007
0.7361224908	3.36E-007	3.09E-007	2.98E-007	3.27E-007	3.07E-007	2.82E-007	3.38E-007	3.37E-007
0.7681278165	2.52E-007	2.40E-007	2.42E-007	2.63E-007	2.52E-007	2.32E-007	2.63E-007	2.57E-007
0.8001331422	2.38E-007	2.10E-007	2.12E-007	2.38E-007	2.28E-007	2.01E-007	2.35E-007	2.37E-007
0.8321384678	2.09E-007	1.81E-007	1.84E-007	2.06E-007	1.89E-007	1.78E-007	1.97E-007	2.03E-007
0.8641437935	1.98E-007	1.77E-007	1.77E-007	1.95E-007	1.79E-007	1.77E-007	1.95E-007	1.97E-007
0.8961491192	1.90E-007	1.68E-007	1.63E-007	1.79E-007	1.70E-007	1.64E-007	1.86E-007	1.88E-007
0.9281544449	1.69E-007	1.53E-007	1.45E-007	1.63E-007	1.61E-007	1.45E-007	1.70E-007	1.70E-007
0.9601597706	1.56E-007	1.55E-007	1.44E-007	1.62E-007	1.53E-007	1.37E-007	1.72E-007	1.64E-007
0.9921650963	1.53E-007	1.35E-007	1.36E-007	1.53E-007	1.41E-007	1.34E-007	1.49E-007	1.51E-007

Figure 3.17: Values of NNPS calculate for all seven slice with FBP algorithm and Convolution kernel A. Note the different values of spatial frequency for head phantom compared to body phantom.

iDose1 vs FBP

The reconstruction kernel is defined as the image processing filter applied to the raw data to yield a final scan image. The sharpness of the final image is most directly influenced by the type of filter employed. The kernels usually have more straightforward names such as smooth kernels (A, EB, UB).

These filters will tend to smooth edges and reduce the amount of image noise. In the head are used to study the soft part of the brain that has low contrast.

Sharp kernels (C, D, DH) tend to enhance edges at the cost of increased overall image noise.

The predominant source of noise is the x-ray photon concentration fluctuation, called quantum noise. The prevalence of noise makes convolving our signal with a filter necessary.

We analyze Fig.[3.18-3.19] and focus on different aspects such as the shape at low frequencies, the slope at high frequencies and noise reduction for all kernels, starting from Filtered Back Projection (exactly as for body phantom). Kernels UB and EB have been studied separately, because these filters are very similar to each other.

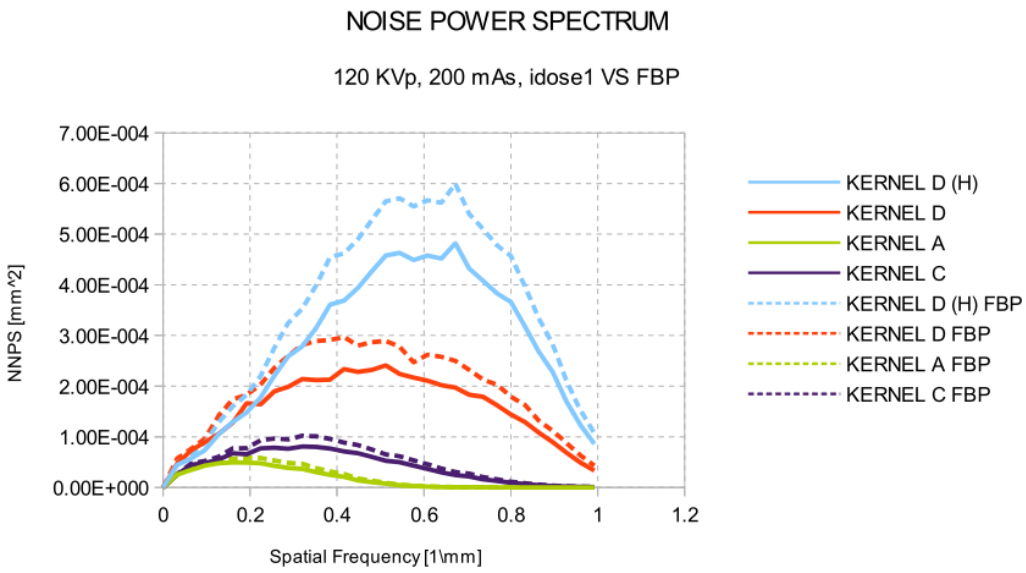

Figure 3.18: Trend of noise power spectrum for all reconstruction kernels, except kernels UB-EB. Radially averaged normalized NPS curves show how noise texture is manifested in the NPS.

- *Shape analysis at low frequencies*: These curves are very similar to each other for values less than 0.2 mm^{-1}. Smooth filter A and sharp filter C are overlap for iterative and filtered back projection reconstruction, then both can be used to improve contrast resolution in this range of frequencies. The shape of NNPS for $\sim$ 0.2 mm^{-1} begins to change, and for values greater than 0.2, we must be careful which filter to use if we want to make a thorough analysis.

  For sharper filters (D and DH), NNPS overlaps at $\sim$ 0.1 mm^{-1}. Compared to iDose1 for body phantom, we note that the curves are similar and from this value onwards they take slightly different trends.

- *Slope analysis at high frequencies*: There are many differences in comparison to body phantom. First, the peaks of kernel DH (both iterative and standard) are shifted beyond 0.6 mm^{-1} compared to [Fig. 3.11] and this affects the texture of the image. For kernel D at spatial frequency of $\sim$ 1 mm^{-1}, both curves overlap and it is difficult to estimate the correct measure for this range of frequency. Not only that, but in this case, using the iterative or FBP will not change the result of reconstruction. Kernels A and C are impossible to study because the differences are virtually undetectable.

- *Noise reduction*: For head phantom, the values of NNPS are lower than body phantom (for all kernels). For kernel DH the curve is less noisy

and steep than FBP; there is a plateau at $\sim 0.6\ mm^{-1}$, which means that the texture fluctuations are less noticeable compared to [Fig. 3.11]. For kernel DH the greater difference is between 0.5 and 0.7 mm^{-1}, and accordingly towards the higher frequencies compared to kernel DH for body phantom. For kernel D is $\sim 0.38\ mm^{-1}$, therefore tends to go to lower frequencies compared to kernel D for body phantom. Kernel A goes towards zero at 0.5 mm^{-1}, i.e. for the same value of Fig.[3.11]; iterative and FBP reconstruction have the same NNPS (same shape). For iterative algorithm, kernel C is slightly different than FBP reconstruction as it varies only in a small range of frequencies (from 0.2 to 0.4 mm^{-1}).

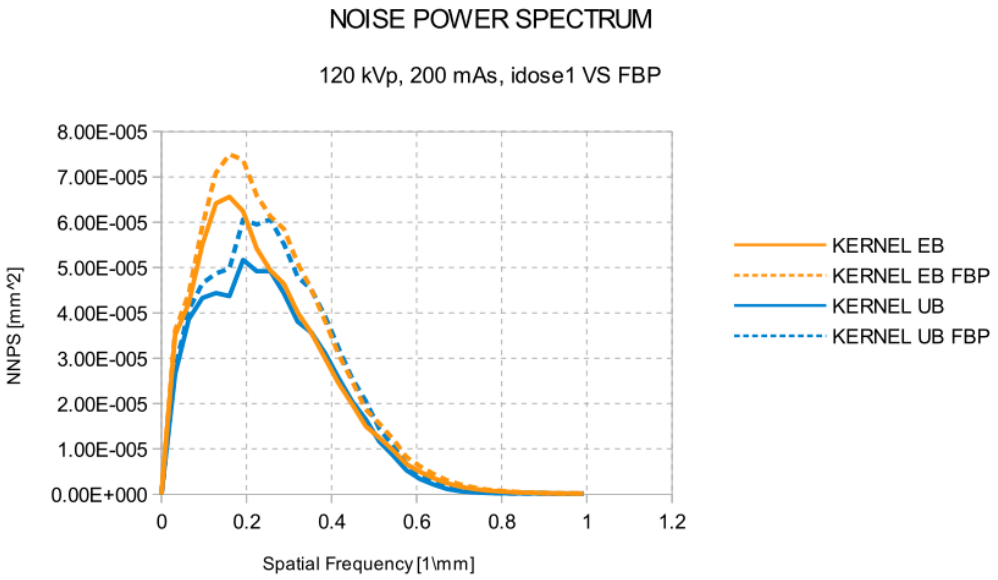

Figure 3.19: Comparison between smooth convolution kernels for head acquisition. UB improves bone-brain interface and no effect on HU values; EB head scans only and increased to observed HU values (not shown here).

- *Comparison between kernel UB and EB*: These two filters are very similar; they both work at lower spatial frequencies, which is a sign that these kernels are more suited for the study of contrast resolution (e.g. abdomen, skull). For values beyond 0.5 mm^{-1}, these filters are completely unnecessary as there are no variations in the values of NNPS. The major changes occur at lower frequencies, in fact we observe several things: first of all, the curve of kernel EB is too smooth compared to the kernel UB, therefore is subject to minor fluctuations in the texture of the image. However, filter EB presents a level of NNPS greater

than filter UB, even if it comes to very small values.

iDose3 vs FBP

Remember that iDose[4] is a hybrid iterative reconstruction algorithm that provides reduced image noise compared with the conventional filtered back projection. Level 3 of reconstruction for the head phantom has several similarities with level 3 of body phantom indeed even here the noise is reduced, in a slightly better way than body. We now repeat the same considerations made for all other cases.

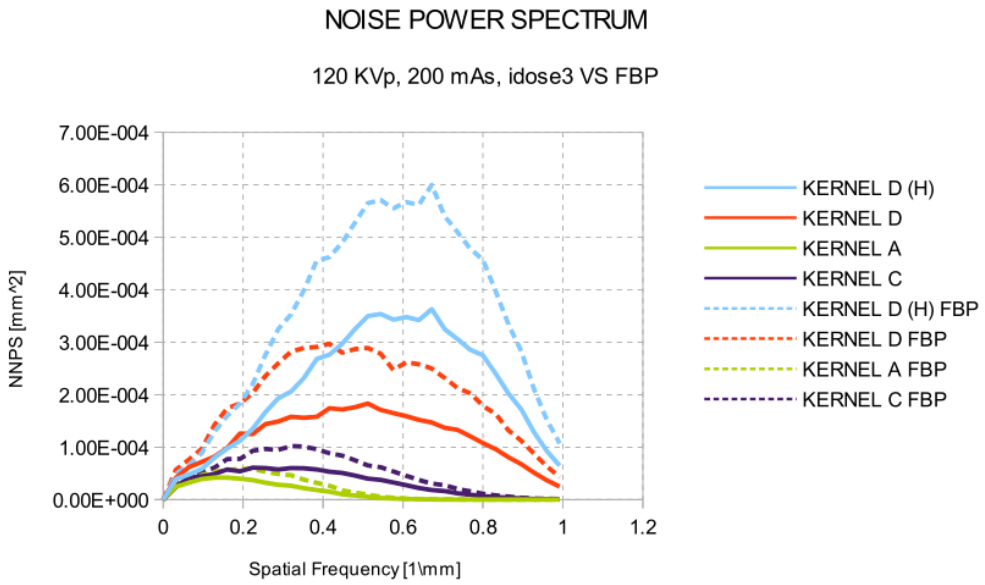

Figure 3.20: Trend of noise power spectrum for all reconstruction kernels, except kernels UB-EB. Radially averaged normalized NPS curves show how noise texture is manifested in the NPS.

- *Shape analysis at low frequencies*: This small range is identical to the smooth kernel A (both iterative and standard reconstruction) compared to body phantom. For $\sim 0.2\ mm^{-1}$ kernel A (FBP) and kernel C (iterative) overlap, and then their use to analyze the texture in this range is the same as before. Sharper filters (D and DH) have similar trends and begin to diversify for values $> 0.2\ mm^{-1}$. We note that, in this case, there are no differences between iDose3 for head phantom and iDose3 for body phantom.

- *Slope analysis at high frequencies*: For higher frequencies the curves for kernel DH go down for values $> 0.6\ mm^{-1}$. Kernel D for standard

reconstruction go down for values $> 0.4\ mm^{-1}$; instead kernel D for iterative decreases after $0.5\ mm^{-1}$. The other two filters analyzed, at frequencies $> 0.7\ mm^{-1}$ do not give contribution. This is correct because most of the information is given at lower frequencies.

- *Noise reduction*: Also here, the variations of noise power spectrum are greater than level 1 of reconstruction, which is observed in particular for sharper kernels. The main changes are found around $0.4\ mm^{-1}$ for kernel D, around $0.6\ mm^{-1}$ for kernel DH, around $0.3\ mm^{-1}$ for kernel C and around $0.25\ mm^{-1}$ for kernel A (although, in the latter case, the variations are too small). Since the amplitude of the NNPS is greater than iDose1 (especially for kernel DH), the trends of the curves here overlap. For example, all kernels will tend to overlap at lower values of the NNPS.

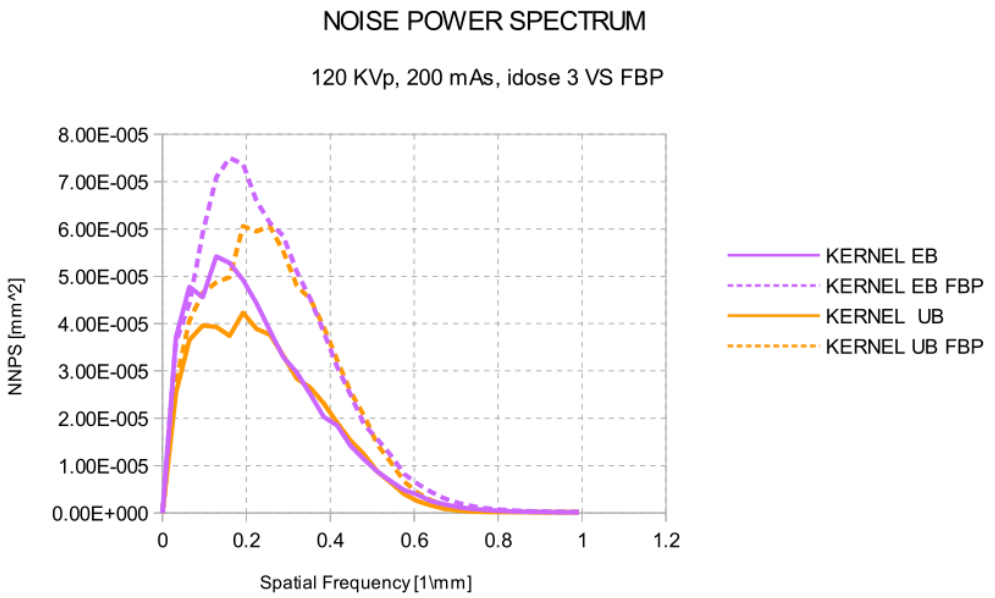

Figure 3.21: Comparison between smooth convolution kernels for head acquisition. UB improves bone-brain interface and no effect on HU values; EB head scans only and increased to observed HU values (not shown here).

- *Comparison between kernel UB and EB*: The NNPS is lower than the previous case (for iterative algorithm). In this level of reconstruction, kernel EB and UB show differences respect to level 1 of reconstruction. First, kernel EB go down from $6.5 \times 10^{-5} mm^2$ to $5.5 \times 10^{-5} mm^2$ and shows a fall around the value of $0.1\ mm^{-1}$, afterwards it goes up immediately to $0.15\ mm^{-1}$ then decreases steadily to zero at $\sim 0.7\ mm^{-1}$.

Kernel UB shows a less relevant peak and has a value of NNPS lower than level 1; further between 0.35 and 0.4 mm^{-1} it does not overlap with the other filter, whereas previously the overlap is more marked for values > 0.25 mm^{-1}.

iDose4 vs FBP

Compared to pixel standard deviation, NPS has greater clinical potential for task-based image quality assessment, describing both the magnitude and spatial frequency characteristics of image noise. While iDose^4 reduces the NPS magnitude more dramatically than FBP, further studies are needed to assess the impacts of noise texture alteration on its clinical usage. Compared to FBP, the iDose^4 algorithm reduced the NPS magnitude while preferentially reducing noise at mid-range spatial frequencies, altering noise texture. This reduction was more significant with increasing iDose^4 noise reduction level.

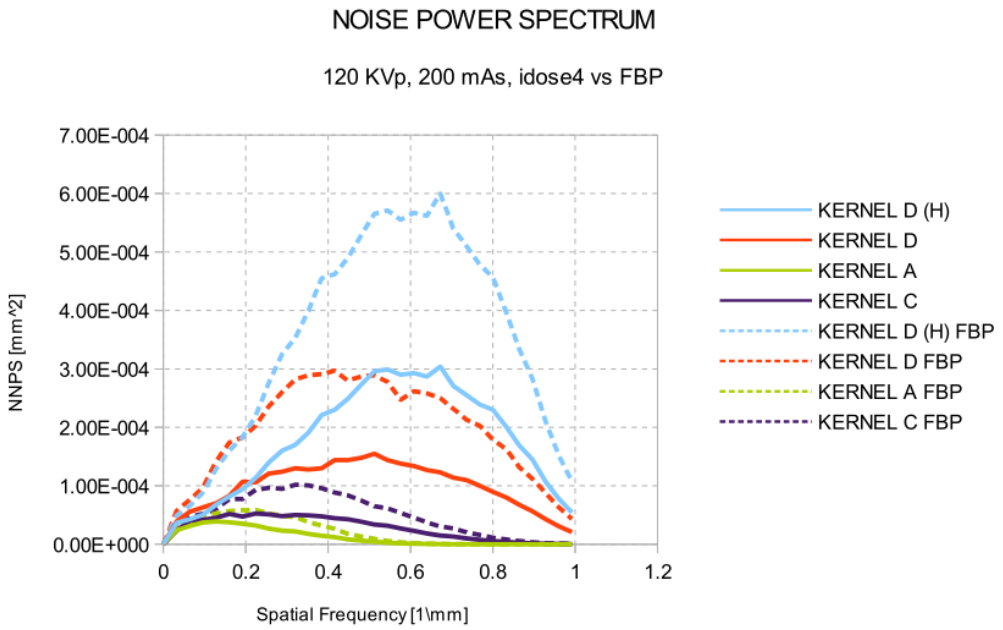

Figure 3.22: Trend of noise power spectrum for all reconstruction kernels, except kernels UB-EB. Radially averaged normalized NPS curves show how noise texture is manifested in the NPS.

- *Shape analysis at low frequencies*: In this range the situation can be summarized as follows. The shape is identical to the previous cases, moreover for values < 0.1 mm^{-1} the curves are indistinguishable and for range between 0.1 and 0.2 slight differences starts to be seen. The

iterative reconstruction allows a better noise reduction than filtered back projection, and the smooth filters have a similar behavior if we want to analyze the contrast resolution.

- *Slope analysis at high frequencies*: Kernel A and C do not give contribution at high frequencies ($> 0.8\ mm^{-1}$). Kernel D and DH behave differently than the two iterative levels previously analyzed. In this case, the high resolution filter tends to almost overlap filter D (FBP); at a closer look, the iterative has a value of NNPS which is slightly higher, and this is due to the shift of the curve towards the higher frequencies.

- *Noise reduction*:We remember that the NPS can be thought as the variance associated with a particular frequency component of an image. For a flat-field image, NPS is the variance associated with a particular frequency component of the noise in that image. In most cases, noise may be represented or approximated, as a stationary Gaussian random process with zero-mean.

  Even in this situation, the NNPS magnitude is reduced (especially for level 4) through the use of an iterative reconstruction. Kernel DH (iterative) and kernel D (FBP) have the same value of NNPS ($3 \times 10^{-4} mm^2$), but have different texture because the first kernel has a peak shifted toward higher frequencies compared to kernel D (FBP). Therefore, the filter DH (iterative) has a spatial resolution better than filter D (FBP), in fact the peak is shifted at high frequencies. Farther, both kernels have the same NNPS amplitude. Unlike the level 3 of reconstruction, at $0.2\ mm^{-1}$ kernel A (FBP) has NNPS slightly higher than kernel C (iterative), but at $0.4\ mm^{-1}$ the situation is reversed.

- *Comparison between kernel UB and EB*: This level of reconstruction has some differences compared to the previous cases. Iterative kernel EB has one peak and does not present changes in the curve of NNPS up to $0.12\ mm^{-1}$. After this value, it begins to fall steadily reaching zero for spatial frequency of $\sim 0.7\ mm^{-1}$.

  Unlike the previous cases (levels 1 and 3), kernel UB presents two peaks at the same value of NNPS ($\sim 4 \times 10^{-5} mm^2$) for spatial frequencies 0.1 and $0.2\ mm^{-1}$. Then this filter has a trend less uniform than kernel EB, but as before it overlap from 0.25 to $0.5\ mm^{-1}$ showing an identical behavior to filter EB.

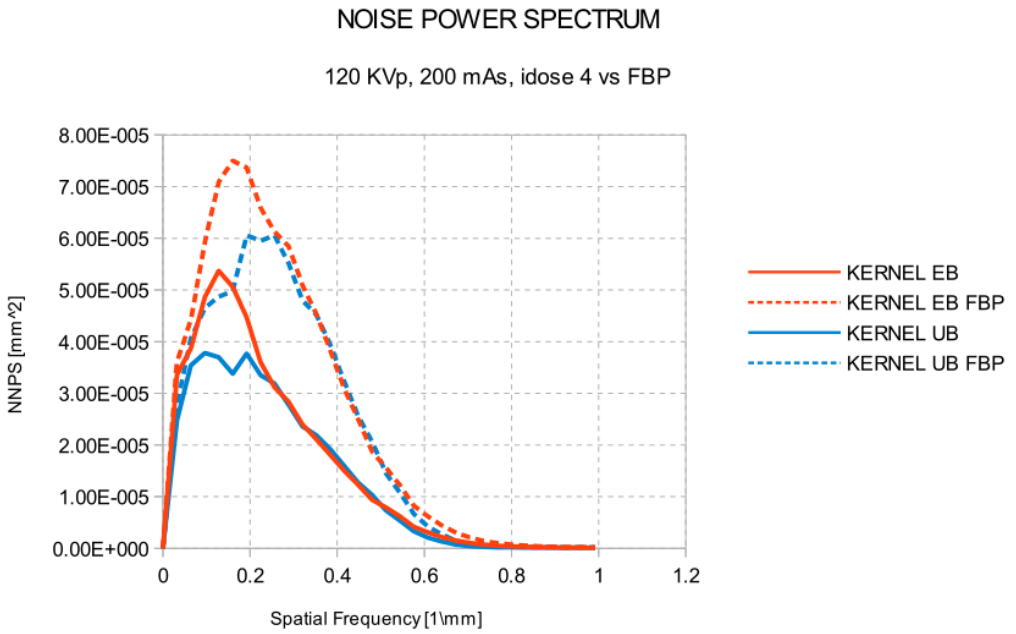

Figure 3.23: Comparison between smooth convolution kernels for head acquisition. UB improves bone-brain interface and no effect on HU values; EB head scans only and increased to observed HU values (not shown here).

As for the case of body phantom, here also it is possible to observe and analyze noise fluctuations. The teflon pin is not present, and the fluctuations are similar to those already observed in the body phantom. Both images represent the convolution kernel DH. On the x-y plane there is the field of view (FOV), which is smaller than Fig.[3.14].

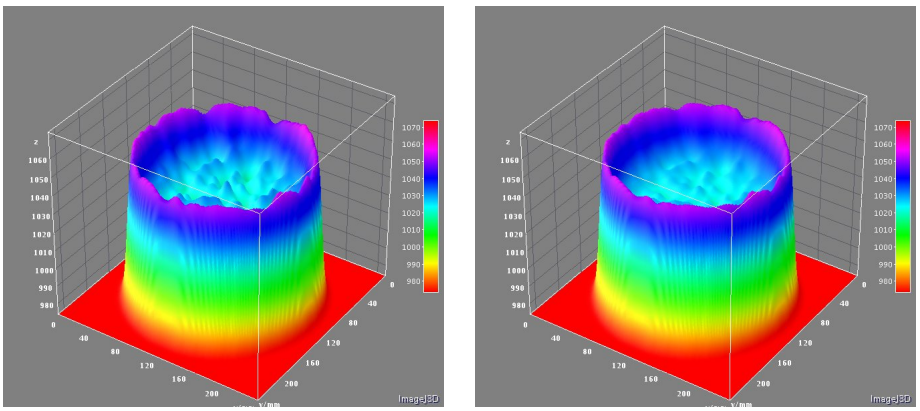

Figure 3.24: Noise texture fluctuations of Filtered Back Projection algorithm with convolution kernel DH (LEFT). Noise texture fluctuations of Iterative reconstruction algorithm (iDose, level 4) with same convolution kernel of FBP (RIGHT).

3.2 Modulation transfer function analysis

Another common metric of image quality is the MTF, which US FDA (Food and Drug Administration) accepts as one component of performance validation for solid state digital detectors. The MTF, related to image resolution, is the Fourier transform of the point spread function (PSF), the systems response to a point object. The MTF and PSF are useful quantities for linear, shift-invariant systems, where the imaging systems response to an arbitrary object can be determined by convolving the true object and the point spread function.

This is not true for nonlinear IR algorithms or even for FBP when nonlinear filters are used. For nonlinear systems, the MTF whose definition assumes independence of location in the image, dose, contrast, and algorithm parameters-acquires dependence on these quantities. As the MTF is not well defined for images reconstructed by IR, it is of limited utility in assessing the quality of these images[34].

Spatial resolution is an important attribute of any radiological imaging system. In CT, spatial resolution depends not only upon physical parameters such as the focal-spot size and detector element dimensions similar to projection radiography, but because all CT images are reconstructed mathematically, the resolving power of a CT image is fundamentally linked to the image reconstruction methods as well. In addition to traditional filtered back projection (FBP) reconstruction algorithms, which utilize a variety of reconstruction kernels that have a profound impact on spatial resolution, iterative CT image reconstruction techniques using statistical or model based constructs are also used clinically. These non linear, adaptive algorithms create a challenging mathematical environment for objectively characterizing spatial resolution[35].

The spatial resolution of a CT measurement is affected by a multitude of factors. Substantial contributions are the properties of the CT device, namely the x-ray source (focal spot size) and the detector (pixel size, scattering), but also the used magnification in cone-beam geometry. The measurement strategy, especially the number of projections per full rotation, and the reconstruction process (voxel size, interpolation, filtering) have a big influence too.

Spatial resolution refers to the ability of an image to convey detail; medical imaging systems produce images that are usually degraded in detail compared with the actual object being imaged.

Fourier based metrology is a prevalent approach to characterizing medical imaging performance. This includes the MTF, which characterizes the resolution of the imaging system. The output signal $I(x, y)$ (i.e., image)

is related to the input signal $f(x, y)$ (i.e., object) by the impulse response function as

$$I(x, y) = \int_{y=-\infty}^{+\infty} \int_{x=-\infty}^{+\infty} f(x - x', y - y') PSF(x', y') dx' dy' \tag{3.2}$$

where $PSF(x, y)$ is defined as the PSF such that

$$\int \int PSF(x, y) dx dy = 1 \tag{3.3}$$

The Fourier representation of the PSF is the optical transfer function (OTF)

$$OTF(u, v) = F\{PSF(x, y)\} \tag{3.4}$$

where F{ } denotes the Fourier transform. The MTF is the modulus of the OTF as

$$MTF(u, v) = |OTF(u, v)| \tag{3.5}$$

describing the magnitude of transferred signal at each spatial frequency. Note that (3.3) implies that $MTF(0) = 1$ (dc signal magnitude is unchanged by the transfer function); and an ideal system has $MTF = 1$ at all spatial frequencies.

The MTF can be employed to characterize the resolution of an imaging system in terms of $MTF(f)$ or to reflect the resolution in a scalar form, for example, the frequency (f_{50}) at which $MTF(f)$ reduces to 0.50[36].

Experimentally, it is impractical to measure the PSF directly. That would require imaging of an infinitesimally small object, a 2D delta function, so that $I(x, y) = PSF(x, y)$. If one is to do so, the mean signal magnitude would be correspondingly small and the resulting image would be dominated by noise. More convenient impulse function techniques are typically used for such measurements, such as the LSF, which is the Radon transform of the PSF

$$LSF(x) = \int PSF(x, y) dx dy \tag{3.6}$$

The edge-spread function can be determined by the integration of the line-spread function

$$ESF(x) = \int_{x=-\infty}^{x} LSF(x') dx' \tag{3.7}$$

which can be measured from the image of a sharp edge. This can be rewritten as

$$LSF(x) = \frac{\partial}{\partial x} ESF(x) \tag{3.8}$$

Hence, the PSF, LSF, ESF, and MTF are all related. Equations (3.6)(3.7)(3.8) illustrate that the family of spread functions, are related and that any one of them can be used to assess the resolution of a CT system in the axial plane. The PSF, LSF and ESF are functions that describe resolution in the spatial domain. However, it is common to transform these functions into the spatial frequency domain, to obtain the modulation transfer function[37].

For a radially symmetric MTF, equations from (3.3) to (3.8) together with the Fourier slice theorem suggest that the one-dimensional MTF (i.e., a slice of the full 2D MTF) is given by

$$MTF(f) = \frac{|\int_{-\infty}^{+\infty} LSF(x)e^{-2\pi ifx}dx|}{\int_{-\infty}^{+\infty} LSF(x)dx} \tag{3.9}$$

where here f represents spatial frequency. The integral in the denominator normalizes the MTF to unity at $f = 0$. If the PSF or ESF is measured directly in CT, these functions can be transformed into the LSF using Eqs. (3.6) or (3.8), respectively, for subsequent assessment of the MTF. Although analytical computation of the MTF from the LSF is possible in some cases. Eqs. (3.9) is evaluated in most cases by a computer subroutine.

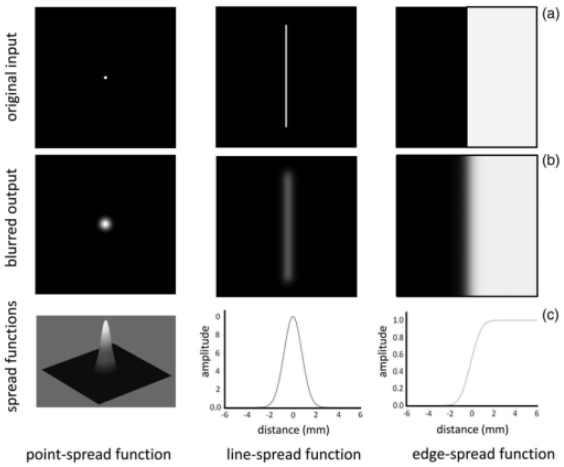

Figure 3.25: (a)Input images defining the point-spread function, the line-spread function and the edge-spread function.(b) Simulated degraded-output images showing raw image data used for the measurements of the PSF, LSF and ESF. The blurring seen in these functions is due to the imperfect resolution properties of the imaging system being characterized.(c) Graphs showing the actual PSF, LSF and ESF. The PSF is a 2D function, and the LSF and ESF are 1D functions.

3.2.1 Test Device and MTF processing

For this study we utilize the Philips phantom (head unit) used in section 3.

The next table shows the acquisition and reconstruction parameters for the Modulation Transfer Function analysis.

Voltage	120 kVp
Exposure	200 mAs
Beam Collimation	64×0.625
Convolution Kernel	A, EB, UB, C, DH
Slice Thickness	1.25 mm
Pixel Sixe	0.3515×0.3515 mm
FOV	180×180 mm
Rotation Time	0.75 s

Table 3.3: List of parameters utilized.

In order to characterize the reconstruction filters used in this study, the MTF of each reconstruction filter was measured. The methodology used to generate these MTF was a wire technique: a wire perpendicular to the scan plane was scanned axially on a multislice CT scanner (ICT 128, Philips Healtcare). The wire was located to the left of the image and acquired with a multiple axial scan using 120 kVp, 200 mAs, 1.25 mm slice thickness and 180 mm reconstruction FOV.

The wire was acquired once and then reconstructed with each filter as indicated in table 3.3. The reconstructed field of view (FOV) was chosen to be small enough to ensure that all frequencies up to the Nyquist frequency (as dictated by the machine sampling rate) would not be aliased by the display grid. A wire image was then generated for each reconstruction algorithm. For each of the resulting wire images, the center of the wire was identified. A spatially invariant linear system is assumed, implying that there is no overlap of system response in frequency space.

However, inside the phantom, there is a slanted wire (50-80 μm tungsten) that reproduced a point spread function witch is suspended in air; since the wire is subpixel sized it is not usually necessary to compensate for its size. Then, we use the impulse source to estimate the point source response function of the CT system. From the print out of a digitized image of the area surrounding the impulse source, we used the numerical data to determine the two-dimensional array of the CT values arising from the impulse source[38].

The FWHM of the point spread function is determined from the best-fit curve of the point spread function numerical data. The average of several different arrays of impulse response functions is calculated to obtain the average point spread function of the system. The point spread function

(PSF) was measured, and then the 2D Fourier transformation of the PSF was performed to obtain a MTF curve. The spatial frequencies at 10% and 50% MTFs were calculated to evaluate the axial resolution[39][40].

All this has been performed through the use of a software called IQ-WORKS. The procedure performed by the software is the following: the software did automatically search the wire and analyzed a squared ROI that contained it. The array analyzed had dimension of 16×16 pixel and from it, central profile was taken and the offset has been eliminated. The software applied a Gaussian filter to reduce the noise, and then has performed a zero-filling Fourier Transform[1]. Finally, from pixel and array dimensions was calculated the correct scale of the spatial frequencies. MTF data are normalized to zero spatial frequency.

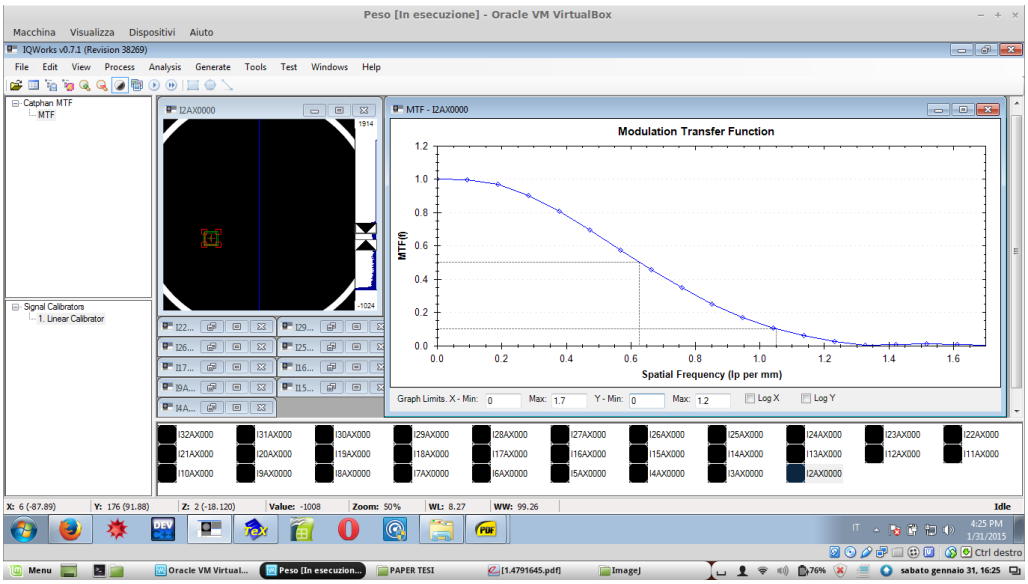

Figure 3.26: Phantom image corresponding to the Philips head phantom using a typical adult head protocol. Image window and level have been adjusted to show bead point source within the ROI (LEFT). Modulation transfer function reconstructed with kernel A; the spatial frequencies at 10% and 50% are shown (RIGHT).

From here on begins the actual analysis. For each MTF was taken one

[1]It turns out that the Fourier transform algorithm used by computer programs is most suited to a number of data points which is a power of 2. So,for example, $2^{14} = 16384$ is a suitable number of data points to transform, but 15000 is not. In practice, therefore, it is usual to zero fill the time domain data so that the total number of points is a power of 2. Zero filling costs nothing in the sense that no extra data is required; it is just a manipulation in the computer. Of course, it does not improve the resolution as the measured signal remains the same, but the lines will be better defined in the spectrum. This is desirable, at least for aesthetic reasons if nothing else.

image with the bead point source that reproduce the point spread function. The IQ WORKS software generates a plot which represents the modulation transfer function with correct spatial frequency; from it were extrapolated values that will be used later to compare the graphs obtained with different convolution kernels (both standard and iterative reconstruction).

spatial frequency	MTF
0	1
0.0948148148	0.9384386228
0.1896296296	0.772019744
0.2844444444	0.5445319516
0.3792592593	0.3222495851
0.4740740741	0.149158286
0.5688888889	0.0457513416
0.6637037037	3.08E-005
0.7585185185	0.0109772441
0.8533333333	0.0069124737
0.9481481481	1.81E-005
1.042962963	0.0060226458
1.1377777778	0.0094143354
1.2325925926	0.0096290254
1.3274074074	0.0061160635
1.4222222222	0.0008407088
1.517037037	0.0050329436
1.6118518519	0.0094790321

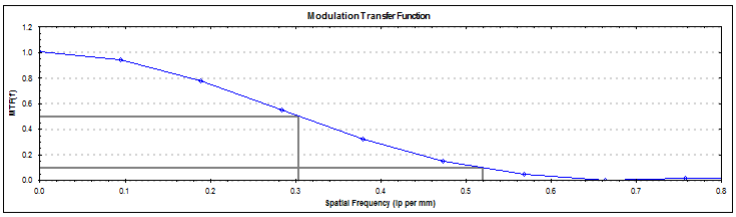

Figure 3.27: MTF values with FBP and iterative algorithm using kernel A (LEFT). MTF plot and values of spatial frequency at 10% and 50% (RIGHT.)

spatial frequency	MTF
0	1
0.0948148148	0.9283517188
0.1896296296	0.7487382798
0.2844444444	0.5277583438
0.3792592593	0.3308806243
0.4740740741	0.1780672256
0.5688888889	0.0783487364
0.6637037037	0.0262480296
0.7585185185	0.0037377886
0.8533333333	0.0013564354
0.9481481481	0.0013787173
1.042962963	0.0058373562
1.1377777778	0.0086202968
1.2325925926	0.008524364
1.3274074074	0.0054127225
1.4222222222	0.0009404866
1.517037037	0.0044033987
1.6118518519	0.0085003539

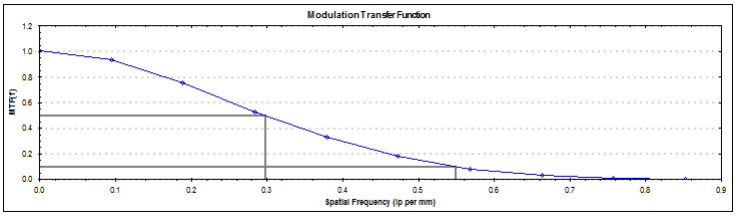

Figure 3.28: MTF values with FBP and iterative algorithm using kernel EB (LEFT). MTF plot and values of spatial frequency at 10% and 50% (RIGHT.)

spatial frequency	MTF
0	1
0.0948148148	0.9422299597
0.1896296296	0.7834789155
0.2844444444	0.5714133064
0.3792592593	0.3600315929
0.4740740741	0.1853626629
0.5688888889	0.0699530634
0.6637037037	0.0116022266
0.7585185185	0.0091362667
0.8533333333	0.0071958057
0.9481481481	0.0005631717
1.042962963	0.0059576558
1.1377777778	0.0100473758
1.2325925926	0.0101148943
1.3274074074	0.0062216544
1.4222222222	0.0009880787
1.517037037	0.0043281878
1.6118518519	0.0093344391

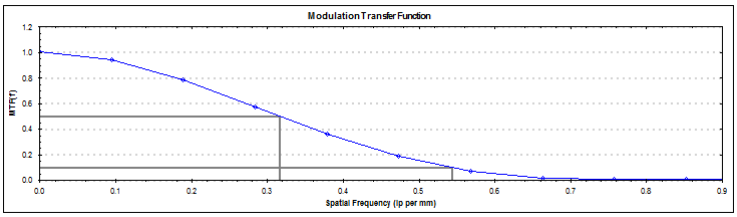

Figure 3.29: MTF values with FBP and iterative algorithm using kernel UB (LEFT). MTF plot and values of spatial frequency at 10% and 50% (RIGHT.)

spatial frequency	MTF
0	1
0.0948148148	0.9608806931
0.1896296296	0.8567389327
0.2844444444	0.701647745
0.3792592593	0.523879085
0.4740740741	0.350054985
0.5688888889	0.2107879518
0.6637037037	0.1102134072
0.7585185185	0.0497792625
0.8533333333	0.0201158106
0.9481481481	0.0086901987
1.042962963	0.0081762193
1.1377777778	0.0094037678
1.2325925926	0.0097083798
1.3274074074	0.0056999549
1.4222222222	0.001508834
1.517037037	0.0048484337
1.6118518519	0.008476084

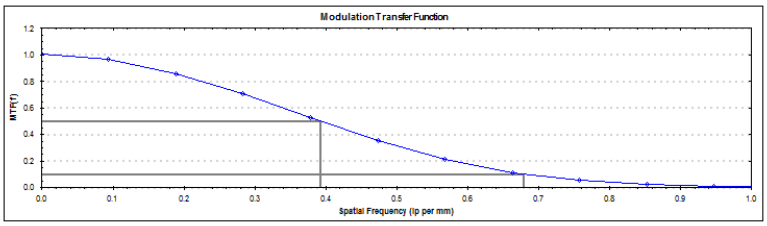

Figure 3.30: MTF values with FBP and iterative algorithm using kernel C (LEFT). MTF plot and values of spatial frequency at 10% and 50% (RIGHT.)

spatial frequency	MTF
0	1
0.0948148148	0.9944724046
0.1896296296	0.9570721124
0.2844444444	0.8827797567
0.3792592593	0.7780160728
0.4740740741	0.6518883424
0.5688888889	0.5254629006
0.6637037037	0.4027326298
0.7585185185	0.2907234669
0.8533333333	0.2029316532
0.9481481481	0.1321009403
1.042962963	0.0772170846
1.1377777778	0.0427934123
1.2325925926	0.020753069
1.3274074074	0.0080452917
1.4222222222	0.0015986289
1.517037037	0.0009222912
1.6118518519	0.0018603101

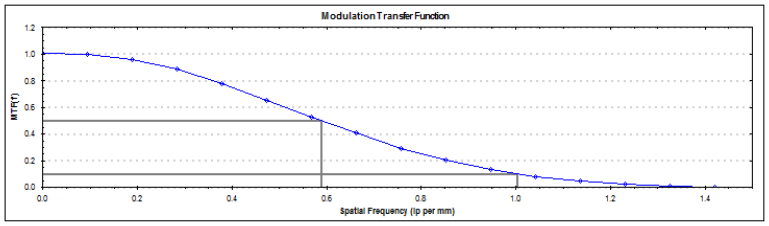

Figure 3.31: MTF values with FBP and iterative algorithm using kernel DH (LEFT). MTF plot and values of spatial frequency at 10% and 50% (RIGHT.)

The high contrast or spatial resolution of the system is often determined using objects having a large signal to noise ratio. Spatial resolution is influenced by factors including:

- System geometric resolution limits-focal spot size, detector width and ray sampling.
- Pixel size.
- Properties of the convolution kernel/mathematical reconstruction filter.

In the previous figures [3.27-3.31] we note a slightly difference between MTFs obtained with all convolution kernels, especially for filter DH. The MTF curve is shifted by higher spatial frequencies, which means that this filter gives a better spatial resolution than others. Typically, these reconstruction filters that enhance or preserve the higher spatial frequencies do so at the cost of increased noise in the image. For high signal to noise objects, this tradeoff is usually acceptable.

The method described here can be used for all images from multislice sequential scans and also for images from helical acquisitions. Scan plane spatial resolution is not generally dependent on helical scan parameters, although the values may be slightly different from those taken with sequential scans due to small differences in acquisition and reconstruction techniques.

Now we plot all modulation transfer functions to show how the reconstruction algorithms behave with different filters. We use five levels of reconstruction to see if there are differences between the trends of curves.

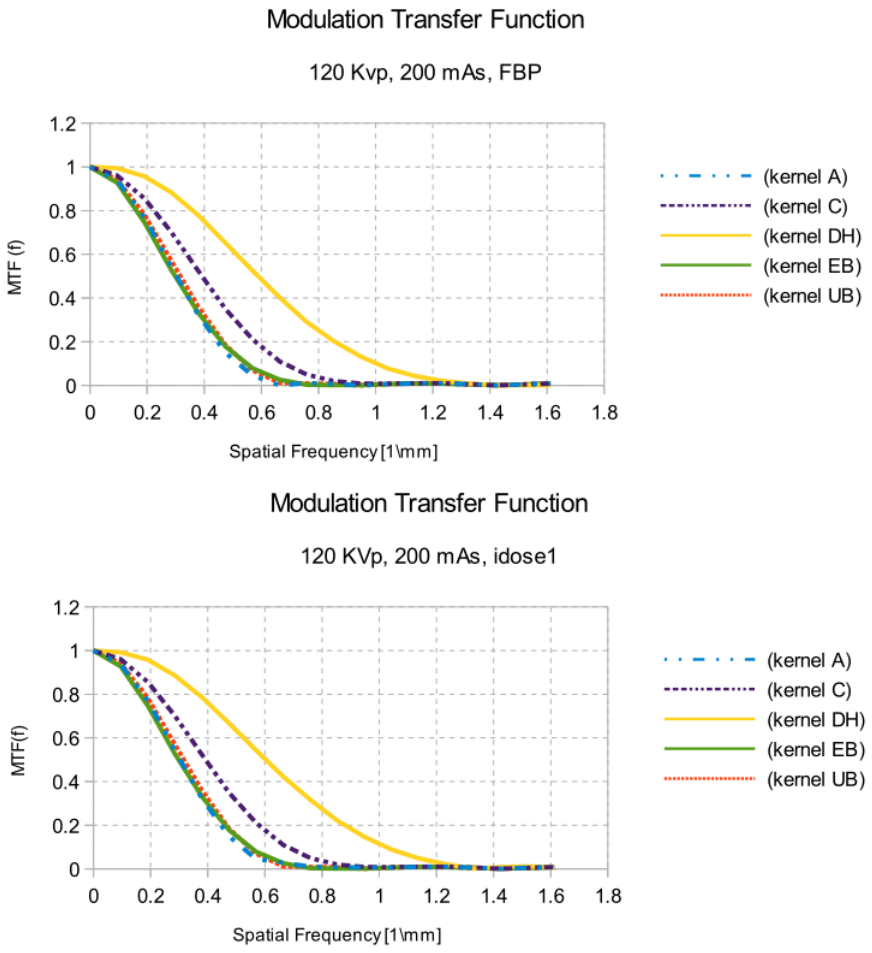

Figure 3.32: MTF for filtered back projection and level 1 of iterative reconstruction algorithm.

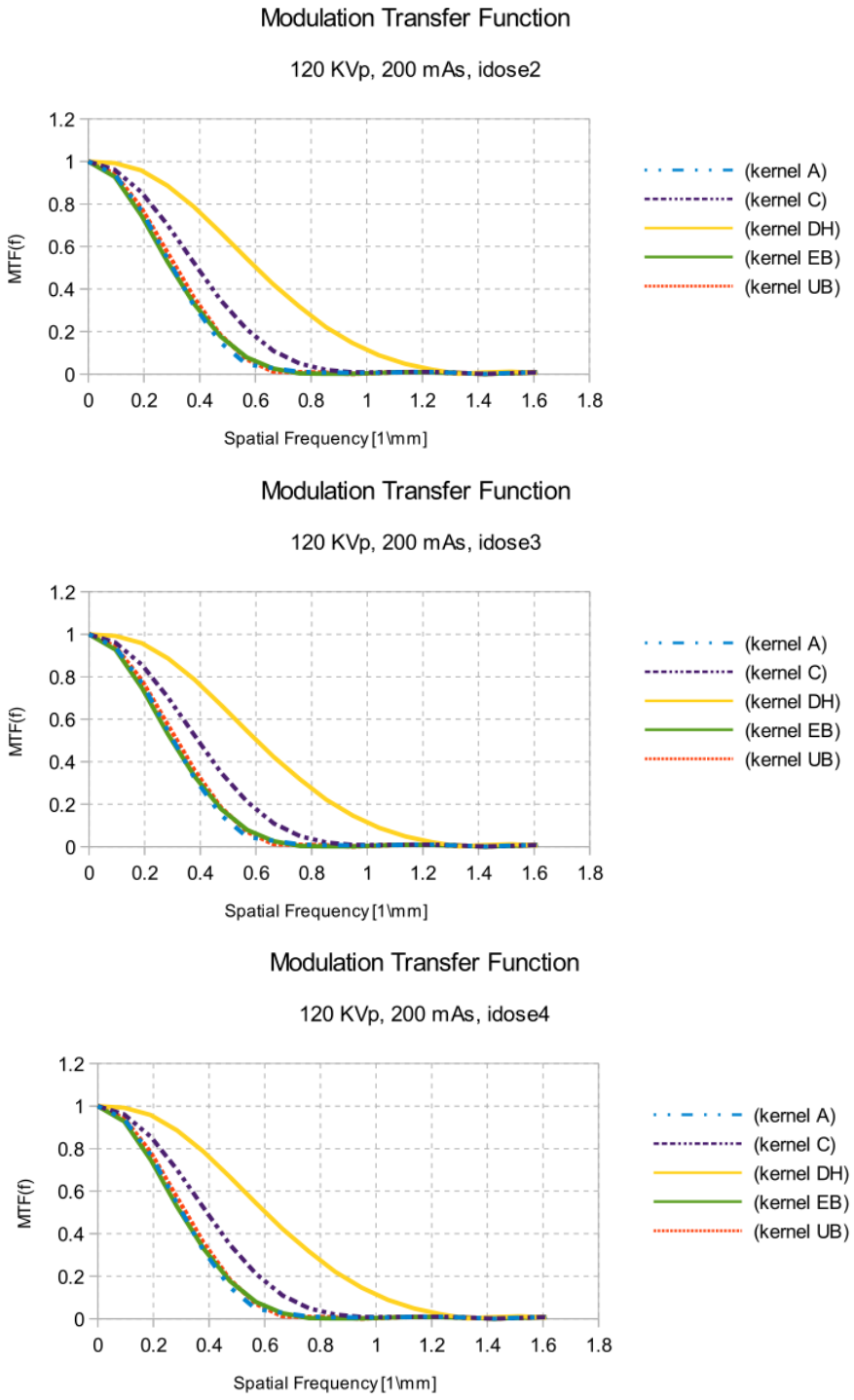

Figure 3.33: MTF for level 2, level 3 and level 4 of iterative reconstruction algorithm.

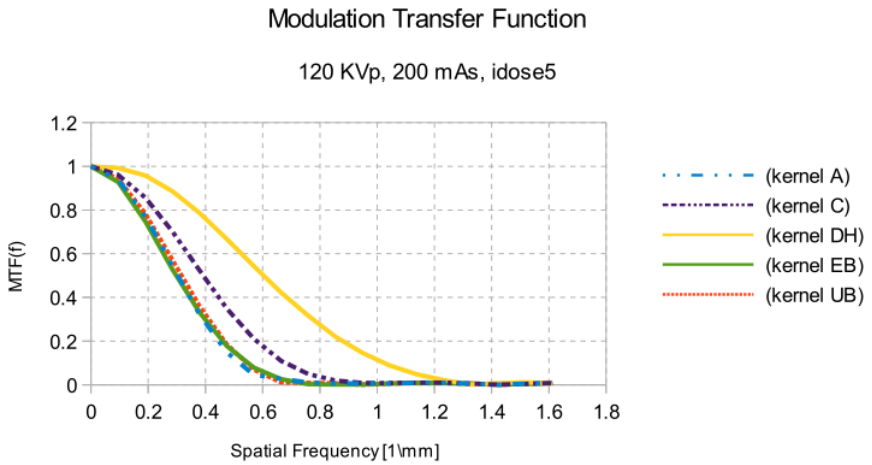

Figure 3.34: MTF for level 5 of iterative reconstruction algorithm.

The iterative reconstructions are identical to the Filtered Back Projection. Fig.[3.32-3.34] illustrate the results of the MTF calculation with the phantom. The five curves are very similar in shape and position. The iDose algorithm does not decrease the spatial resolution. This is an important observation, because in this case the iDose algorithm reduces noise (as seen previously), whereas the spatial resolution is maintained. Then, a key component of the iDose^4 algorithm, is the preservation of the spatial resolution among the different strengths (levels).

The above results can be summarized as follows: high MTF values in the low frequency range is needed to outline the coarse details of the image and are important for presentation and detection of relatively large but low contrast lesions. Consequently increased MTF values in the high frequency range are necessary to portray fine details and sharp edges. This is of obvious importance for small objects but also sometimes for larger objects due to the importance of edges and sharp borders for detection of low contrast objects and for accurate assessment of their size and shape.

The final analysis of this chapter is to assess the values of $MTF_{50\%}$, $MTF_{10\%}$ and standard deviation (in HU) of FBP and iterative reconstruction algorithm, thous to observe what kind of pattern has the variation of the modulation transfer function.

All MTF data was averaged into 0.05 mm^{-1} bins as per IEC specification to facilitate a comparison of the data, as shown in[39].

	FBP		
	$MTF_{10\%}$	$MTF_{50\%}$	SD[HU]
kernel A	0.5	0.3	43.4
kernel UB	0.5	0.3	46.7
kernel EB	0.5	0.2	47.6
kernel C	0.6	0.3	57.3
kernel DH	1.0	0.5	137.1

Table 3.4: Values of MTF at 10%, 50% and standard deviation (noise) of filtered back projection for all convolution kernels.

	iDose1		
	$MTF_{10\%}$	$MTF_{50\%}$	SD[HU]
kernel A	0.5	0.3	43.4
kernel UB	0.5	0.3	46.7
kernel EB	0.5	0.2	47.6
kernel C	0.6	0.3	57.3
kernel DH	1.0	0.5	137.0

Table 3.5: Values of MTF at 10%, 50% and standard deviation (noise) of idose level 1 for all convolution kernels.

	iDose5		
	$MTF_{10\%}$	$MTF_{50\%}$	SD[HU]
kernel A	0.5	0.3	43.4
kernel UB	0.5	0.3	46.7
kernel EB	0.5	0.2	47.6
kernel C	0.6	0.3	57.3
kernel DH	1.0	0.5	136.9

Table 3.6: Values of MTF at 10%, 50% and standard deviation (noise) of idose level 5 for all convolution kernels.

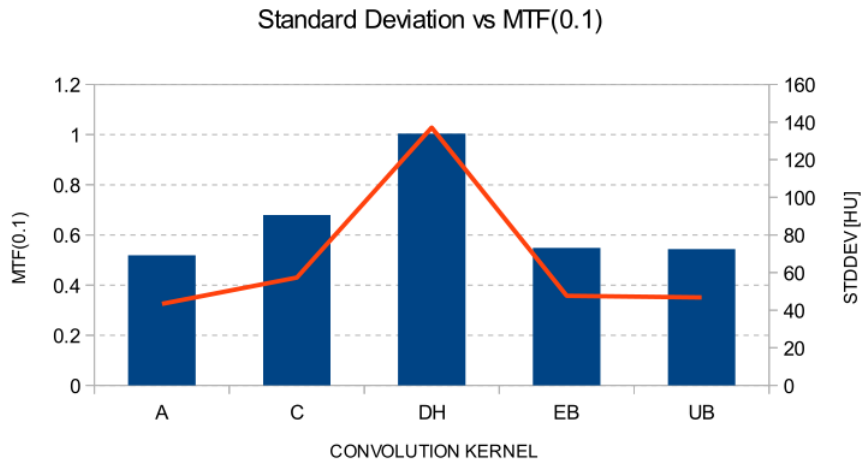

Figure 3.35: Modulation transfer function at 10% compared standard deviation for all convolution kernels. The filter DH has a value greater than other.

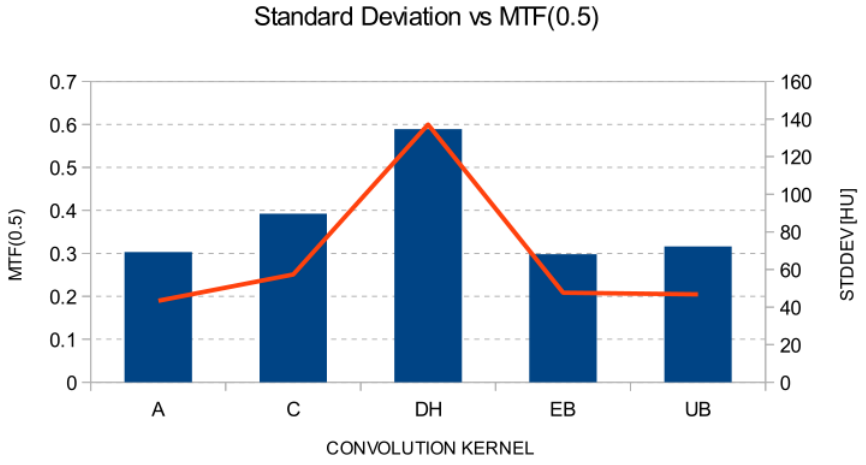

Figure 3.36: Modulation transfer function at 50% compared standard deviation for all convolution kernels. The filter DH has a greater value than other.

Chapter 4

Low-Contrast Detectability

The low contrast detectability (LCD) represents the ability of CT scanner to distinguish between objects that have similar x-ray attenuation coefficients. In cases of other diagnostic imaging modalities it means the ability of imaging equipment to differentiate between objects that have similar properties. LCD is one of the important performance parameters for Computed Tomography (CT). Often LCD is determined by visual inspection of low contrast phantom images. The testing process is gated not only by limitations of existing LCD phantoms, but also by the subjective nature of the evaluation methodology[41].

In general, LCD aims to describe the performance of a CT system in detecting objects of low contrast against the background. Ideally, one would define an objective test method, for example, using phantoms, to assess LCD for scanner characterization. In current practice, LCD is typically specified by measuring a low contrast phantom with objects of different sizes and different densities.

The crux lies in the presumed ability to see a certain low contrast structure, since for an individual this is a highly subjective task. It makes difficult to obtain statistically objective data with some level of confidence using visual methods.

4.1 Catphan 600 phantom

Our study is based on images acquired with the Catphan 600 phantom (The Phantom Laboratory Incorporated, Salem, NY). The phantom, cylindrical in shape, is constructed of PMMA and consists of 5 modules designed to perform various quality tests in tomographic images. The phantom long axis (z-axis) has to be placed longitudinal to the CT table, the modules are in

transverse planes to the phantom z-axis (x-y plane).

The Catphan 600 phantom has multiple test modules for assessing various image quality parameters. Low contrast detectability was measured using the CTP515 low contrast module. The ability to distinguish between the object and the background is limited by object size and image noise.

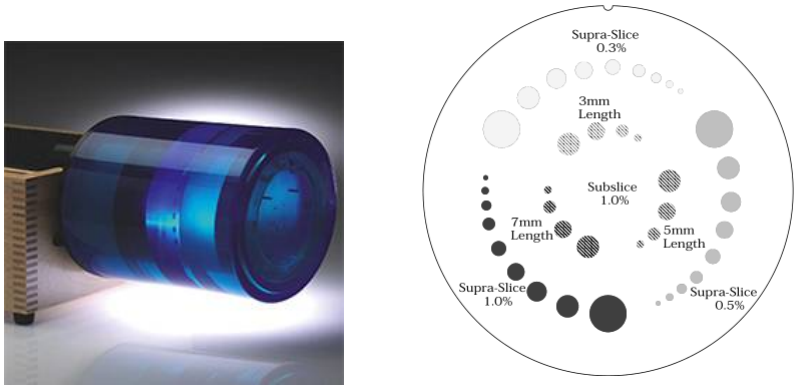

Figure 4.1: Catphan 600 phantom (LEFT). CTP515 low contrast module with supra-slice and subslice contrast targets (RIGHT).

Supra-slice targets have diameters from 2.0mm to 15.0mm. Subslice targets have diameters fro 3.0mm to 9.0mm. In low contrast resolution module we can find three areas with different nominal contrast levels: 1%, 0.5% and 0.3% (supra-slice targets). All of the targets in each contrast group are cast from a single mix to assure that the contrast levels will be the same for all targets.

Along with the supra-slice (targets with z axis dimension longer than most maximum slice width) the CTP515 low contrast module includes subslice targets (targets with z axis length smaller than some of the usual slice width). The subslice targets are arranged in the inner circle of tests in the module. The subslice targets are cast from the same mix as the 1.0% supra-slice targets. Because they are from the same mix in the evaluation of the actual subslice target contrast the supra-slice targets can be used to establish contrast values. The subslice targets have z axis lengths of 3, 5, and 7 mm and diameters of 3, 5, 7, and 9 mm. The evaluation of subslice target readability is helpful in understanding the scanner's different spiral imaging settings and how the settings will affect the ability to visualize small objects with low contrasts from their background.

4.1.1 Contrast to noise ratio with Catphan 600

Low-contrast resolution was assessed in two steps using the low-contrast module of the phantom Fig.[4.2]. The module contains three sets of outer supraslice cylinders, with a z-axis dimension of 40 mm, which according to the manufacturer have a nominal contrast of 1%, 0.5% and 0.3%. Objective assessment was done by measuring the CT numbers (HU) within the ROI and in the background selected, the noise was measured as the standard deviation within the same region of interest (ROI) of background selected previously. Contrast-to-noise ratios (CNRs) were calculated using the formula:

$$CNR = \frac{HU_{object} - HU_{background}}{\sigma_{background}} \tag{4.1}$$

where HU_{object} is the average pixel value of the low contrast object in a $15mm$ diameter region of interest, $HU_{back.}$ is the average pixel value of the background region of interest and σ is the standard deviation of the attenuation values of the background (in HU). The parameter $\sigma_{back.}$ not only includes photon statistics and electronic noise in the results but also structural noise than can obscure the object.

The CNR is a useful metric for describing the signal amplitude relative to the ambient noise for simple and largely homogeneous objects. However, the CNR depends only on contrast and noise. Actual signal detectability also depends on factors including signal size, shape, and density distribution; background level, variability, and correlation; the variance and covariance of measurement noise; spatial resolution; and the observer and detection strategy used. The CNR can be useful in some simple situations, e.g., determining thresholds of contrast agents at which signals on a test phantom become visible.

Since the target contrasts are nominal, the actual target contrasts need to be determined before testing specific contrast performance specifications. The limiting detectability should be measured with the reconstruction algorithm of the scanner which is routinely used, as well as other clinically relevant reconstruction algorithms. The baseline performance level must be stated for a given phantom at specific scan conditions, including radiation dose, viewing conditions, and visualization criteria. It should be noted that this visual test for establishing LCD is subjective since it depends on a number of factors including the visual acuity of the observers and ambient lightning conditions.

The next table shows the acquisition and reconstruction parameters for the CNR analysis.

Voltage	120 kVp
Exposure	300 mAs
Beam Collimation	64×0.625
Convolution Kernel	A, EB, UB, C
Slice Thickness	5 mm
Pixel Sixe	0.4901×0.4901 mm
FOV	250×250 mm
Rotation Time	0.75 s

Table 4.1: List of parameters utilized.

The actual contrast levels are measured by making region of interest measurements over the three larger targets, for all contrast and in the local background area. To determine actual contrast levels, average the measurements made from several scans. For this study we use the first five reconstruction slice using kernel A, EB, UB and C (both standard and iterative algorithm).

It is important to measure the background area adjacent to the measured target because "cupping" and "capping" effects cause variation of CT numbers from one scan region to another. Position the region of interest to avoid the target edges. The region of interest should be at least 4×4 pixels in diameter.

Because low contrast measurements are "noisy" it is advisable to calculate the average of the multiple measurements made from several scans. Carefully monitor the mAs setting because the photon flux will improve with increased x-ray exposure. Use the size of the targets visualized under various noise levels to estimate information on contrast to noise ratio.

Although decreasing tube current is the most means of reducing CT radiation dose, this alteration also reduces the contrast-to-noise ratio, which may affect the diagnostic outcome of the examination. This is especially true in abdominal studies, where the low-contrast area are severely affected by CNR. Some studies suggest that scanning with low tube voltage is possible to reduce dose without markedly affecting image quality; however, there are few reports on the effect of low tube voltage on abdominal image quality and low-contrast detectability[42][43][44].

We selected only the first big target ($15mm$) for all nominal contrasts. This is because the other smaller targets are very difficult to study on a conventional displays (contrast and resolution limited). All measurements were made using the same region of interest (ROI), stored using imageJ software with reconstruct image sets using $5mm$ slice thickness.

First and foremost we have done a window-level to improve the image display and to perform all measurements correctly. Subsequently, the measurements were made using the slice centered on the image plane and the mean values of the object and background are acquired obtaining the contrast to noise ratio. The same method was applied to all reconstructed images with all convolution kernels.

Then, the software allowed to store a circular ROI, accordingly obtain the values used for the calculation of CNR, this for all analyzed kernels and for each phantom insert $(0.3\%, 0.5\%, 1\%)$. The procedure and the analysis are shown in Fig.[4.2-4.5-4.8].

$$\boxed{CNR \Longrightarrow Nominal\ Contrast\ 1\%.}$$

The detectability of detail increases with object size and/or contrast between object and background. For example, the detectability of objects with the same contrast will increase in line with the object size. Similarly, when object size is maintained, detectability will increase with increasing contrast. Hence, small objects can have higher contrast than larger objects for the same detectability.

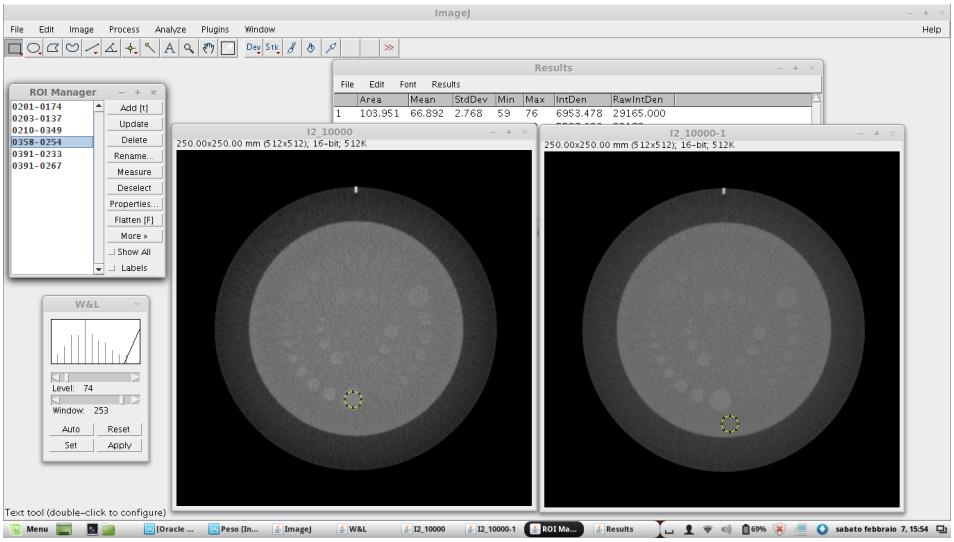

Figure 4.2: Catphan phantom analysis using nominal contrast of 1%.

The CNR was obtained by subtracting the mean CT number measured in the $15mm$ diameter object from the mean CT number measured nearby (phantom background) and by dividing the result by the standard deviation of the pixel values of the phantom background.

The region of interest used to perform the measurements was slightly smaller than the $15mm$ diameter of the object in order to include only it in the measurements. The measurement was repeated for filtered back projection and iterative algorithm (for the first five reconstruction levels).

Remembering that, the larger the CNR, the less noise is viewed on an image and the quality is improved; we can summarize the results shown in the table below as follows: looking at this data, the images with the highest CNR are, for all convolution kernels, those using the iterative algorithm with the highest level of reconstruction.

The convolution kernel A has CNR higher than the others, which means that its use allows us to obtain images (and therefore reconstructions) with better contrast for the same pin with nominal contrast of 1%.

	Nominal contrast 1%			
	Kernel A	Kernel UB	Kernel EB	Kernel C
FBP	6.2± 0.2	4.6± 0.3	4.5± 0.3	3.6± 0.3
idose 1	6.4± 0.2	4.8± 0.3	4.9± 0.3	4.0± 0.2
idose 2	7.6± 0.2	5.3± 0.3	5.3± 0.3	4.2± 0.2
idose 3	8.1± 0.2	5.7± 0.2	5.7± 0.2	4.5± 0.2
idose 4	8.6± 0.1	6.1± 0.2	6.1± 0.2	4.9± 0.1
idose 5	9.4± 0.1	6.6± 0.1	6.7± 0.1	5.5± 0.1

Table 4.2: CNR values both standard and iterative reconstruction; nominal contrast 1%.

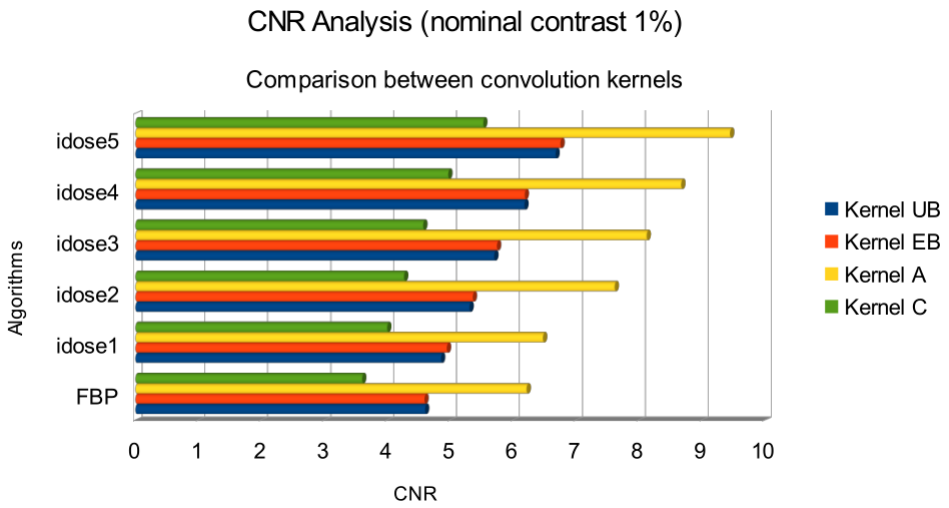

Figure 4.3: Contrast to noise ratio for iterative and standard algorithm. We can see the differences between the values; they are very similar between kernel UB and EB.

Fig.[4.3] shows the variations of the CNR, compared to the different iterative levels used. The images which show the greatest amount of noise are the images with the lowest CNR, which are those related to the convolution kernel C (i.e. sharp filter). This data also reflects the results seen in the low contrast detectability exam, where only a few targets are visible with images that have low CNR.

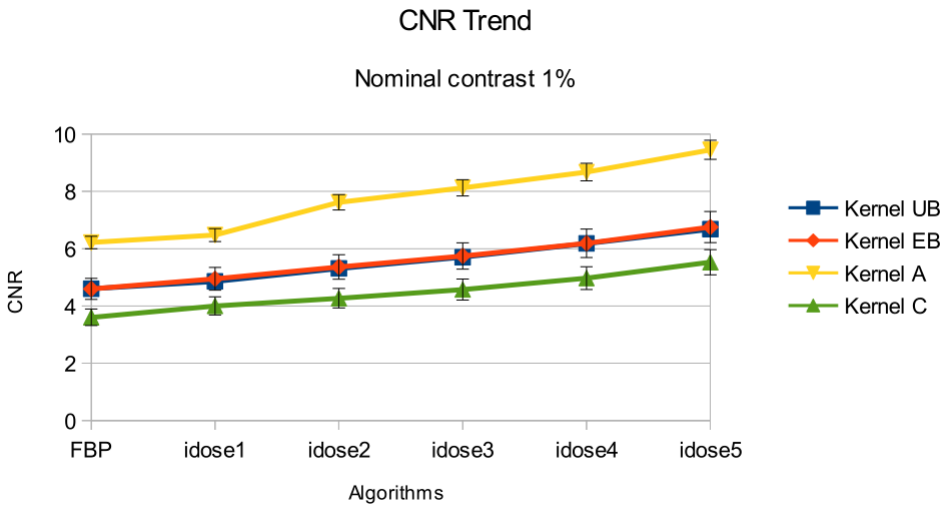

Figure 4.4: Trends of contrast to noise ratio at varying levels of reconstruction.

Fig.[4.4] shows the trend of the various filters by varying the algorithm and its levels of reconstruction. We observe that filter A does not vary much, however it rises between iterative level 1 and level 2; while tends to have a linear trend from the second level onwards.

UB and EB filters overlap, then they give the same contrast variation using Filtered Back Projection and iterative algorithm. These two filters have, in fact, very similar features; the only thing that distinguishes them is the type of acquisition, axial for UB and helical for EB.

The filter C instead has the lowest value of CNR; this is because, being a moderate sharp filter, allows the noise to affect more the image. In this way the calculated contrast will be lower than the previous filters.

$$\boxed{CNR \Longrightarrow Nominal\ Contrast\ 0.5\%}$$

Low contrast objects with a high noise level will generate a low CNR value which results in reduced visibility of the object as marked in the yellow ROI. CNR plays a certain role when it comes to detecting objects of inherent

low contrast. With high inherent contrast, the object is clearly visible also with a high noise level.

The samples and the background material have equivalent effective atomic numbers. Only the densities is varied to produce changes in effective attenuation coefficients.

Unlike previous measures, the ROI was placed on the medium low contrast object and mean CT number was recorded. In addition a ROI with the same size was selected from the background and mean CT number values and SD were stored. The CNR values were calculated according to the equation (4.1).

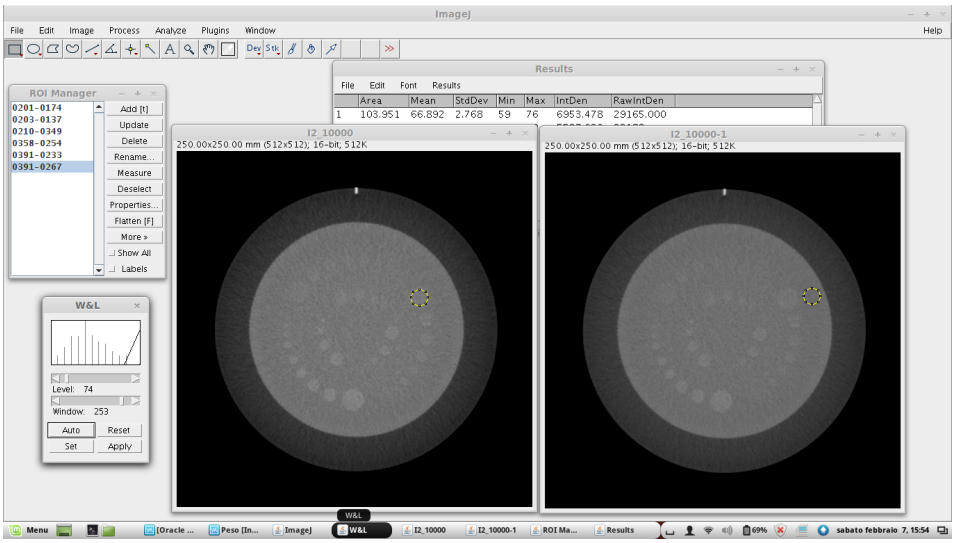

Figure 4.5: Catphan phantom analysis using nominal contrast of 0.5%.

	Nominal contrast 0.5%			
	Kernel A	Kernel UB	Kernel EB	Kernel C
FBP	4.5± 0.3	2.6± 0.3	2.5± 0.3	2.4± 0.3
idose 1	4.8± 0.2	2.7± 0.3	2.7± 0.3	2.7± 0.3
idose 2	5.4± 0.2	3.0± 0.2	2.9± 0.2	2.9± 0.2
idose 3	5.8± 0.2	3.2± 0.2	3.1± 0.2	3.1± 0.2
idose 4	6.3± 0.2	3.4± 0.2	3.3± 0.2	3.4± 0.2
idose 5	7.0± 0.1	3.8± 0.2	3.5± 0.2	3.7± 0.1

Table 4.3: CNR values both standard and iterative reconstruction; nominal contrast 0.5%.

The table 4.3 shows the values obtained using a pin with nominal contrast 0.5%. Even here, values of CNR increase with the use of iterative algorithm;

however, the values are generally lower than those obtained previously for all convolution kernels.

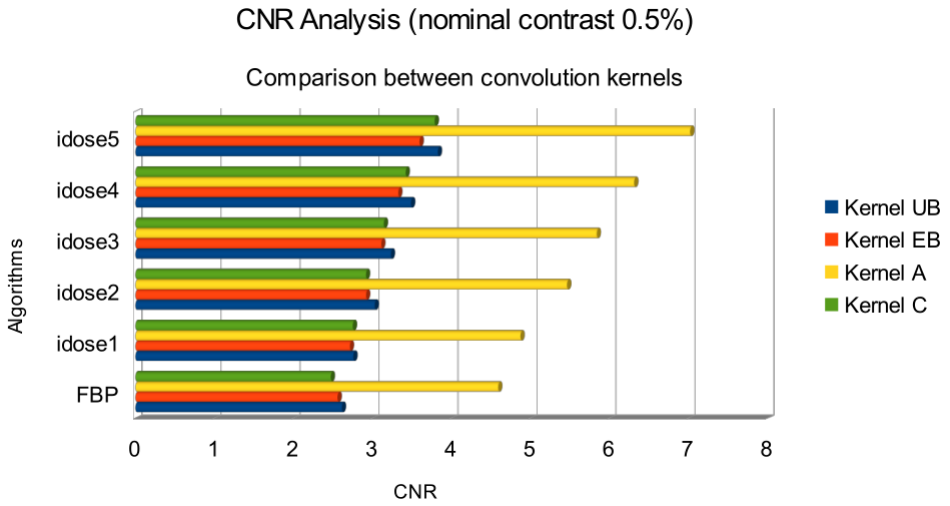

Figure 4.6: Contrast to noise ratio for iterative and standard algorithm. We can see the small differences between the filter C and EB.

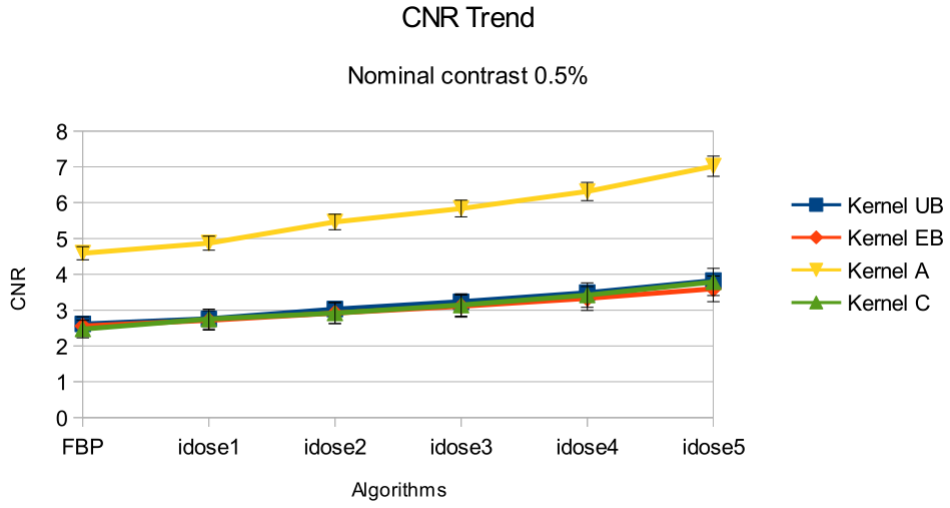

Figure 4.7: Trends of contrast to noise ratio at varying levels of reconstruction.

Fig.[4.6] shows that for filter A the variation between FBP and level 5 of iDose is greater than the other filters. This means that the iterative algorithm allows to reconstruct the image with better contrast.

For filter C we immediately noticed that for standard reconstruction the value of CNR is lower than filter EB; while for the first iterative level, the CNR is almost equal. Instead, for higher levels of reconstruction its values are even higher (the latter compared with the filter EB). The other values of CNR have a performance similar to the case designed for the pin with nominal contrast 1%.

Fig.[4.7] allows to observe how the CNR varies depending on the levels of reconstruction. Unlike the previous case, UB, EB and C filters behave in a different way: all three trends are superimposed, especially for the first three levels of iDose^4. Instead as regards the filtered back projection, there is a slight difference in the values for filter C; while in the case of the pin with nominal contrast 1% variability was more pronounced.

The last two levels of reconstruction show different features. The CNR for the filter EB has an even lower value (even if slightly) compared to the sharp filter and standard filter, which is not observed in the case discussed previously.

$$\boxed{CNR \Longrightarrow Nominal\ Contrast\ 0.3\%}$$

Also in this case, the procedure for the calculation of the CNR is similar to that used in the two previous cases. We made sure to select the region correctly, given the very low visibility. The target chosen is the biggest one with the lowest nominal contrast. The results showed that increasing level of iDose^4 improved the low contrast resolution.

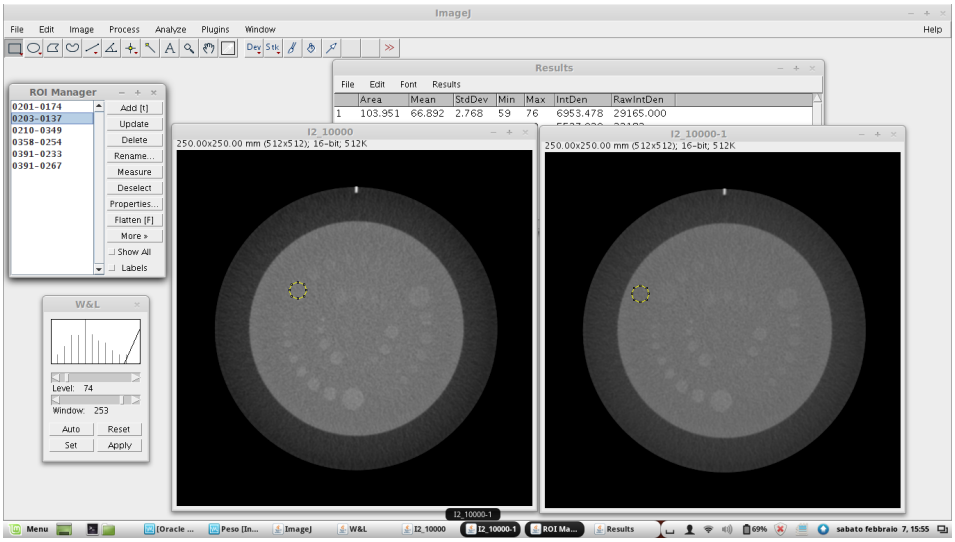

Figure 4.8: Catphan phantom analysis using nominal contrast of 0.3%.

In this case, from the carried analysis, the variations of the CNR can be observed, compared to the previous analysis. For the filtered back projection, the difference with level 5 of iDose is less marked than nominal contrasts 1% and 0.5%. All filters have low values, this in agreement with the fact of having considered the pins with lower contrast, thus more difficult to detect.

In the filter A there is a greater variation, this is because the iterative algorithm influence to a greater extent the smooth filter. Instead, the filters EB and UB have almost the same values, instead the filter C has values even higher. We will immediately notice the difference in the values of this filter, via the analysis made in the case of the nominal contrast 0.5%.

	Nominal contrast 0.3%			
	Kernel A	Kernel UB	Kernel EB	Kernel C
FBP	2.9± 0.3	1.6± 0.2	1.6± 0.2	1.7± 0.2
idose 1	3.0± 0.3	1.7± 0.2	1.7± 0.2	1.9± 0.2
idose 2	3.6± 0.2	1.9± 0.2	1.9± 0.2	2.0± 0.2
idose 3	3.9± 0.2	2.0± 0.2	2.0± 0.2	2.1± 0.1
idose 4	4.1± 0.2	2.2± 0.1	2.2± 0.1	2.3± 0.1
idose 5	4.4± 0.1	2.4± 0.1	2.3± 0.1	2.5± 0.1

Table 4.4: CNR values both standard and iterative reconstruction; nominal contrast 0.3%.

Fig.[4.9] shows the values of the contrast-to-noise ratio at varying levels of reconstruction. Also here, the filter A is one that has the highest contrast (both standard and iterative algorithm), for the same considered pins.

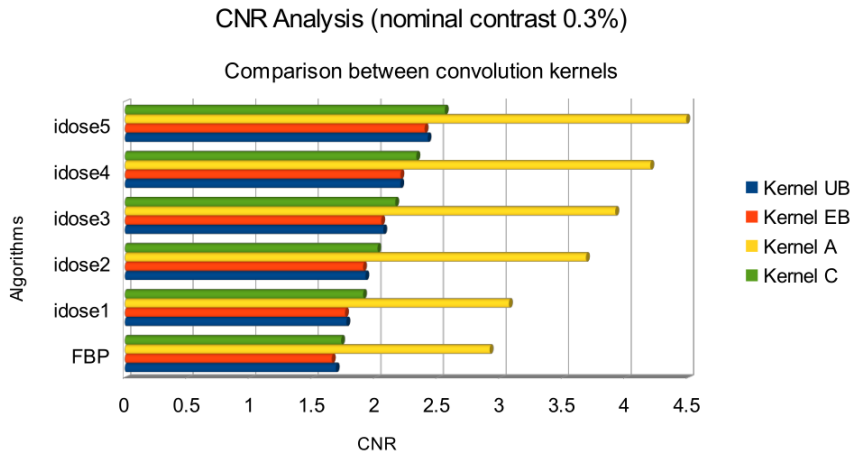

Figure 4.9: Contrast to noise ratio for iterative and standard algorithm. We can see the differences between the filters C, EB and UB.

Instead, what we see is that the other filters have almost similar values, and filter C has even higher values than standard filters (EB and UB).

The figure below describes the trends of the CNR, from filtered back projection to level 5 of iterative reconstruction. The trend of the smooth filter is very similar to the previous one, while the others tend to have the same variation of the CNR. But here we have a peculiarity: the sharp filter has a value very close to the one of standard filters UB and EB, for FBP. While for all iDose levels, this filter has higher values than the other two filters. This feature is found only by analyzing the low contrast referred to pin with nominal contrast 0.3%.

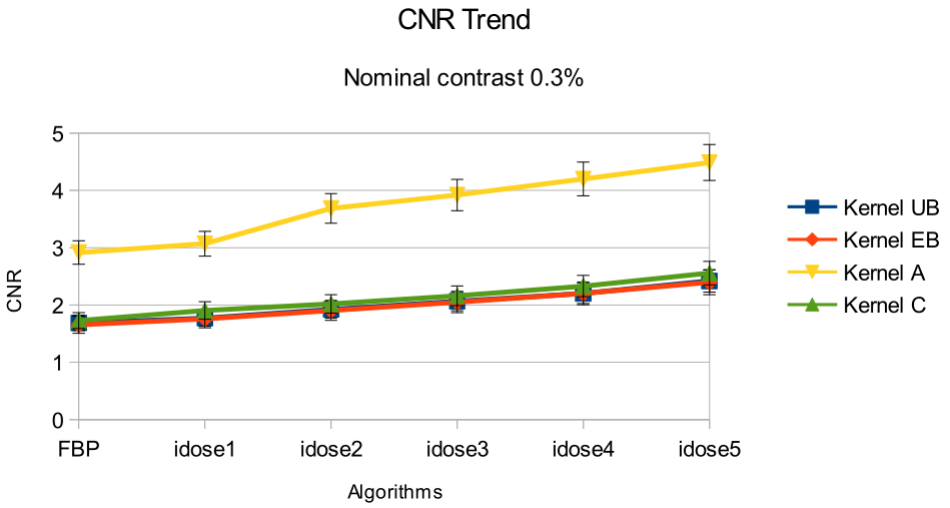

Figure 4.10: Trends of contrast to noise ratio at varying levels of reconstruction.

4.1.2 CIRS 061 phantom

The CIRS Helical CT Phantom is designed to test scanning protocols to verify that small, low contrast lesions will be detected. The phantom permits complete testing of low contrast lesion detection when scan parameters are varied. These parameters include collimation, pitch, reconstructed field of view, reconstruction algorithms, z-axis interpolators, kVp, mA and rotation time. Testing can be applied to protocols designed for head and abdomen. The phantom is manufactured from a proprietary epoxy material which accurately mimics liver tissue.

The CT Lesion Detectability Phantom is particularly useful to physicians, CT technologists, and medical physicists who design scanning protocols for abdominal, pelvic, and brain CT. It allows users to test various scanning

protocols to verify that small low contrast lesions will be detected. This is the only way to be sure that a CT scanner is "seeing" tumors that are known to be present. The use of this phantom removes many doubt as to the limit of low contrast spherical lesion detectability for various scan protocols, it is used for 3D analysis. This lesion detectability testing can be applied to protocols designed for imaging of the liver, spleen, pancreas, kidneys, and adrenal glands. It can also be used for mass detection in the brain.

The CT lesion detectability Phantom is a tissue-equivalent test object that consists of an 18 cm diameter right circular cylinder with a CT value of 50 HU at 120 kVp. Within the phantom is an 18 cm diameter, 4 cm deep right circular void in which a soft-tissue equivalent disk (containing low contrast spheres) can be placed. The cylindrical void is in a plane containing the z-axis of the scanner. The soft-tissue-equivalent disk also has a background CT value of 50 HU. Embedded within the disk are three sets of simulated spherical lesions.

There are three rows of spherical targets that are 5, 10 and 20 HU below the liver equivalent background matrix. This phantoms is designed to assist technical and clinical staffs in the selection of optimal spiral/helical scanning parameters.

One set is 5 HU below background, a second set is 10 HU below background, and the last set is 20 HU below background. Each set contains one sphere each of the following diameters: 2.4, 3.2, 4.0, 4.8, 6.3 and 9.5 *mm*. These diameters were chosen to encompass the full range of clinically significant lesions. The disk can also be placed at the end of the phantom when axial scanning detectability testing is desired.

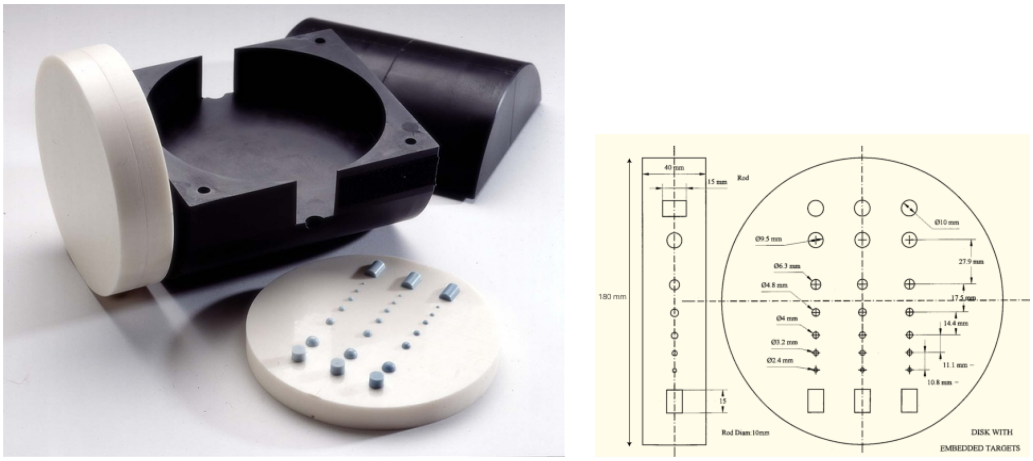

Figure 4.11: Spiral CIRS phantom, internal view (LEFT). Phantom contains spherical objects; these spheres are placed in three rows. Each row contains spheres that were originally designed to be 20, 10, and 5 HU below background (designed to equal liver; no attenuation given (RIGHT).

4.1.3 Contrast to noise ratio with CIRS 061

The phantom body serves a dual purpose. One, it enables the test disk to be positioned parallel to the CT couch in the z-axis without artifacts and with appropriate surrounding attenuation. Two, it can be used as a support device to position the test disk at 90 degrees to the CT couch in the x, y axis. The testing disk has exterior markings to enable location and orientation of the embedded targets. The disk has a scribe line which indicates the midline of the test disk and the targets. The disk is also marked top, left and right to correspond with the Fig.[4.11].

The main features for this phantom are:

- Incorporates clinically-relevant lesion shape (spherical) and size.
- Provides clinically-relevant absolute HU values for soft tissue.
- Provides a clinically-relevant HU differential (i.e. tumors have a slightly lower HU than backround).
- Designed for use on all conventional and spiral (helical) CT scanners.
- Valid for x-ray energies from 80 to 140 kVp.
- Background Hounsfield Units (HU) approximate liver tissue.

Next table shows the acquisition and reconstruction parameters for the CNR analysis.

Voltage	120 kVp
Exposure	300 mAs
Beam Collimation	64×0.625
Convolution Kernel	A, B, C
Slice Thickness	5 mm
Pixel Sixe	0.4901×0.4901 mm
FOV	250×250 mm
Rotation Time	0.75 s
Pitch	1.067

Table 4.5: List of parameters utilized.

In the abdomen, the most significant challenge related to low dose is low-contrast object detection, especially in the liver, where neoplastic disease is commonly manifest as a low-attenuation object within a background of

slightly higher attenuation normal liver. Thus, any dose-reduction strategy must address and maintain low-contrast object detection.

In this case, since the targets are below the liver equivalent background matrix, the equation to calculate the contrast-noise ratio can be written as:

$$CNR = \left| \frac{HU_{object} - HU_{background}}{\sigma_{background}} \right| \tag{4.2}$$

Now, we proceed in a similar manner to the case of Catphan phantom. The only difference will be the nominal contrast analyzed.

$$\boxed{CNR \Longrightarrow Nominal\ Contrast\ 2\%}$$

A low-contrast phantom (CIRS Helical CT Phantom, Computerized Imaging Reference Systems), composed of three rows of cylinders was scanned. The raw data were reconstructed using FBP and iDose^4 with kernel A, B and C. All reconstructions were performed using the same size FOV at the same table position.

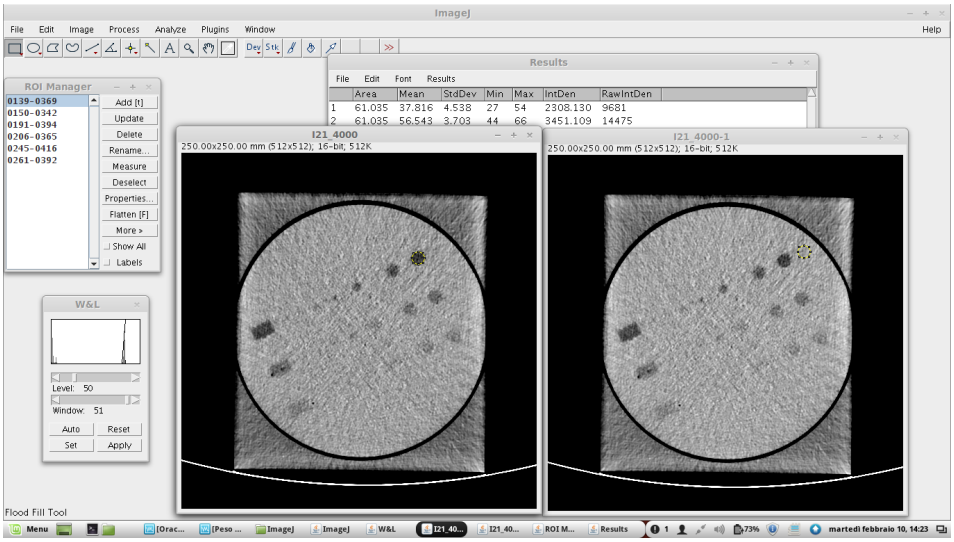

Figure 4.12: Cirs 061 phantom analysis using nominal contrast 2%.

In the phantom, by using imageJ software, same size regions of interest (ROIs) in the same position and belonging to the same slice were placed on the large cylinder, and the adjacent background used is the one belonging to the right of the sphere. The contrast was calculated as the difference between the mean CT numbers of the ROI from the low contrast cylinder and the phantom background. The noise was the SD of the CT numbers inside the

ROI of the phantom background. Then, the CNR was calculated using (4.2) and the results are shown in the next table.

	Nominal contrast 2%		
	Kernel A	Kernel B	Kernel C
FBP	5.8± 0.4	3.4± 0.3	2.2± 0.2
idose 1	6.5± 0.4	3.8± 0.3	3.3± 0.2
idose 2	7.2± 0.4	4.1± 0.3	3.5± 0.2
idose 3	7.7± 0.3	4.3± 0.2	3.8± 0.1
idose 4	8.5± 0.3	4.7± 0.2	4.2± 0.1
idose 5	9.6± 0.3	5.2± 0.1	4.7± 0.1

Table 4.6: CNR values both standard and iterative reconstruction; nominal contrast 2%.

These values reflect the assessment made for the other phantom. Here too, the filter A gives a greater value than other filters. Even, the FBP is almost half of the level 5 of iDose[4] (for smooth filter) and less than half respect to sharp filter. This is due to the fact that, probably, the nominal contrast is different from Catphan 600, furthermore, Hounsfield unit varies significantly between the pin and background.

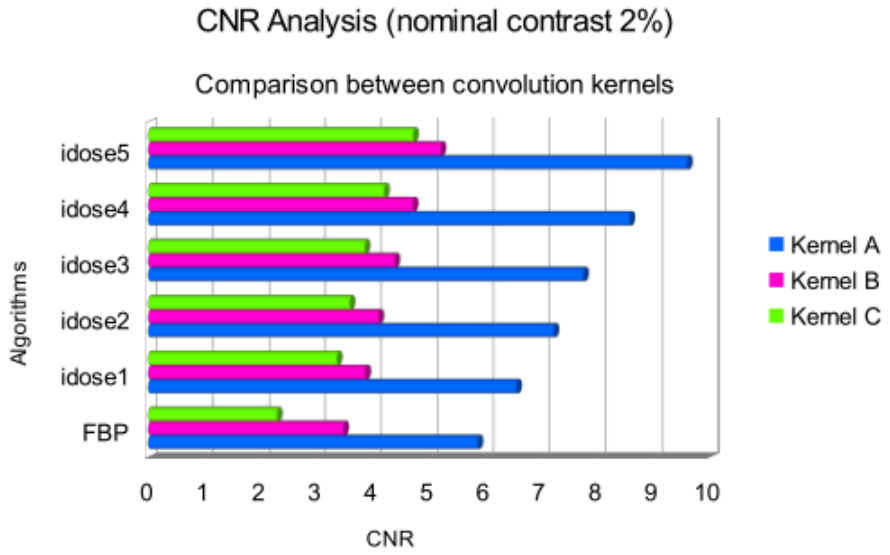

Figure 4.13: Contrast to noise ratio for iterative and standard algorithm.

Next figure shows the curves obtained using kernel A, B and C. The smooth filter has a values larger than other two, then maintains the characteristic of being a filter that improves the contrast resolution. Instead,

kernels B and C have very similar values, except in the range between FBP and level 1 of iterative algorithm.

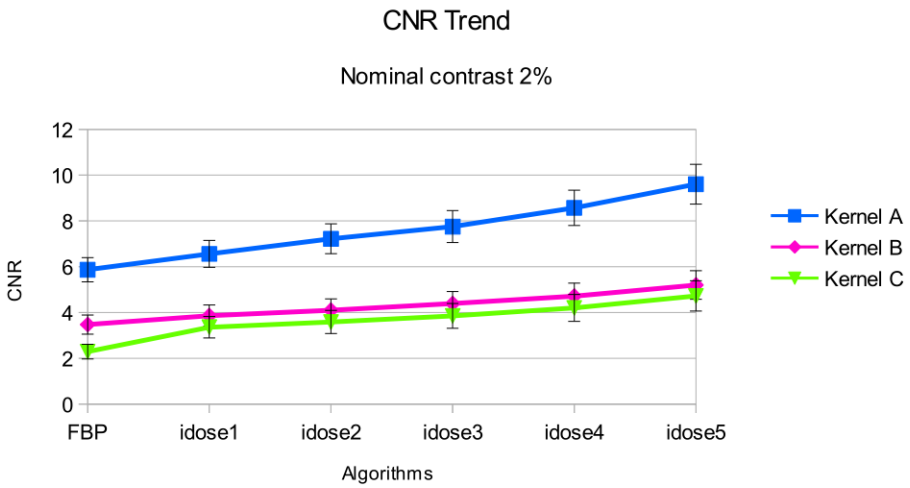

Figure 4.14: Trends of contrast to noise ratio at varying levels of reconstruction.

$$\boxed{CNR \Longrightarrow \textit{Nominal Contrast } 1\%}$$

Next analysis leads us to consider the pin with nominal contrast of 10 HU (1%). For the phantom that we are considering, for each object imaged below background attenuation (10 HU), there is an observation at low contrast cylinder both in FBP and iDose[4].

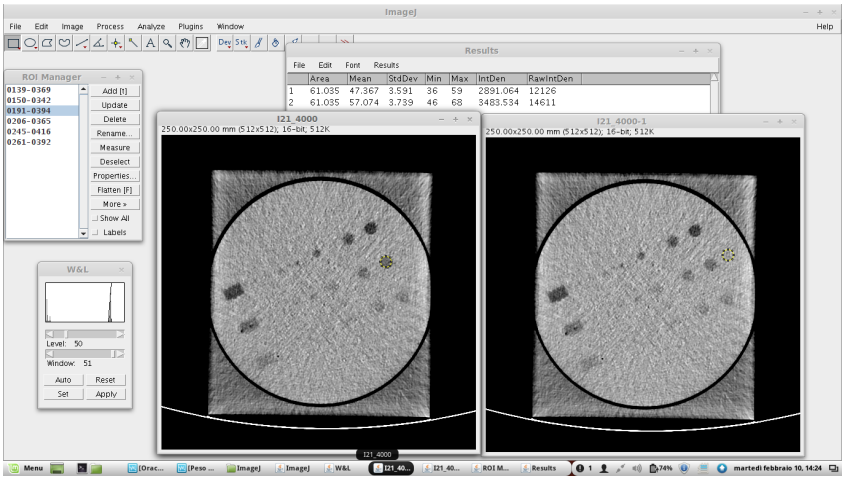

Figure 4.15: Cirs 061 phantom analysis using nominal contrast 1%.

The simulated lesions usually have fixed location and are framed by surrounding structures, which are often more conspicuous than the lesions of interest. The routine use of thinner collimation with MSCT has resulted in more frequent detection of very small lesions, and the detection and characterization of small lesions can be important for patients with history of malignancy[47]. Now, we repeat the same procedure by positioning the ROI above the cylinder.

	Nominal contrast 1%		
	Kernel A	Kernel B	Kernel C
FBP	2.7± 0.3	1.9± 0.2	1.6± 0.2
idose 1	2.9± 0.3	2.1± 0.2	1.8± 0.2
idose 2	3.1± 0.3	2.2± 0.2	1.9± 0.2
idose 3	3.3± 0.2	2.4± 0.2	2.0± 0.1
idose 4	3.7± 0.2	2.5± 0.2	2.2± 0.1
idose 5	4.0± 0.2	2.8± 0.1	2.4± 0.1

Table 4.7: CNR values both standard and iterative reconstruction; nominal contrast 1%.

The table above shows the values obtained by using pin (lesions) with density 10 HU lower than that of the background; nevertheless, while lesions with great difference in density or with higher density to background might present different results, a difference in the density of 10 HU represents the minimum lesion to liver contrast necessary for detection.

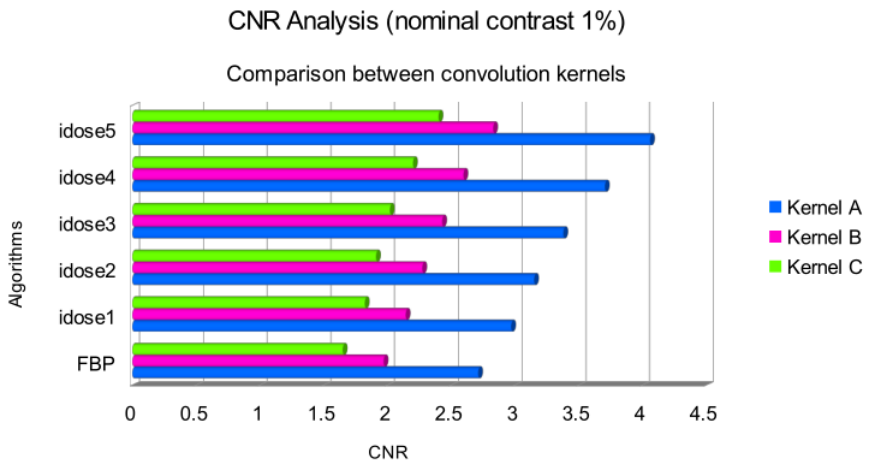

Figure 4.16: Contrast to noise ratio for iterative and standard algorithm.

Here, we note a small differences between nominal contrast 2% and nominal contrast 1%.

In the nominal contrast of 2%, kernels B and C have a variation in the CNR higher than nominal contrast of 1%. For Filtered Back Projection the range of variation is 1.2, while for iterative reconstruction is 0.5 (level 5). In the nominal contrast 1%, the range is 0.3 (FBP) and 0.4 (iDose, level 5).

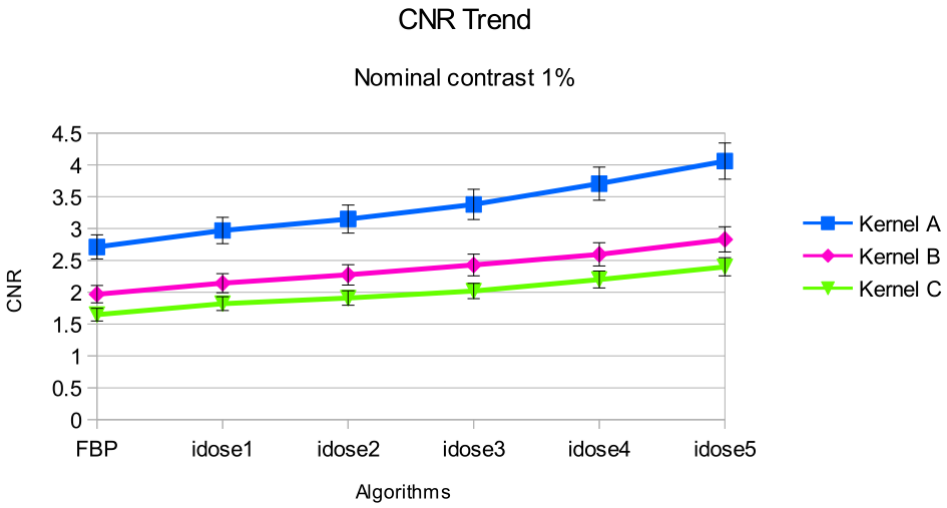

Figure 4.17: Trends of contrast to noise ratio at varying levels of reconstruction.

$$\boxed{CNR \Longrightarrow Nominal\ Contrast\ 0.5\%}$$

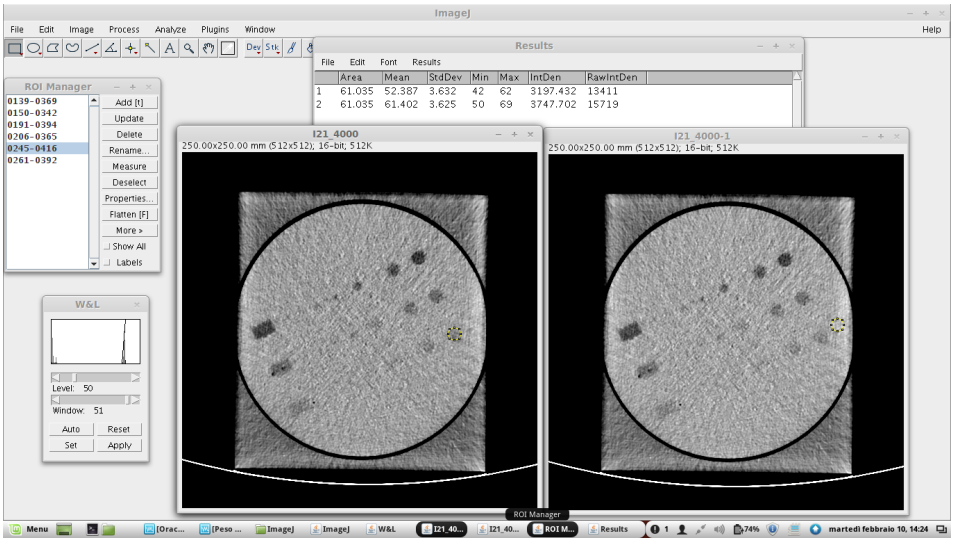

Figure 4.18: Cirs 061 phantom analysis using nominal contrast 0.5%.

Last analysis leads us to consider the pin with nominal contrast of 5 HU (0.5%). Our results suggest that the use of a phantom with fixed lesion location may therefore be adequate for optimization of routine liver protocols when the detection of small lesions is required. We repeat the same procedure, by positioning the ROI above the insert.

We note that it is very difficult to place the region of interest, because the pin has a very limited visibility. We must be careful do not incorporate the background when we calculate the CT mean values.

	Nominal contrast 0.5%		
	Kernel A	Kernel B	Kernel C
FBP	2.4± 0.3	1.8± 0.2	1.4± 0.2
idose 1	2.5± 0.2	2.0± 0.2	1.6± 0.2
idose 2	2.7± 0.2	2.1± 0.2	1.6± 0.1
idose 3	2.8± 0.2	2.3± 0.2	1.8± 0.1
idose 4	3.0± 0.1	2.4± 0.2	1.9± 0.1
idose 5	3.2± 0.1	2.6± 0.1	2.1± 0.1

Table 4.8: CNR values both standard and iterative reconstruction; nominal contrast 0.5%.

In this case, the variations for kernel B and C are 0.4 (FBP) and 0.5 (iterative algorithm).

Obviously, also in this case, the filter A maintains an higher value, respecting the intrinsic characteristics of contrast resolution (i.e, this filter allows to study better low contrast lesions).

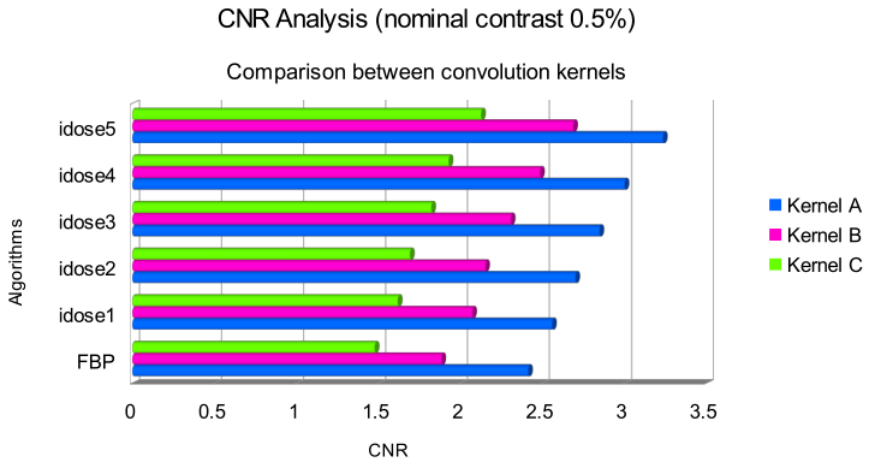

Figure 4.19: Contrast to noise ratio for iterative and standard algorithm.

The standard deviation obtained when smaller pin sizes were used, were significantly increased compared to a nominal contrast of 1% and 2%. The increase of SD as resulted in a decrease of the CNR of the images acquired when using filtered back projection compared to iterative reconstruction.

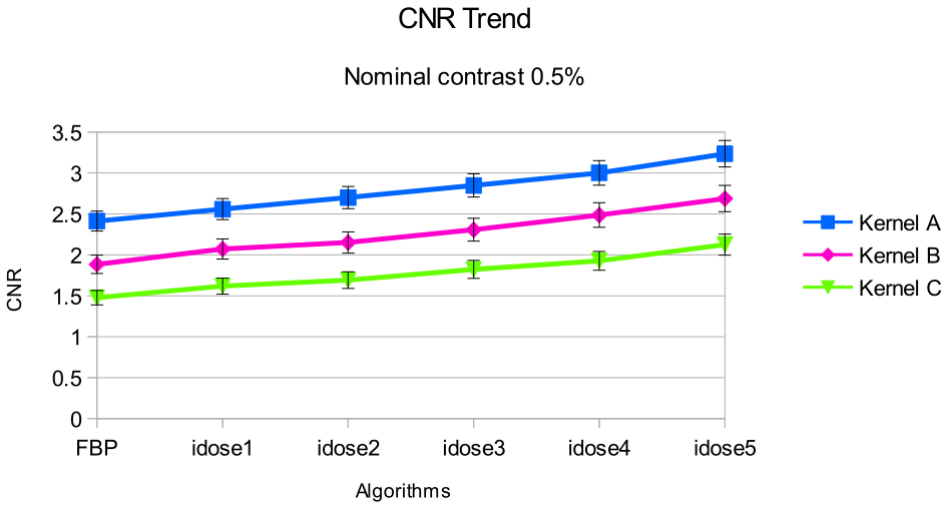

Figure 4.20: Trends of contrast to noise ratio at varying levels of reconstruction.

In this plot, the trends of CNRs are almost linear, except for the range between FBP and level 2 of iDose (kernel B and C).

If we consider the sharp filter, we notice slight differences from linearity also in the transition from level 4 to level 5 of iterative reconstruction.

Chapter 5

Dose Assessment

CT and dose, far too often a book of mystery for many of those who have to deal with this imaging modality. When asking somebody for the radiation exposure from a given CT examination, the casual answer is: "so and so many mAs". Even in scientific publications the applied current-time product is used as a synonym for radiation exposure.

This point of view is not completely wrong as there is a linear relationship between the applied tube current-time product and radiation dose. However, it is often not recognized that this relationship differs depending on the type of scanner. Dose comparisons in terms of mAs statements are therefore not appropriate in the field of CT and are far from allowing a reasonable indication of the radiation exposure relative to that from conventional x-ray projection techniques.

In this context it has turned out as very useful to distinguish between local and integral dose quantities. Local dose quantities are indicators of the intensity of the irradiation inside the limits of the irradiated body region[48].

Computed tomography Dose Index (CTDI), dose free-in-air on the axis of rotation and organ dose are members of this group. In contrast, integral dose quantities. such as dose-lengh product (DLP) and effective dose, are descriptors of the total amount of radiation absorbed by taking into account also the extent of the body region being irradiated.

5.1 Computed Tomography Dose Index

The CTDI has for many years commonly been used as the most-specific dose quantity for CT. Whenever, as usually occurs in practice, several adjacent slices are scanned instead of a single slice, the dose for a particular slice is increased due to the contributions from slices in its neighbourhood.

If the examination is performed with overlapping slices, i.e. by using a table feed smaller than the slice thickness, the increase in dose becomes even larger. The packing factor is used as an indicator of the degree of overlap, which is roughly given by the ratio of slice thickness and table feed, i.e. pitch.

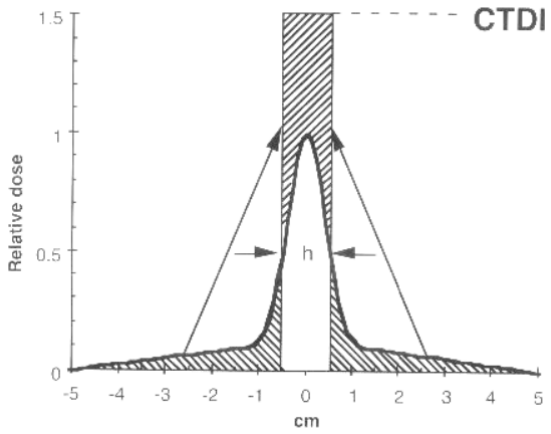

Figure 5.1: Illustration of the term "Computed Tomography Dose Index".

Fig.[5.1] illustrates the meaning of this term: the CTDI is the equivalent of the dose value inside the irradiated slice that would result if the absorbed radiation dose profile were entirely concentrated to a rectangular profile of width equal to the nominal slice thickness. All dose contributions from outside the nominal slice width are added to the area inside the slice[49].

The corresponding mathematical definition of CTDI therefore describes the summation of all dose contributions along a line which is parallel to the axis of rotation for the scanner

$$CTDI = \frac{1}{h}\int_{-\infty}^{+\infty} D(z)dz \qquad [mGy] \tag{5.1}$$

where $D(z)$ is the value of the dose at a given location z, and h is the nominal slice thickness. CTDI is therefore equal to the area of the dose profile (the DLP) divided by the nominal slice thickness.

Weighted CTDI is a weighted mixture of the pair of CTDI_{100} values, with weightings of $\frac{1}{3}$ for the central $\mathrm{CTDI}_{100,c}$ and $\frac{2}{3}$ for the peripheral $\mathrm{CTDI}_{100,p}$:

$$CTDI_w = \frac{1}{3}CTDI_{100,c} + \frac{2}{3}CTDI_{100,p} \tag{5.2}$$

CTDI_w must be calculated separately for both the head and body phantoms. It is important to differentiate between absolute and normalized values

of $CTDI_w$. The only advantage is that it enables the use of a single number instead of two, particularly in the case of the body region where the central and peripheral values are not of the same magnitude.

5.2 Dose Length Product

CTDI, weighted CTDI and axial dose free-in-air are by definition only indicators of the level of local dose in the irradiated slice. Dose is an indicator of the intensity of irradiation inside the irradiated part of the body, but only here. If an organ, such as the liver, is already completely situated inside the scan range, then the dose to the liver remains the same even if the scan range is further extended. Only in those cases where an organ was partially irradiated, will the organ dose grow with the increasing scan length, but only once again until the organ is fully irradiated[50].

In conventional projection radiography, the quantity dose area product (DAP) is used ti express both aspects of an irradiation, intensity and extent. The analogy for CT, where the diameter of body is always completely irradiated, is dose length product (DLP).

DLP is obtained by multiplying one of the dose quantities appropriate for CT wit the product pf the number of slices n and the slice thickness h:

$$DLP_{x,y,z} = CTDI_{x,y,z} \cdot n \cdot h \qquad [mGy \cdot cm] \tag{5.3}$$

The suffix "w" or "air" tells us which kind of CTDI was used. This difference is important if DLP is used to assess effective dose. In this definition of DLP, pitch-related effects have already been taken into account, since instead of the scan length L, the product of the number of slices and their thickness is used.

Since the pitch factor is already implicitly contained in (5.3), some care is necessary in order not to correct for pitch for a second time when calculating DLP from the effective CTDI displayed at the operator's console. In these cases, the calculation of DLP_w must be made using a different formula such as

$$DLP_w = CTDI_{w,eff} \cdot p \cdot n \cdot h \tag{5.4}$$

so as to convert from effective CTDI into weighted CTDI. It would appear that the DLP discussed here is the same quantity as that already mentioned in the context of the definition of CTDI. It is important to recognize that here the DLP stands for the entire scan series, with "length" meaning the dimension of the irradiated part of the body. In the case of the dose length product for a single slice, "length" means the dimension over which the contributions from the dose profile are summed.

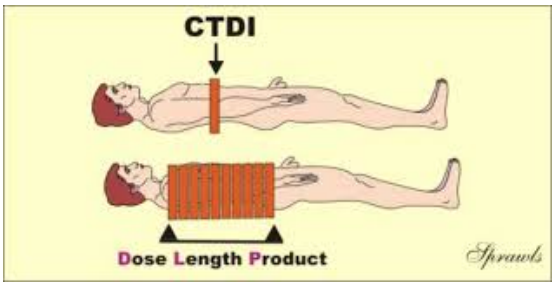

Figure 5.2: Illustration of the term "Dose Length Product".

In some examinations, more than one series of scans, is subsequently made. Dose-relevant parameters such as mAs product, slice thickness and scan length may differ from series to series. Therefore the DLP should be calculated separately for each scan series. The total radiation exposure for the complete examination is obtained by simply adding the contribution from each series.

5.3 CTDI and DLP Measurements

The CT Head/Body/Pediatric CTDI (Computed Tomography Dose Index) Phantom, in combination with a specialized CT-ion chamber, provides a means of determining the approximate dose to the patient for a given series of scans. The CT head and body phantoms are designed in accordance with the FDA standard for diagnostic x-ray units, specifically as applied to CT systems.

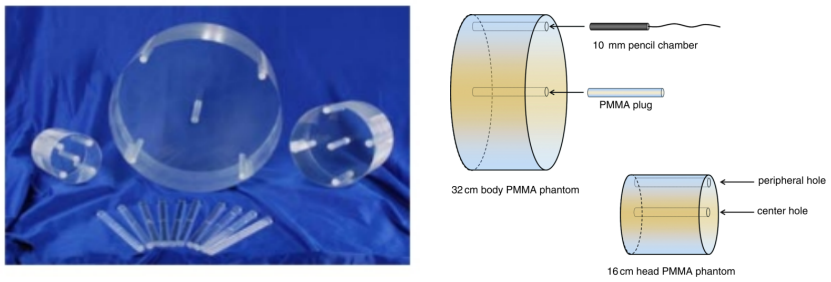

Figure 5.3: Phantom kit to evaluate CTDI (LEFT) and internal view with pencil chamber (RIGHT).

The phantoms can be used with any computed tomography system designed to image both adult and pediatric head and body. They can separately dose information for each. When performing dose profile measurements, the

dose phantoms allow the user to collect information for the maximum, minimum, and mid-range value of the nominal tomographic sections thickness.

This essential phantom kit consists of three parts: an adult body phantom, an adult head phantom that doubles as a pediatric body phantom, and a pediatric head phantom. All are made of solid acrylic and 15 cm thick with diameters of 32 cm, 16 cm, and 10 cm respectively. Each part contains five probe holes-one in the center and four around the perimeter-that are 90 degrees apart and 1 cm from the edge. The inside diameter of the holes is 1.3 cm. Each part includes five acrylic rods for plugging all the holes in the phantom.

In this case, since it uses a long pencil-like detectors with active lengths of 100 mm, Eq.(5.1) becomes

$$CTDI_{100} = \frac{1}{h}\int_{-50}^{+50} D(z)dz \qquad [mGy] \tag{5.5}$$

CTDI_{100} has been generally accepted as a standard CT dose descriptor. Finally, CTDI obtained by Dosewatch software can be written as

$$CTDI_{vol} = \frac{CTDI_w}{pitch} \qquad [mGy] \tag{5.6}$$

Whereas CTDI_w represents the average absorbed radiation dose over the x and y directions at the center of the scan from a series of axial scans where the scatter tails are negligible beyond the 100 mm integration limit, CTDI_{vol} represents the average absorbed radiation dose over the x, y and z directions.

5.3.1 Protocols and Method

The CTDI_{vol} is an objective technical dose parameter based on a measured quantity. It takes into account protocol-specific parameters and is useful to compare different scan protocols across various CT scanners. Thus, IEC standards require the prospective display of the CTDI_{vol} on the console of the CT scanner.

To represent the overall dose of a given scan protocol (in this case abdomen, chest and head), the CTDI_{vol} is multiplied with the examination range which then yields the DLP.

We utilized Dosewatch GE software, that retrieves, tracks and reports the radiation dose administrated to patients during medical exams and automatically organizes the data for hospital leaders. The system collects data may be analyzed in different way, from imaging device. It can than compare and contrast the CTDI and DLP being administered in one exam to another in the past.

We consider the main protocols on which is applied the iterative reconstruction algorithm and evaluate CTDI and DLP to compare with filtered back projection.

Table 5.1 shows the sample exams taken into account to calculate CTDI and DLP, which we than compared with the national DLR values (dose reference values for CT examinations, D.L. 187/00). For iterative algorithm, each of these protocols uses a particular convolution kernel that has reconstructed them on various levels.

Sample exams

Protocols	Standard	Iterative	DLR CTDI	DLR DLP
CT Head	2896	112	60	1050
CT Abdomen	6285	1163	35	780
CT Chest	9364	1968	30	650

Table 5.1: Number of exams analyzed to calculate Computed Tomography Dose Index and Dose Length Product.

Standard Algorithm

Protocols	Kernel	CTDI $[mGy]$	DLP $[mGy \cdot cm]$
CT Head	SOFT	64± 5	1140± 200
CT Abdomen	SOFT	20± 7	840± 390
CT Chest	DETAIL	18± 6	563± 220

Table 5.2: Comparison of calculated CTDI_{vol} and DLP mean values for different protocols, by using standard reconstruction algorithm.

Iterative Algorithm

Protocols	Kernel	iDose level	CTDI $[mGy]$	DLP $[mGy \cdot cm]$
CT Head	SOFT	2	60± 1	1014± 58
CT Abdomen	SOFT	3	12± 5	520± 230
CT Chest	DETAIL	4	10± 4	390± 130

Table 5.3: Comparison of calculated CTDI_{vol} and DLP mean values for different protocols, by using iterative reconstruction algorithm.

Tabs 5.2 and 5.3 show the examined protocols and the results obtained with standard reconstruction and iterative reconstruction.

- The standard algorithm show a good agreement for CT chest and CT abdomen with DLR ; while the value of CT head is to the limit with reference values.

- The iterative algorithm show a good agreement for all three protocols, but the most important thing that we may notice is a reduction in the values of CTDI and DLP compared to the standard algorithm.

CTDI and DLP values were extrapolated on a large numbers of patients, subjected to the same type of examinations.

The variations on abdomen and chest regions is due to the patient size variability.

Errors in DLP values take into account both patient size and variability in multiphase length, in particular for abdomen.

Chapter 6

Conclusions

In this thesis we studied the approaches to the objective assessment of the quality of iteratively reconstructed CT images, compared to filtered back projection (FBP). The work presented here provides an objective and robust way to quantitatively assess the image quality impact of newly introduced CT iterative reconstruction (IR) analyzing the noise power spectrum, the modulation transfer function and the contrast-to-noise ratio. The main results obtained have been:

- According to our measures, the performance of the IR shows that the image quality is better than the traditional FBP algorithm. Our results indicate that iDose^4 IR can be another tool allowing for a reduction of noise. Scans reconstructed with iDose^4 have a higher CNR compared to filtered back projection. The ability of iDose^4 to improve low-contrast object detection depends on the levels of reconstruction.

- Our MTF measurements showed that the high-contrast resolution not differs for the FBP and iDose^4 reconstructions. Spatial resolution was largely unaffected by the IR levels.

- iDose^4 allows us to tailor our CT scanning protocols to each clinical indication, resulting in optimal image quality with the lowest radiation dose. This algorithm reduces the radiation dose compared to FBP and national DLR values.

The potential for patient dose reduction is generally considered the biggest advantage of IR methods, and applications such as CT imaging, where dose figures are of great concern, are a prime target. For this reason, an optimization process with a Radiologist and a Physicist should be made to determine the appropriate dose to obtain diagnostic image quality for the particular clinical task.

This suggests that further study are necessary to analyze image quality and dose patient. In addition, further verification using patient data and human observer study are needed to fully develop low dose patient scan protocols using IR algorithm. Real time reconstruction speed, the availability to all CT imaging modes, and the large dose saving make this IR method a good candidate to replace FBP as the routine reconstruction method used in CT.

Appendix A

Images, tables and surface plot

A.1 Body Phantom images

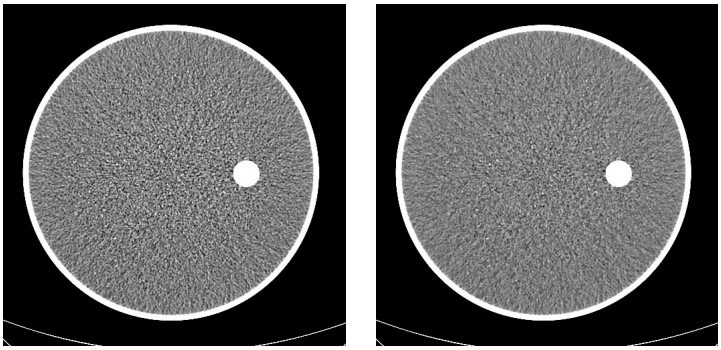

Figure A.1: Filtered Back Projection reconstruction with kernel A (LEFT). Iterative reconstruction with kernel A (RIGHT).

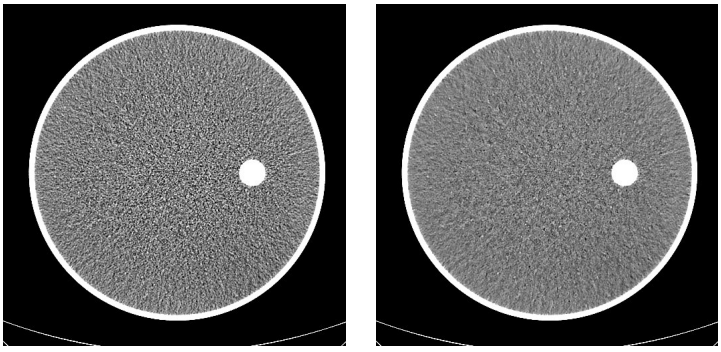

Figure A.2: Filtered Back Projection reconstruction with kernel B (LEFT). Iterative reconstruction with kernel B (RIGHT).

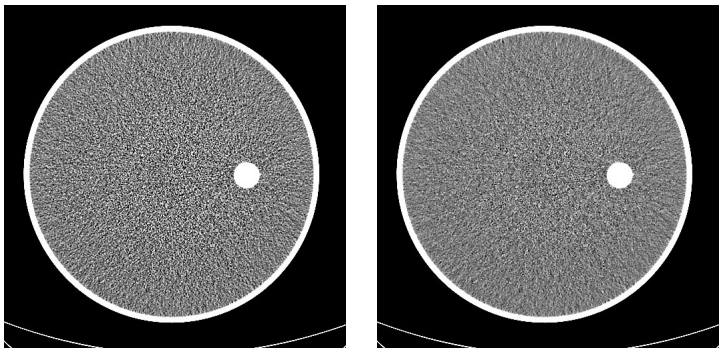

Figure A.3: Filtered Back Projection reconstruction with kernel C (LEFT). Iterative reconstruction with kernel C (RIGHT).

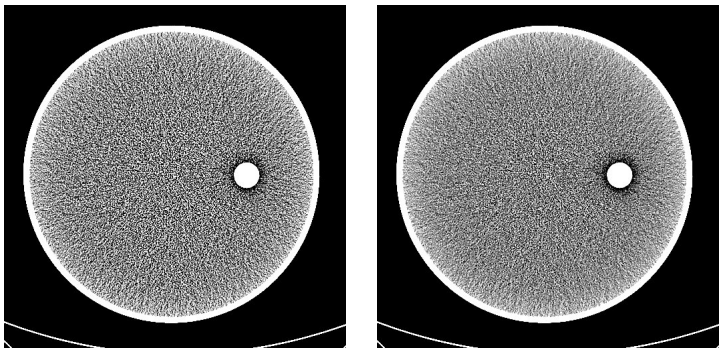

Figure A.4: Filtered Back Projection reconstruction with kernel D (LEFT). Iterative reconstruction with kernel D (RIGHT).

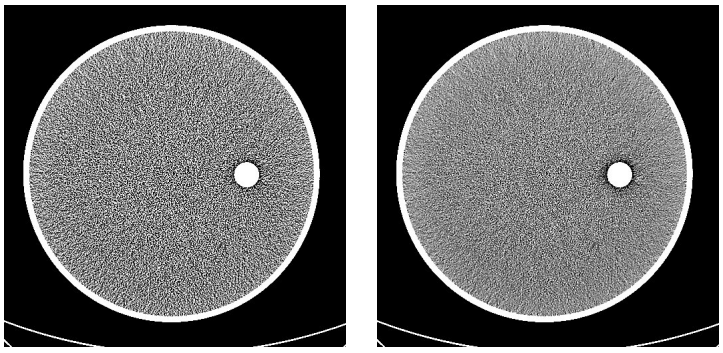

Figure A.5: Filtered Back Projection reconstruction with kernel DH (LEFT). Iterative reconstruction with kernel DH (RIGHT).

A.2 Head Phantom images

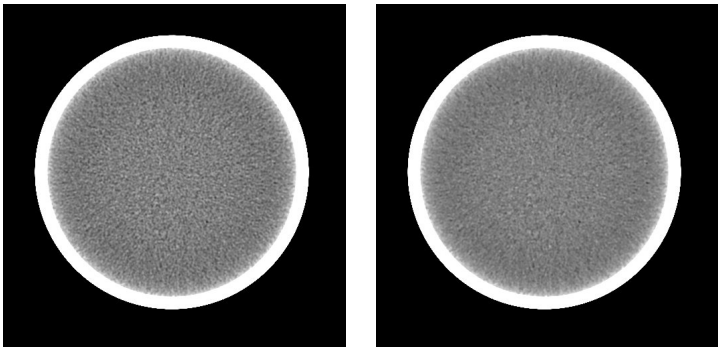

Figure A.6: Filtered Back Projection reconstruction with kernel A (LEFT). Iterative reconstruction with kernel A (RIGHT).

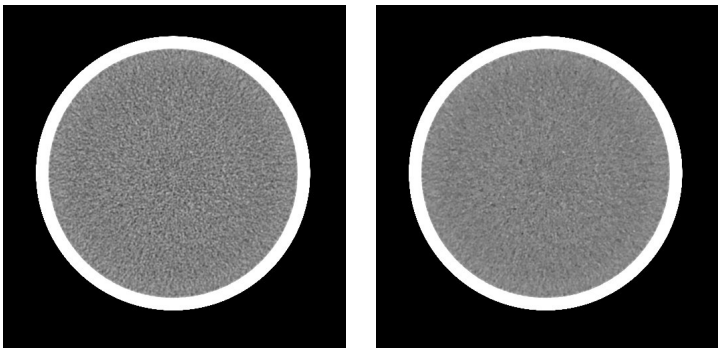

Figure A.7: Filtered Back Projection reconstruction with kernel UB (LEFT). Iterative reconstruction with kernel UB (RIGHT).

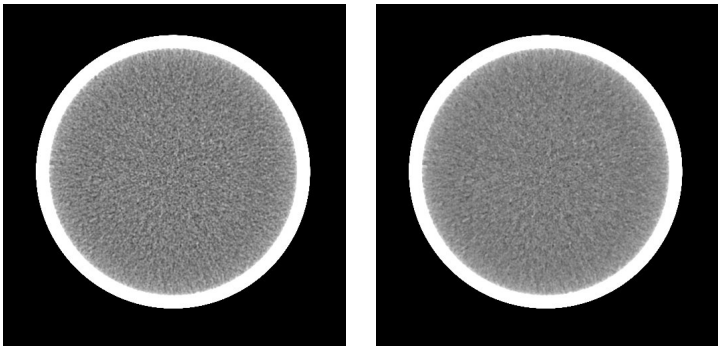

Figure A.8: Filtered Back Projection reconstruction with kernel EB (LEFT). Iterative reconstruction with kernel EB (RIGHT).

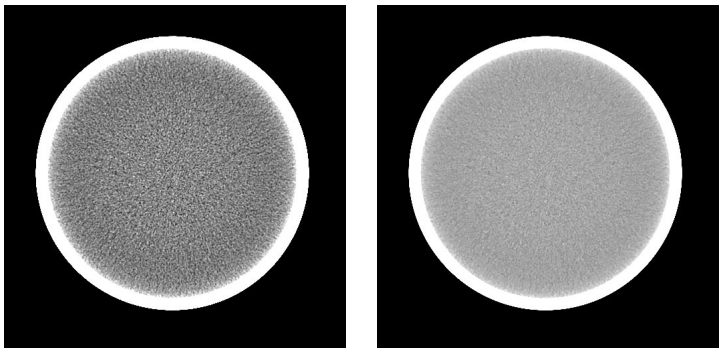

Figure A.9: Filtered Back Projection reconstruction with kernel C (LEFT). Iterative reconstruction with kernel C (RIGHT).

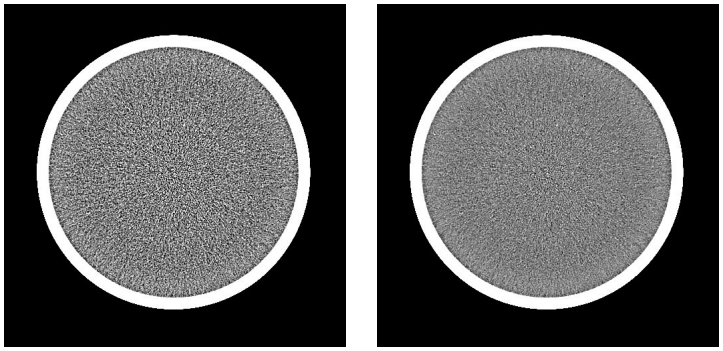

Figure A.10: Filtered Back Projection reconstruction with kernel D (LEFT). Iterative reconstruction with kernel D (RIGHT).

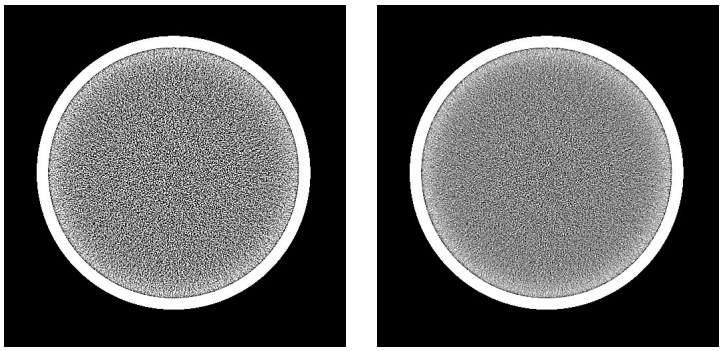

Figure A.11: Filtered Back Projection reconstruction with kernel DH (LEFT). Iterative reconstruction with kernel DH (RIGHT).

A.3 NNPS tables both FBP and iterative algorithm, head and body phantoms. 3D surface plot.

Spatial Frequency	Average KERNEL D (H)	Average KERNEL D	Average KERNEL A	Average KERNEL C	Average KERNEL EB	Average KERNEL D (H) FBP	Average KERNEL D FBP	Average KERNEL A FBP	Average KERNEL C FBP	Average KERNEL EB FBP	Average KERNEL UB	Average KERNEL UB FBP
0	0	0	0	0	0	0	0	0	0	0	0	0
0.0320053257	3.67E-005	3.93E-005	2.41E-005	2.36E-005	3.36E-005	4.92E-005	5.71E-005	2.65E-005	2.63E-005	3.61E-005	2.48E-005	2.77E-005
0.0640106514	4.28E-005	5.59E-005	3.15E-005	4.04E-005	3.87E-005	6.58E-005	7.61E-005	3.67E-005	4.73E-005	4.42E-005	3.54E-005	4.06E-005
0.0960159771	5.05E-005	6.31E-005	3.73E-005	4.20E-005	4.86E-005	8.84E-005	9.66E-005	4.68E-005	5.22E-005	5.92E-005	3.78E-005	4.65E-005
0.1280213027	6.77E-005	7.00E-005	3.91E-005	4.55E-005	5.37E-005	1.29E-004	1.42E-004	5.29E-005	6.09E-005	7.09E-005	3.70E-005	4.87E-005
0.1600266284	8.15E-005	8.29E-005	3.77E-005	5.19E-005	5.06E-005	1.60E-004	1.74E-004	5.68E-005	7.73E-005	7.50E-005	3.38E-005	4.98E-005
0.1920319541	9.43E-005	1.07E-004	3.53E-005	4.77E-005	4.47E-005	1.83E-004	1.83E-004	5.83E-005	7.75E-005	7.37E-005	3.77E-005	6.06E-005
0.2240372798	1.14E-004	1.06E-004	3.22E-005	5.27E-005	3.60E-005	2.20E-004	2.03E-004	5.85E-005	9.30E-005	6.59E-005	3.35E-005	5.95E-005
0.2560426055	1.40E-004	1.21E-004	2.69E-005	5.12E-005	3.12E-005	2.76E-004	2.36E-004	5.31E-005	9.67E-005	6.13E-005	3.19E-005	6.06E-005
0.2880479312	1.60E-004	1.24E-004	2.34E-005	4.81E-005	2.84E-005	3.25E-004	2.60E-004	4.88E-005	9.50E-005	5.85E-005	2.78E-005	5.52E-005
0.3200532569	1.70E-004	1.30E-004	2.19E-005	5.03E-005	2.40E-005	3.53E-004	2.82E-004	4.66E-005	1.02E-004	5.10E-005	2.36E-005	4.80E-005
0.3520585825	1.91E-004	1.28E-004	1.79E-005	4.96E-005	2.11E-005	3.99E-004	2.89E-004	3.82E-005	1.01E-004	4.53E-005	2.19E-005	4.52E-005
0.3840639082	2.21E-004	1.30E-004	1.49E-005	4.78E-005	1.81E-005	4.55E-004	2.91E-004	3.20E-005	9.60E-005	3.83E-005	1.92E-005	3.94E-005
0.4160692339	2.30E-004	1.44E-004	1.24E-005	4.47E-005	1.50E-005	4.62E-004	2.97E-004	2.65E-005	8.85E-005	3.09E-005	1.59E-005	3.23E-005
0.4480745596	2.49E-004	1.44E-004	8.42E-006	4.29E-005	1.23E-005	4.90E-004	2.80E-004	1.77E-005	8.38E-005	2.50E-005	1.27E-005	2.56E-005
0.4800798853	2.73E-004	1.48E-004	6.46E-006	3.87E-005	9.37E-006	5.28E-004	2.87E-004	1.35E-005	7.49E-005	1.87E-005	1.03E-005	2.06E-005
0.512085211	2.96E-004	1.55E-004	4.53E-006	3.39E-005	7.90E-006	5.65E-004	2.89E-004	9.35E-006	6.53E-005	1.56E-005	7.33E-006	1.45E-005
0.5440905367	2.99E-004	1.44E-004	2.71E-006	3.18E-005	6.16E-006	5.71E-004	2.78E-004	5.63E-006	6.17E-005	1.22E-005	5.36E-006	1.07E-005
0.5760958624	2.90E-004	1.38E-004	1.67E-006	2.73E-005	4.15E-006	5.55E-004	2.47E-004	3.47E-006	5.37E-005	8.24E-006	3.31E-006	6.64E-006
0.608101188	2.93E-004	1.34E-004	1.01E-006	2.31E-005	3.08E-006	5.67E-004	2.62E-004	2.06E-006	4.57E-005	6.17E-006	2.09E-006	4.22E-006
0.640106517	2.87E-004	1.27E-004	6.01E-007	1.86E-005	2.20E-006	5.62E-004	2.58E-004	1.19E-006	3.74E-005	4.44E-006	1.34E-006	2.71E-006
0.6721118394	3.04E-004	1.23E-004	3.39E-007	1.51E-005	1.50E-006	6.00E-004	2.50E-004	6.64E-007	3.06E-005	3.06E-006	7.30E-007	1.46E-006
0.7041171651	2.71E-004	1.14E-004	2.31E-007	1.35E-005	1.04E-006	5.40E-004	2.32E-004	4.30E-007	2.73E-005	2.12E-006	4.29E-007	8.24E-007
0.7361224908	2.55E-004	1.10E-004	1.87E-007	1.01E-005	7.26E-007	5.10E-004	2.13E-004	3.37E-007	2.05E-005	1.46E-006	2.84E-007	5.19E-007
0.7681278165	2.39E-004	1.00E-004	1.52E-007	7.90E-006	5.07E-007	4.78E-004	2.03E-004	2.57E-007	1.61E-005	1.00E-006	1.97E-007	3.45E-007
0.8001331422	2.30E-004	8.96E-005	1.41E-007	5.56E-006	3.85E-007	4.57E-004	1.79E-004	2.37E-007	1.13E-005	7.42E-007	1.63E-007	2.79E-007
0.8321384678	2.01E-004	8.03E-005	1.20E-007	4.17E-006	2.82E-007	3.97E-004	1.63E-004	2.03E-007	8.36E-006	5.23E-007	1.45E-007	2.38E-007
0.8641437935	1.69E-004	6.76E-005	1.18E-007	2.91E-006	2.15E-007	3.34E-004	1.32E-004	1.97E-007	5.79E-006	3.88E-007	1.40E-007	2.30E-007
0.8961491192	1.45E-004	5.66E-005	1.14E-007	1.85E-006	1.78E-007	2.83E-004	1.12E-004	1.88E-007	3.64E-006	3.06E-007	1.31E-007	2.16E-007
0.9281544449	1.07E-004	4.29E-005	1.04E-007	1.16E-006	1.39E-007	2.10E-004	8.75E-005	1.70E-007	2.27E-006	2.33E-007	1.22E-007	1.91E-007
0.9601597706	7.79E-005	3.09E-005	1.03E-007	8.03E-007	1.30E-007	1.52E-004	6.33E-005	1.64E-007	1.55E-006	2.14E-007	1.14E-007	1.80E-007
0.9921650963	5.44E-005	2.10E-005	9.54E-008	5.25E-007	1.19E-007	1.07E-004	4.32E-005	1.51E-007	1.01E-006	1.93E-007	1.10E-007	1.74E-007

Figure A.12: Average NNPS both Filtered Back Projection and Iterative reconstruction algorithm, head phantom. Spatial Frequency [mm^{-1}], NNPS [mm^2].

Spatial Frequency	Average KERNEL DH	Average KERNEL D	Average KERNEL A	Average KERNEL C	Average KERNEL B	Average KERNEL DH FBP	Average KERNEL D FBP	Average KERNEL A FBP	Average KERNEL C FBP	Average KERNEL B FBP
0	0	0	0	0	0	0	0	0	0	0
0.022860278	1.49E-004	2.10E-004	1.11E-004	1.26E-004	1.05E-004	1.89E-004	2.52E-004	1.35E-004	1.53E-004	1.26E-004
0.045720556	2.18E-004	2.80E-004	1.69E-004	1.65E-004	1.76E-004	2.76E-004	3.47E-004	2.06E-004	2.04E-004	2.12E-004
0.0685808339	3.11E-004	3.20E-004	1.90E-004	1.85E-004	1.91E-004	4.08E-004	4.18E-004	2.42E-004	2.38E-004	2.39E-004
0.0914411119	4.10E-004	4.77E-004	2.18E-004	2.09E-004	1.95E-004	5.57E-004	6.50E-004	2.92E-004	2.82E-004	2.57E-004
0.1143013899	4.53E-004	5.30E-004	2.10E-004	2.69E-004	2.12E-004	6.71E-004	7.81E-004	3.02E-004	3.91E-004	3.03E-004
0.1371616679	4.38E-004	5.35E-004	2.34E-004	2.75E-004	2.17E-004	7.07E-004	8.49E-004	3.62E-004	4.19E-004	3.34E-004
0.1600219459	5.66E-004	5.80E-004	2.34E-004	2.98E-004	2.40E-004	9.75E-004	9.96E-004	3.94E-004	4.99E-004	3.97E-004
0.1828822238	6.14E-004	6.26E-004	2.29E-004	2.79E-004	2.18E-004	0.0011335179	0.0011531514	4.08E-004	4.98E-004	3.85E-004
0.2057425018	6.76E-004	6.07E-004	2.14E-004	2.91E-004	2.01E-004	0.0013217089	0.0011756626	4.06E-004	5.49E-004	3.81E-004
0.2286027798	7.44E-004	6.70E-004	2.00E-004	3.04E-004	1.99E-004	0.0015139121	0.0013679499	3.98E-004	5.95E-004	3.95E-004
0.2514630578	8.61E-004	6.66E-004	2.02E-004	3.15E-004	2.12E-004	0.0017933222	0.0013942431	4.15E-004	6.41E-004	4.33E-004
0.2743233358	9.04E-004	6.97E-004	1.70E-004	2.97E-004	1.94E-004	0.0019194515	0.0014857653	3.60E-004	6.15E-004	4.04E-004
0.2971836138	0.0009885594	7.29E-004	1.58E-004	2.98E-004	1.94E-004	0.0021003829	0.001542222	3.39E-004	6.18E-004	4.08E-004
0.3200438917	0.0010709795	7.30E-004	1.46E-004	2.90E-004	1.77E-004	0.0022586156	0.00154033	3.13E-004	6.05E-004	3.73E-004
0.3429041697	0.0011852848	8.08E-004	1.38E-004	3.15E-004	1.78E-004	0.002464283	0.0016856831	2.97E-004	6.54E-004	3.75E-004
0.3657644477	0.001294033	8.53E-004	1.15E-004	3.12E-004	1.66E-004	0.0026396158	0.0017446659	2.44E-004	6.41E-004	3.46E-004
0.3886247257	0.001344716	8.49E-004	1.01E-004	2.85E-004	1.52E-004	0.0027068478	0.0017191926	2.15E-004	5.81E-004	3.14E-004
0.4114850037	0.0013822955	8.86E-004	8.22E-005	2.71E-004	1.32E-004	0.0027574392	0.0017769627	1.74E-004	5.53E-004	2.72E-004
0.4343452816	0.0015511664	8.61E-004	6.40E-005	2.83E-004	1.28E-004	0.0030806265	0.0017212313	1.36E-004	5.76E-004	2.64E-004
0.4572055596	0.0015199479	8.75E-004	5.05E-005	2.46E-004	1.18E-004	0.0030343654	0.0017501358	1.07E-004	5.03E-004	2.46E-004
0.4800658376	0.001614478	8.57E-004	3.90E-005	2.18E-004	1.01E-004	0.0032426979	0.0017308852	8.39E-005	4.47E-004	2.11E-004
0.5029261156	0.0016261341	7.71E-004	2.72E-005	1.99E-004	8.74E-005	0.0032991975	0.0015779403	5.89E-005	4.15E-004	1.85E-004
0.5257863936	0.001506581	7.57E-004	1.95E-005	1.80E-004	7.10E-005	0.0031015434	0.0015727099	4.27E-005	3.79E-004	1.52E-004
0.5486466715	0.0014094257	7.13E-004	1.32E-005	1.56E-004	6.03E-005	0.0029392055	0.001498276	2.92E-005	3.31E-004	1.31E-004
0.5715069495	0.0013870539	6.29E-004	9.01E-006	1.35E-004	4.89E-005	0.0029373036	0.0013394253	2.00E-005	2.89E-004	1.06E-004
0.5943672275	0.0012703051	5.55E-004	5.66E-006	1.07E-004	3.68E-005	0.0027140994	0.0011921377	1.24E-005	2.31E-004	8.03E-005
0.6172275055	0.0011136001	4.61E-004	3.70E-006	8.43E-005	2.73E-005	0.0023868125	9.98E-004	7.94E-006	1.82E-004	5.97E-005
0.6400877835	9.87E-004	3.93E-004	2.43E-006	6.23E-005	2.13E-005	0.002116111	8.50E-004	5.17E-006	1.35E-004	4.65E-005
0.6629480614	8.40E-004	3.31E-004	1.71E-006	4.75E-005	1.48E-005	0.0018013724	7.15E-004	3.49E-006	1.02E-004	3.24E-005
0.6858083394	7.07E-004	2.77E-004	1.31E-006	3.69E-005	1.06E-005	0.0015071386	5.96E-004	2.66E-006	7.88E-005	2.27E-005
0.7086686174	5.59E-004	2.05E-004	1.09E-006	2.49E-005	6.97E-006	0.0011826659	4.37E-004	2.15E-006	5.27E-005	1.49E-005

Figure A.13: Average NNPS both Filtered Back Projection and Iterative reconstruction algorithm; body phantom. Spatial Frequency [mm^{-1}], NNPS [mm^2].

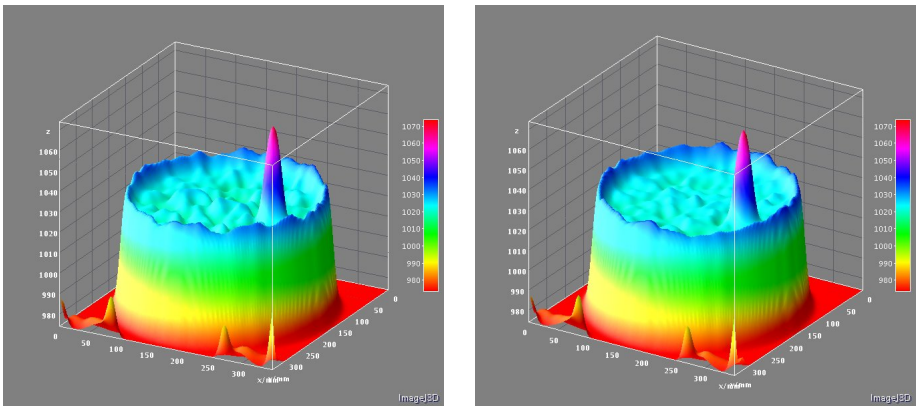

Figure A.14: Noise texture fluctuations of Filtered Back Projection algorithm with convolution kernel B (LEFT). Noise texture fluctuations of Iterative reconstruction algorithm (iDose, level 4) with same convolution kernel of FBP (RIGHT). The teflon insert is not affected by noise texture and reconstruction algorithm. Body phantom.

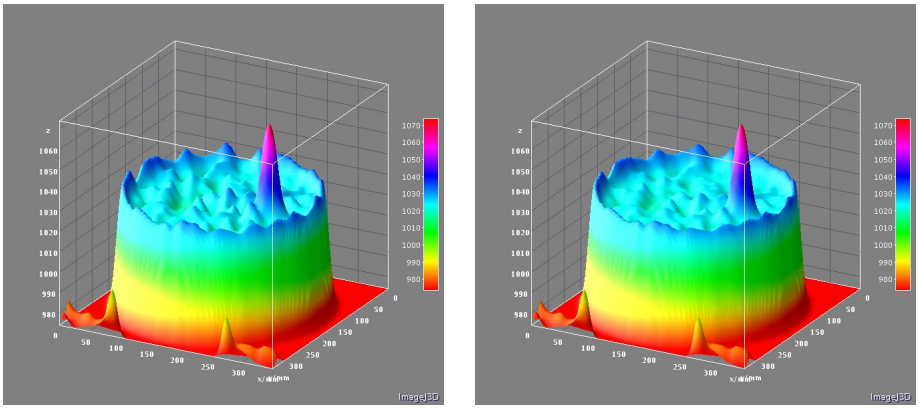

Figure A.15: Noise texture fluctuations of Filtered Back Projection algorithm with convolution kernel C (LEFT). Noise texture fluctuations of Iterative reconstruction algorithm (iDose, level 4) with same convolution kernel of FBP (RIGHT). The teflon insert is not affected by noise texture and reconstruction algorithm. Body phantom.

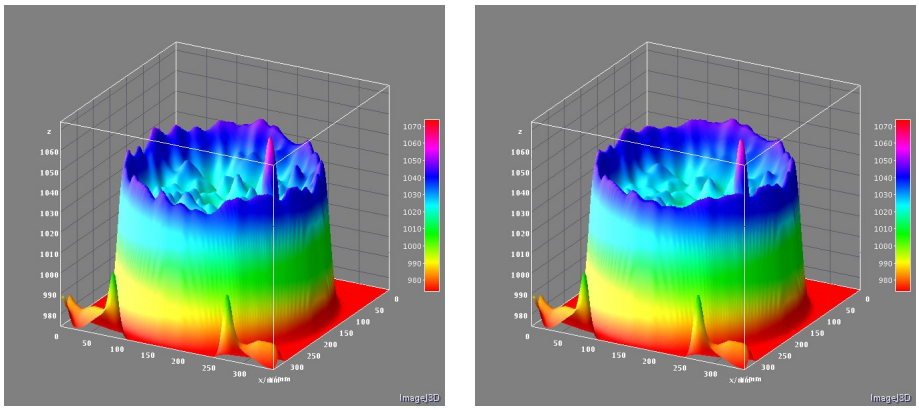

Figure A.16: Noise texture fluctuations of Filtered Back Projection algorithm with convolution kernel D (LEFT). Noise texture fluctuations of Iterative reconstruction algorithm (iDose, level 4) with same convolution kernel of FBP (RIGHT). The teflon insert is not affected by noise texture and reconstruction algorithm. Body phantom.

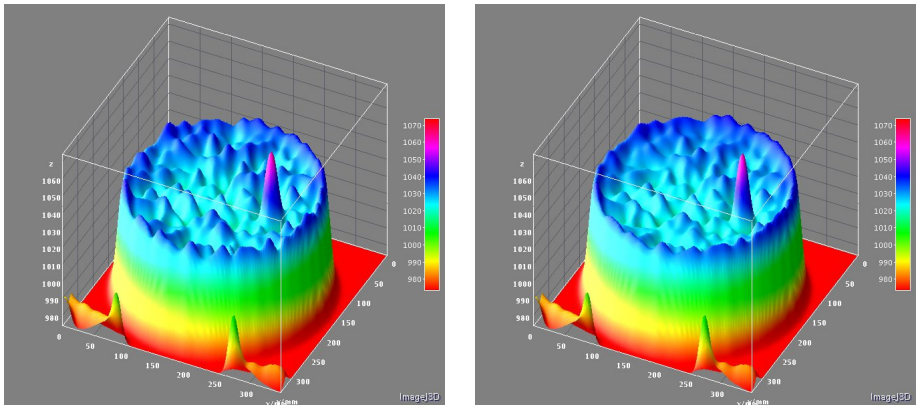

Figure A.17: Noise texture fluctuations of Filtered Back Projection algorithm with convolution kernel DH (LEFT). Noise texture fluctuations of Iterative reconstruction algorithm (iDose, level 4) with same convolution kernel of FBP (RIGHT). The teflon insert is not affected by noise texture and reconstruction algorithm. Body phantom.

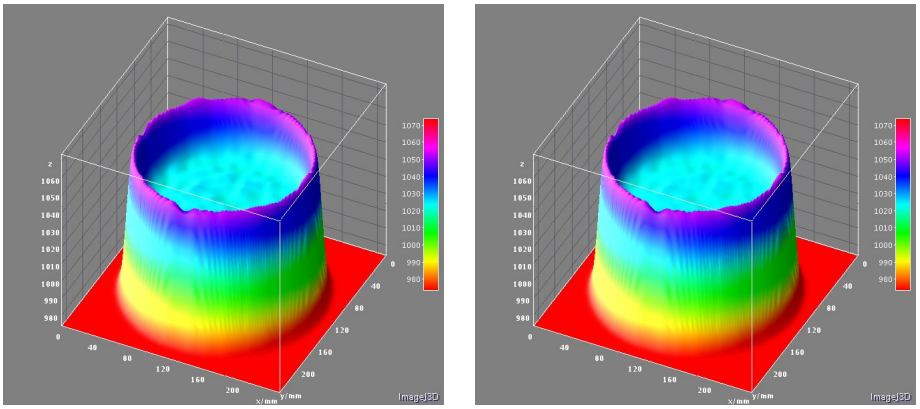

Figure A.18: Noise texture fluctuations of Filtered Back Projection algorithm with convolution kernel UB (LEFT). Noise texture fluctuations of Iterative reconstruction algorithm (iDose, level 4) with same convolution kernel of FBP (RIGHT). Head phantom.

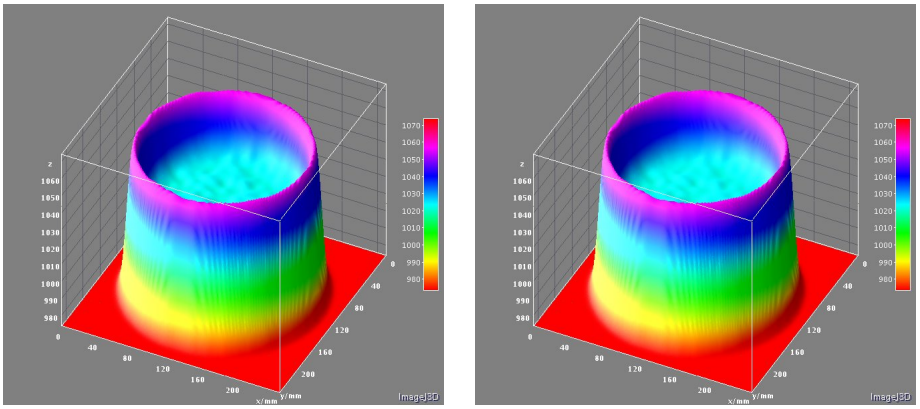

Figure A.19: Noise texture fluctuations of Filtered Back Projection algorithm with convolution kernel EB (LEFT). Noise texture fluctuations of Iterative reconstruction algorithm (iDose, level 4) with same convolution kernel of FBP (RIGHT). Head phantom.

Appendix B

CNR Plot → Catphan 600

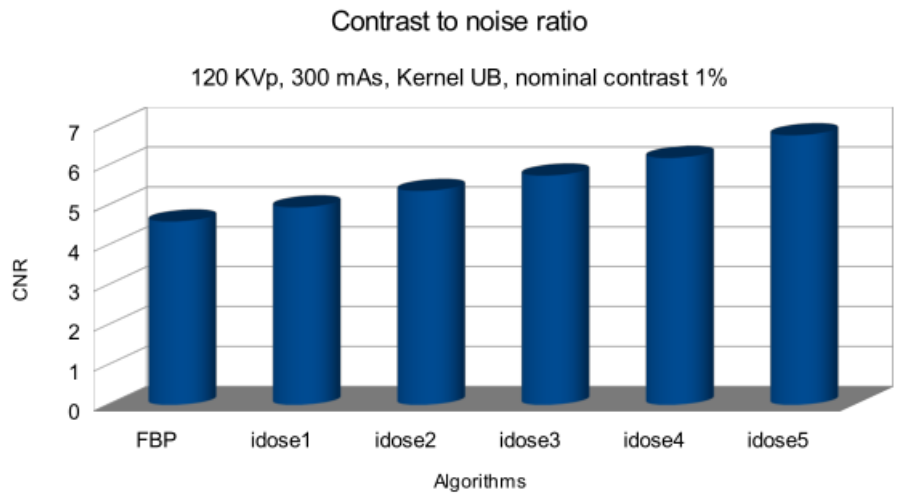

Figure B.1: CNR values for kernel UB; nominal contrast 1%.

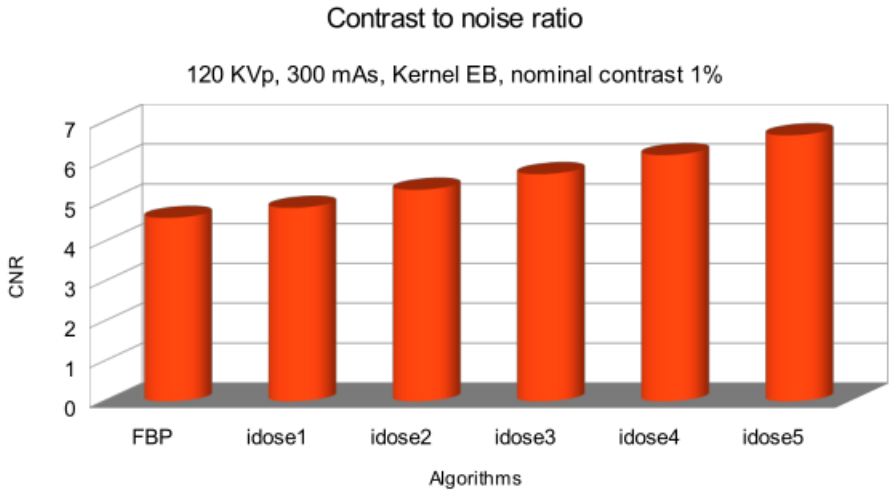

Figure B.2: CNR values for kernel EB; nominal contrast 1%.

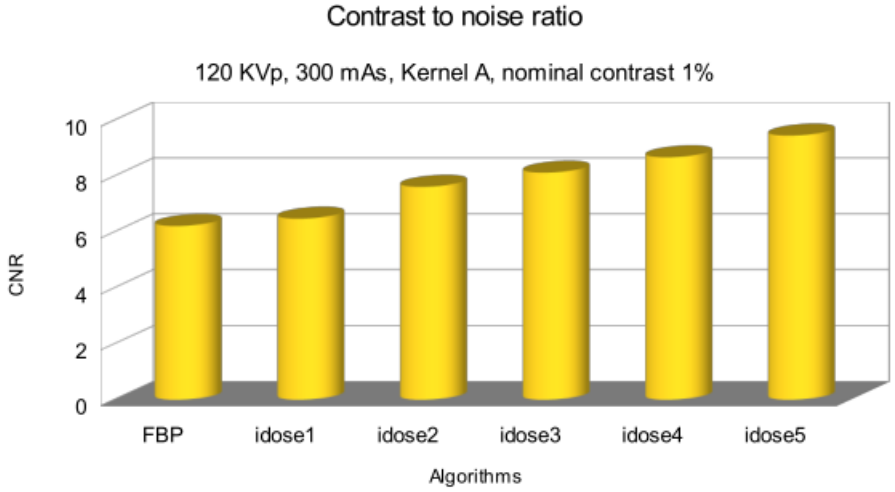

Figure B.3: CNR values for kernel A; nominal contrast 1%.

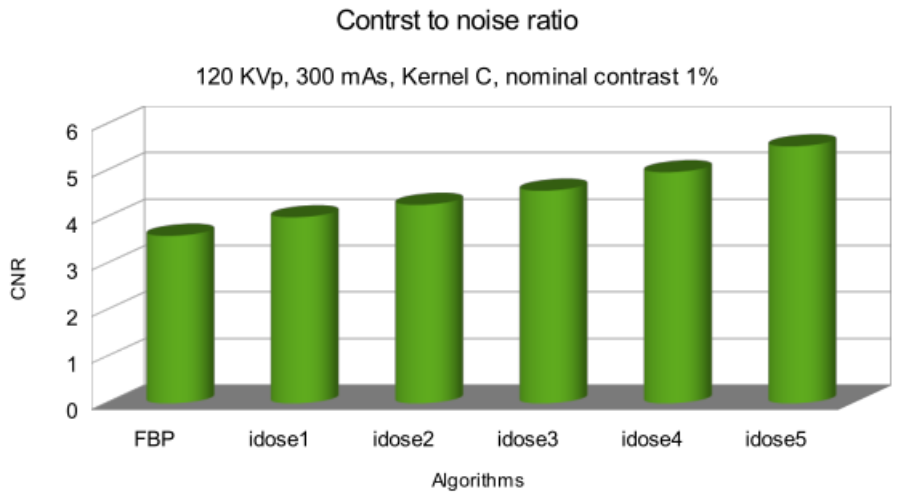

Figure B.4: CNR values for kernel C; nominal contrast 1%.

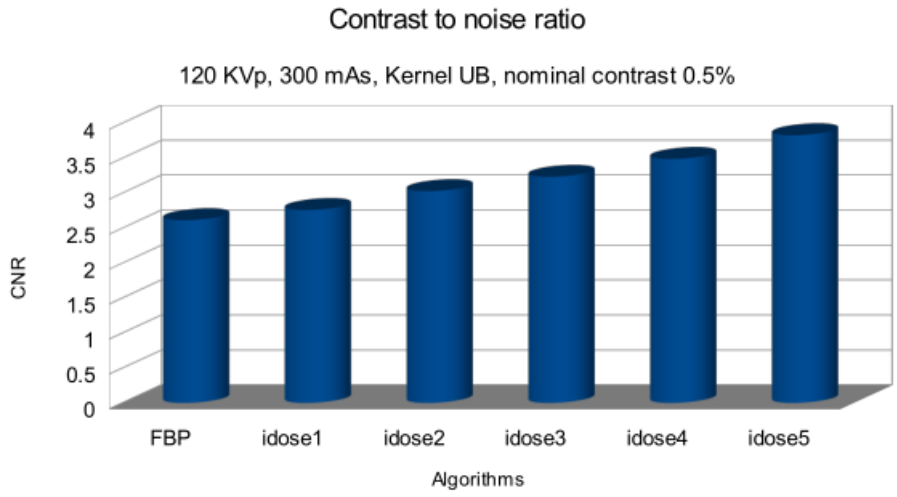

Figure B.5: CNR values for kernel UB; nominal contrast 0.5%.

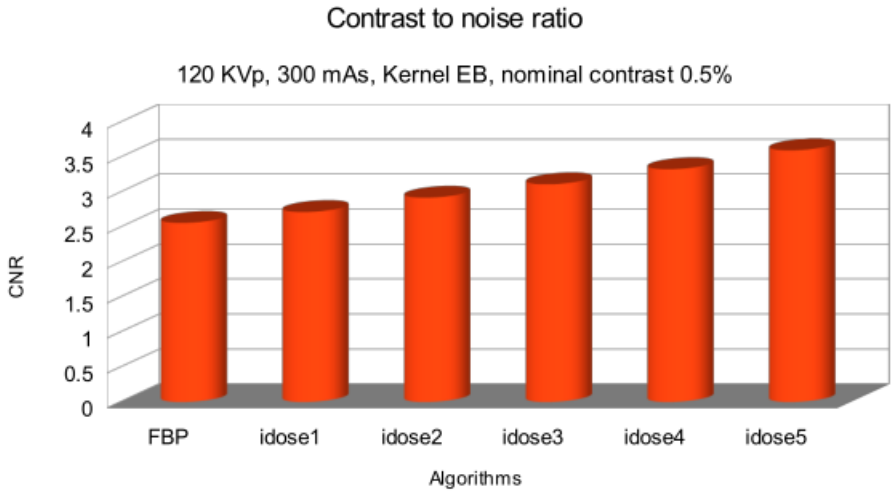

Figure B.6: CNR values for kernel EB; nominal contrast 0.5%.

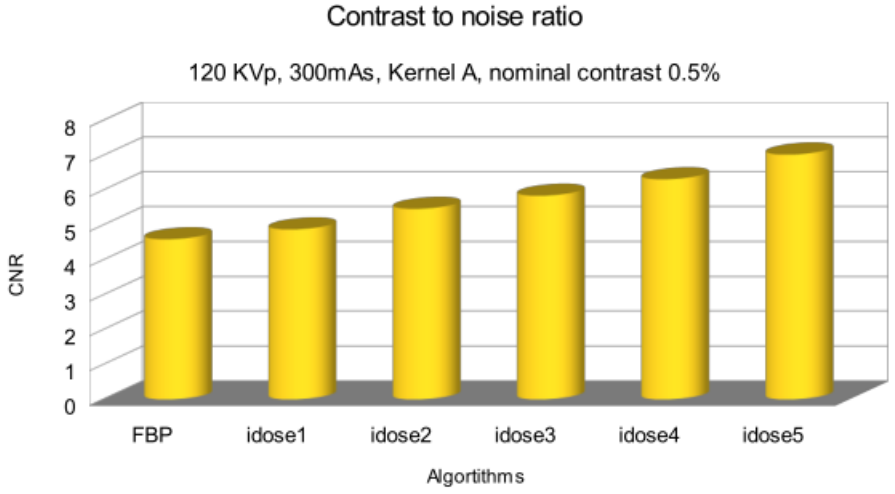

Figure B.7: CNR values for kernel A; nominal contrast 0.5%.

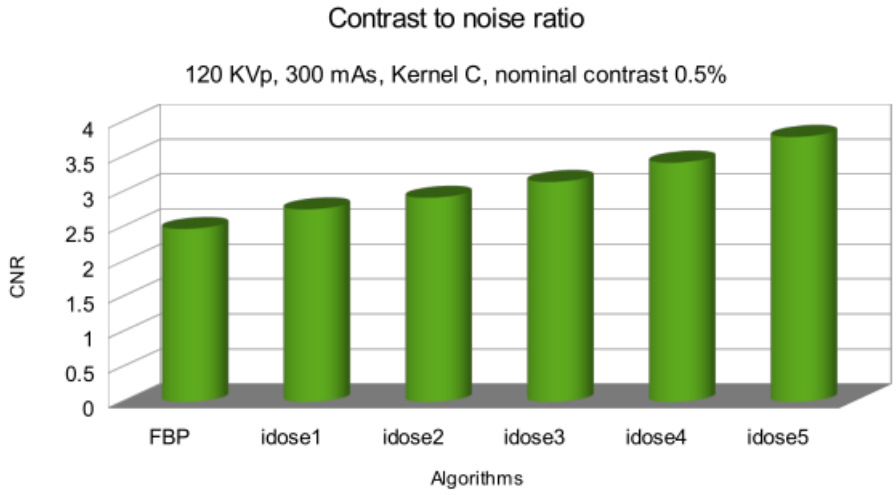

Figure B.8: CNR values for kernel C; nominal contrast 0.5%.

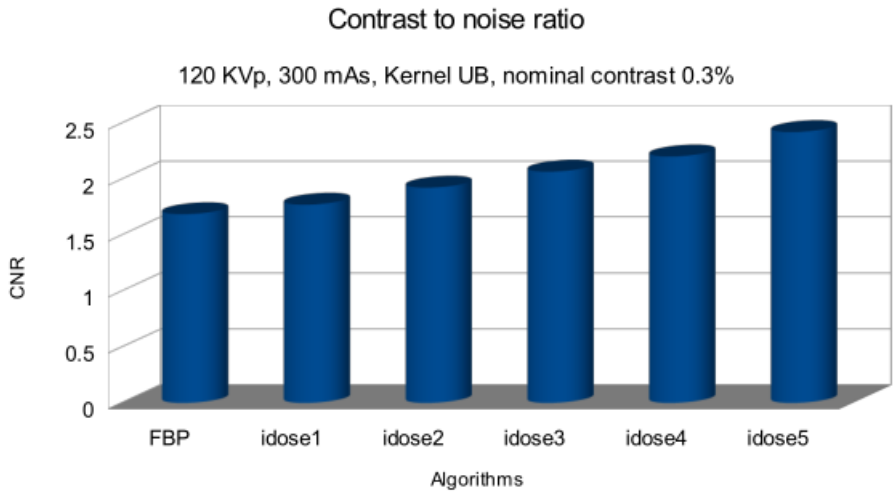

Figure B.9: CNR values for kernel UB; nominal contrast 0.3%.

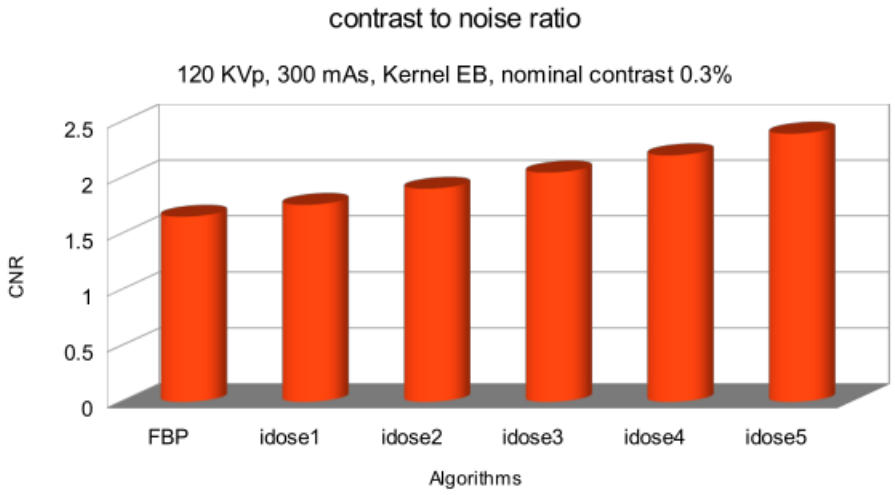

Figure B.10: CNR values for kernel EB; nominal contrast 0.3%.

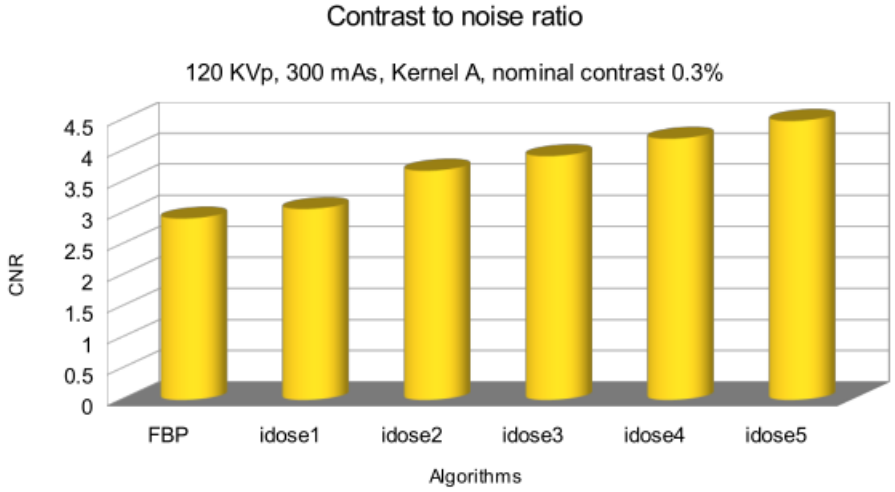

Figure B.11: CNR values for kernel A; nominal contrast 0.3%.

Appendix C

CNR plot → CIRS 061

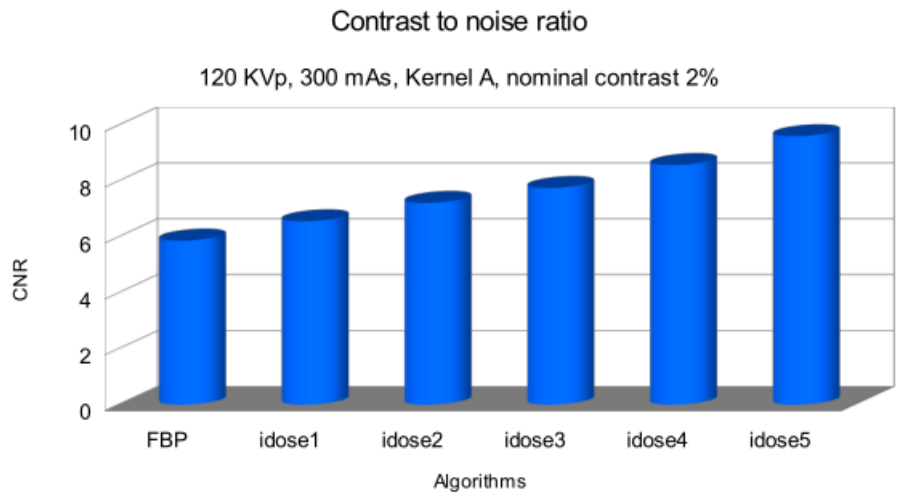

Figure C.1: CNR values for kernel A; nominal contrast 2%.

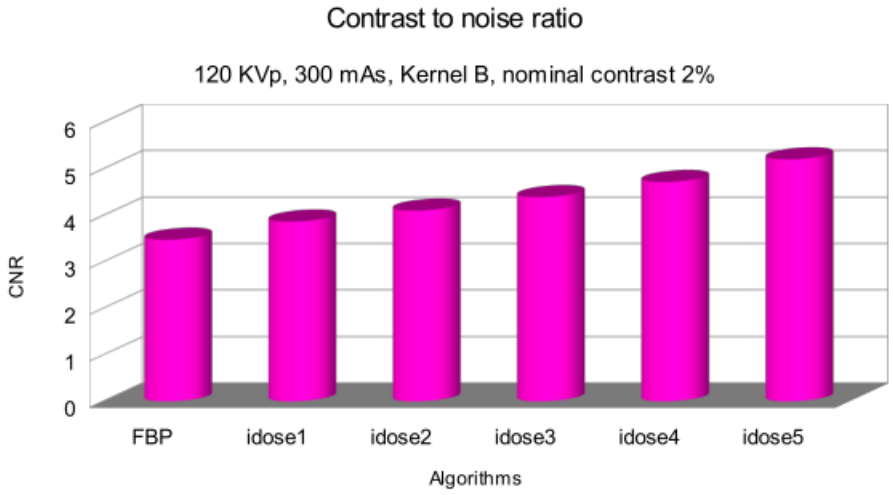

Figure C.2: CNR values for kernel B; nominal contrast 2%.

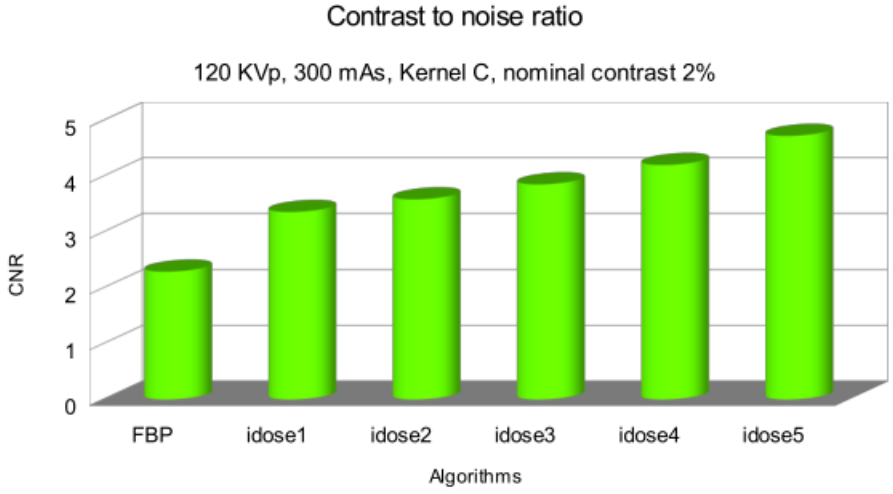

Figure C.3: CNR values for kernel C; nominal contrast 2%.

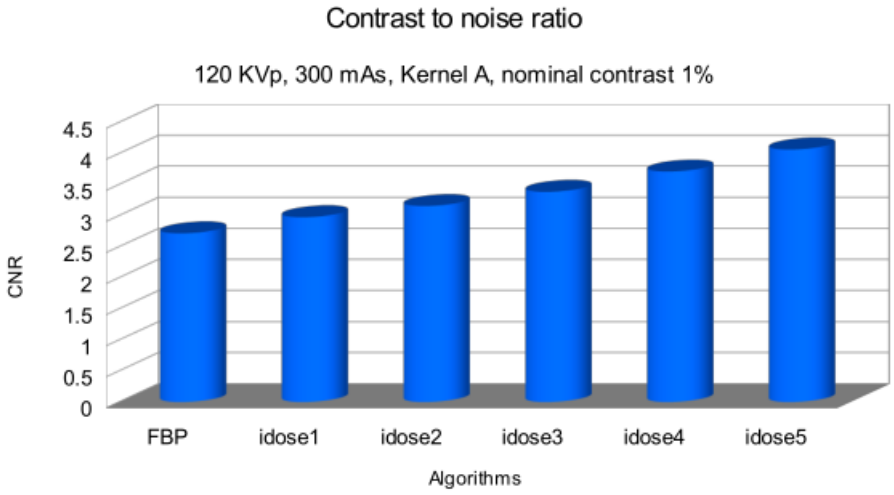

Figure C.4: CNR values for kernel A; nominal contrast 1%.

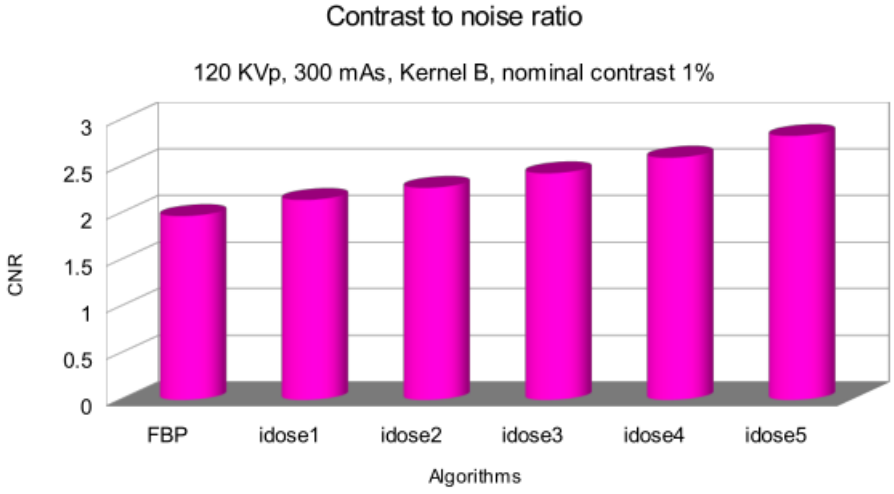

Figure C.5: CNR values for kernel B; nominal contrast 1%.

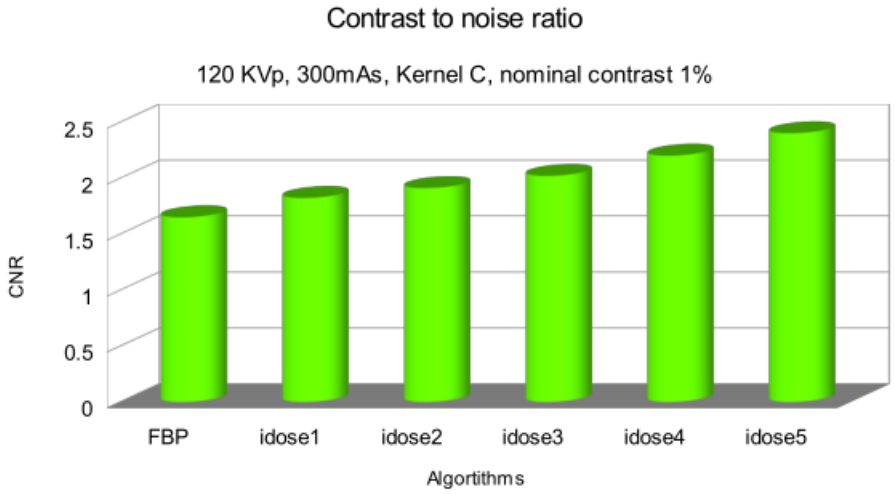

Figure C.6: CNR values for kernel C; nominal contrast 1%.

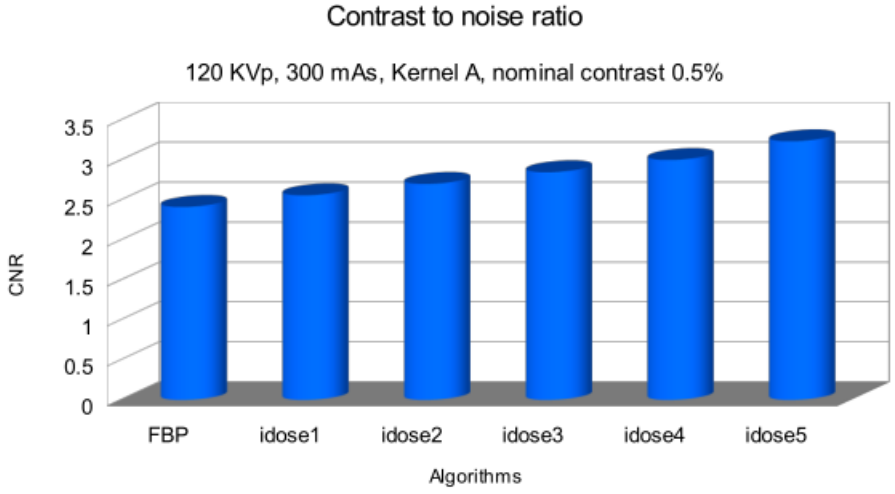

Figure C.7: CNR values for kernel A; nominal contrast 0.5%.

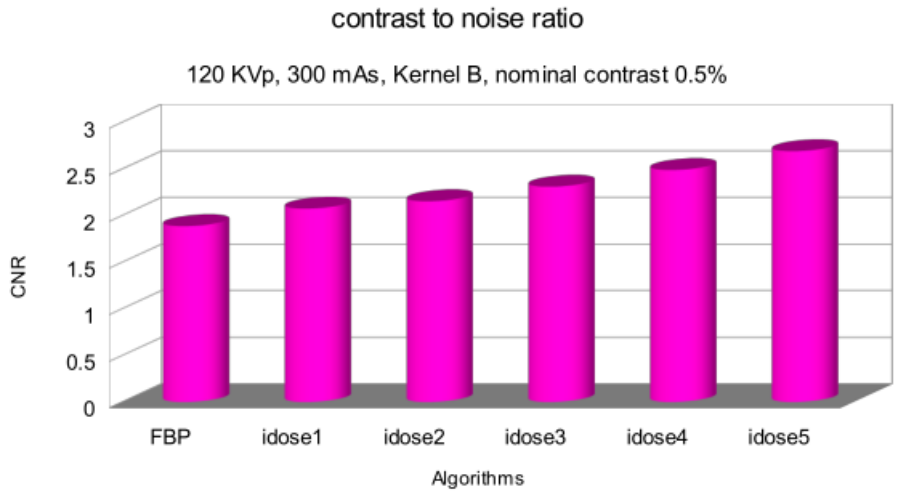

Figure C.8: CNR values for kernel B; nominal contrast 0.5%.

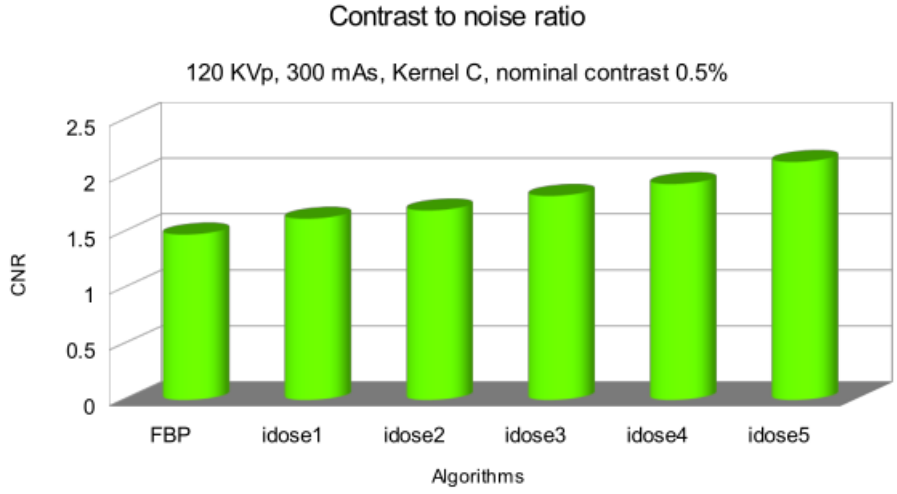

Figure C.9: CNR values for kernel C; nominal contrast 0.5%.

Bibliography

[1] J. Beutel, H.L. Kundel, R.L. Van Metter "*Handbook of Medical Imaging* ", SPIE Press, **(2000)**.

[2] International Commission "*Radiation Dose and Image Quality Assessment in Computed Tomography* ", Oxford University Press, **(2012)**.

[3] G.F. Knoll,"*Radiation Detection and Measurements*", Wiley, **(2000)**.

[4] N.A. Dyson, "*X-Rays in Atomic and Nuclear Physics*", Cambridge University Press, **(1990)**.

[5] P.R. Griffiths, "*Handbook of Vibrational Spectroscopy*", Wiley, **(2006)**.

[6] L.W. Goldman, "*Principles of CT and CT Technology*", Journal of Nuclear Medicine Technology, **(2007)**.

[7] L. Pierotti, "*Evoluzione dei sistemi TC*", Impact Scan.org, **(2013)**.

[8] L.W. Goldman, "*Principles of CT: Multislice CT*", Journal of Nuclear Medicine Technology, **(2008)**.

[9] J. Hsieh, B. Nett, Z. Yu, K. Sauer, J.B. Thibault, C.A. Bouman, "*Recent Advances in CT Image Reconstruction*", Springer-Science, **(2013)**.

[10] A.H. Hara, R.G. Paden, A.C. Silva, "*Iterative Reconstruction Technique for Reducing Body Radiation Dose at CT: Feasibility Study*", American Journal of Roengtenology, **2009**.

[11] B.P. Fahimian, Y. Zhao, Z. Huang, . Fung, Y. Mao, C. Zhu, M. Khatonabadi, J.J. DeMarco, S.J. Osher, M.F. McNitt-Gray and J. Miao, "*Radiation dose reduction in medical x-ray CT via Fourier-based iterative reconstruction*", Medical Physics, **2013**.

[12] H. Shi, S. Luo, "*A novel scheme to design the filter for CT reconstruction using FBP algorithm*", BioMedical Engineering OnLine, **2013**.

[13] M. Beister, D. Kolditz, W.A. Kalender, "*Iterative Reconstruction method in X-ray CT*", European Journal of Medical Physics, **2012**.

[14] S. Kaczmarz, "*Angenäherte Auflösung von Systemen Linearer Gleichungen*", Bull Internat Acad Polonsci Lettres A, **1937**.

[15] K.E. Jang, J. Lee, Y. Sung, S. Lee, "*Information-theoretic discrepancy based iterative reconstructions (IDIR) for polychromatic x-ray tomography*", Medical Physics, **2013**.

[16] L. Liu, "*Model-based Iterative Reconstruction: A Promising Algorithm for today's Computed Tomography Imaging*", Journal of Medical Imaging and Radiation Sciences, **2014**.

[17] H.W. Tseng, J. Fan, M.A. Kupinski, P. Sainath, J. Hsieh "*Assessing image quality and dose reduction of a new x-ray computed tomography iterative reconstruction algorithm using model observers*", Medical Physics, **2014**.

[18] A. Hara, "*ASiR reconstruction sharpens images, slices abdominal CT dose*", Mayo Clinic Arizona, **2009**.

[19] D.A. Kaplan, "*Iterative reconstruction in CT evolves for lower dose, increased clarity*", DiagnosticImaging.com, **2011**.

[20] H.S. Park, H.M. Cho, J. Jung, C.L. Lee, H.J. Kim "*Comparison of the image Noise Power Spectra for Computed Tomography*", Journal of the Korean Physical Society, **2008**.

[21] M.F. Kijewski, P.F. Judy, "*The noise power spectrum of CT images*", Physics in Medicine and Biology, **1986**.

[22] O. Rampado, "*Interconfronto metodi di valutazione NPS*", Review presentata alla città della scienza e della salute di Torino, **2014**.

[23] O. Rampado, "*Algoritmi Iterativi: Review Letteratura*", Review presentata alla città della scienza e della salute di Torino, **2014**.

[24] O. Rampado, "*Interconfronto metodi NPS: fantocci*", Review presentata alla città della scienza e della salute di Torino, **2014**.

[25] K.M. Hanson, "*Noise and contrast discrimination in computed tomography*", Radiology of the skull and Brain, **1981**.

[26] L. Berta, L. Mascaro, P. Feroldi, R. Maroldi "*Optimisation of an MDCT abdominal protocol: Image quality assessment of standard vs. iterative reconstruction*", Physica Medica, **2013**.

[27] K.L. Boedeker, V.N. Cooper, M.F. McNitt-Gray "*Application of the noise power spectrum in modern diagnostic MDCT: part 1. Measurement of noise power spectra and noise equivalent quanta*", Physics in Medicine and Biology, **2007**.

[28] K.L. Boedeker, M.F. McNitt-Gray "*Application of the noise power spectrum in modern diagnostic MDCT: part 2. Noise power spectra and signal to noise*", Physics in Medicine and Biology, **2007**.

[29] S.N. Friedman, G.S.K. Fung, J.H. Siewerdsen, B.N.W. Tsui, "*A simple approach to measure computed tomography (CT) modulation transfer function (MTF) and noise power spectrum (NPS) using the American College of Radiology (ACR) accreditation phantom*", Medical Physics, **2013**.

[30] J.H. Siewerdsen, I.A. Cunningham, D.A. Jaffray, "*A framework for noise power spectrum analysis of multidimensional image*", Medical Physics, **2002**.

[31] K. Yang, A.L.C. Kwan, S. Ying Huang, N.J. Packard, J.M. Boone, "*Noise power properties of a cone-beam CT system for breast cancer detection*", Medical Physics, **2008**.

[32] J.T. Dobbins, E. Samei, N.T. Ranger, Y. Chen, "*Intercomparison of methods for image quality characterization: Noise power spectrum*", Medical Physics, **2006**.

[33] C. Ghetti, O. Ortenzia, G. Serreli, "*CT Iterative reconstruction in image space: A phantom study*", Physica Medica, **2011**.

[34] J.T. Dobbins, E. Samei, N.T. Ranger, Y. Chen, "*Intercomparison of methods for image quality characterization: Modulation transfer function*", Medical Physics, **2006**.

[35] J.Y. Vaishnav, W.C. Jung, L.M. Popescu, R. Zeng, K.J. Myers, "*Objective assessment of image quality and dose reduction in CT iterative reconstruction*", Medical Physics, **2014**.

[36] E. Buhr, S.G. Kohfahl, U. Neitzel, "*Accuracy of a simple method for deriving the presampled modulation transfer function of a digital radiographic system from an edge image*", Medical Physics, **2003**.

[37] I.A. Cunningham, B.K. Reid, "*Signal and noise in modulation transfer function determinations using the slit, wire, and edge techniques*", Medical Physics, **1992**.

[38] K. Li, J. Zambelli, N. Bevins, Y. Ge and G.H. Chen, "*Spatial resolution characterization of differential phase contrast CT systems via modulation transfer function (MTF) measurements*", Physics in medicine and biology, **2013**.

[39] S.M. Akbari, M.R. Ay, A.R. Kamali, H. Ghadiri, H. Zaidi "*Experimental measurements of modulation transfer function (MTF) in five commercial CT scanners*", XII Mediterranean Conference on Medical and Biological Engineering and Computing, **2010**.

[40] J.M. Wilson, O.I. Christianson, S. Richard, E. Samei "*A methodology for image quality evaluation of advanced CT systems*", Medical Physics, **2013**.

[41] A. Love, M.L. Olsson, R. Siemund, F. Stalhammar, I.M. Bjorkman-Burtscher, M. Soderberg, "*Six iterative reconstruction algorithms in brain CT:a phantom study on image quality at different radiation dose levels*", Journal of Radiology, **2013**.

[42] J. Hausleiter, S. Martinoff, M. Hadamitzky, "*Image quality and radiation exposure with a low tube voltage protocol for coronary CT angiography: result of the PROTECTION Trial*", Cardiovascular imaging, **2010**.

[43] D. Marin, R.C. Nelson,H. Barnhart, "*Detection of pancreatic tumors, image quality, and radiation dose during the pancreatic parenchymal phase: effect of a low-tube-voltage, high-tube-current CT technique-preliminary results*", Radiology, **2010**.

[44] A. Love, M.L. Olsson, R. Siemund, F. Stalhammar, I.M. Bjorkman-Burtscher, M. Soderberg, "*Impact of a reduced tube voltage on CT angiography and radiation dose. Results of the PROTECTION study*", Cardiovascular imaging, **2009**.

[45] K. Tang, L. Wang, R. Li, X. Zheng, G. Cao "*Effect of Low Tube Voltage on Image Quality, Radiation Dose, and Low-Constrast Detectability at Abdominal Multidetector CT: Phantom Study*", Journal of Biomedicine and Biotechnology, **2012**.

[46] G. F. Acquah, B. Schiestl, A. Y. Cofie, J. O. Nkansah, M. Gustavsson "*Radiation dose reduction without degrading image quality during computed tomography examinations: Dosimetry and quality control study*", International Journal of Cancer and Oncology, **2014**.

[47] K. L. Dobeli, S. J. Lewis, S. R. Meikle, D. L. Thiele, P. C. Brennan "*Optimization of Computed Tomography Protocols: Limitations of a Methodology Employing a Phantom with Location-Known Opacities*", Journal of Digital Imaging, **2013**.

[48] E. Samei, N. T. Ranger, J. T. Dobbins, C. E. Ravin "*Effective dose efficiency: an application-specific metric of quality and dose for digital radiography*", Physics in Medicine and Biology, **2011**.

[49] S. Kim, H. Song, E. Samei, F. Yin, T. Yoshizumi "*Computed Tomography dose index and dose length product for cone-beam CT: Monte Carlo simulations of a commercial system*", Journal of Applied Clinical Medical Physics, **2010**.

[50] C. Descamps, M. Gonzalez, E. Garrigo, A. Germanier, D. Venencia "*Measurements of the dose delivered during CT exams using AAPM Task Group Report No.* 111", Journal of Applied Clinical Medical Physics, **2012**.